学 位 論 文

Gold-nanocluster-mediated microinflammation detection using a tissue clearing method and Molecular mechanism for SARS-CoV-2-specific $CD4^+$ T cell activation in healthy people

(組織透明化法を用いた金ナノクラスターによる微小炎症検出と健常人における SARS-CoV-2 特異的 $CD4^+$ T 細胞活性化の分子機構に関する研究)

2023年 3 月

北 海 道 大 学

フェイロウズ　シャウキー　アブデルモネイム ネイム

Fayrouz Shawky Abdelmoneim Naim

Molecular Psychoimmunology

学 位 論 文

Gold-nanocluster-mediated microinflammation detection using a tissue clearing method and Molecular mechanism for SARS-CoV-2-specific $CD4^+$ T cell activation in healthy people

(組織透明化法を用いた金ナノクラスターによる微小炎症検出と健常人における SARS-CoV-2 特異的 $CD4^+$ T 細胞活性化の分子機構に関する研究)

2023年 3 月

北 海 道 大 学

フェイロウズ　シャウキー　アブデルモネイム ネイム

Fayrouz Shawky Abdelmoneim Naim

Molecular Psychoimmunology

Table of Contents

Page#

List of Publications and Presentations ---------- 1

Summary ---------- 2

List of Abbreviations ---------- 4

Chapter #1: Molecular mechanism for SARS-CoV-2-specific $CD4^+$ T cell activation in healthy people

1. Introduction ---------- 7
2. Materials and Methods ---------- 15
3. Results ---------- 22
4. Discussion ---------- 44

Chapter #2: Gold-nanocluster-mediated microinflammation detection using a tissue clearing method

1. Introduction ---------- 46
2. Materials and Methods ---------- 54
3. Results ---------- 59
4. Discussion ---------- 67

Conclusion ---------- 68

Acknowledgements ---------- 69

Disclosure of Conflict of Interest ---------- 69

References ---------- 70

List of Publications and Presentations

List of Publications:

1. **Fayrouz Naim**, Rie Hasebe, Shintaro Hojyo, Yukatsu Shichibu, Yuki Tanaka, Kazuki Tainaka, Shimpei I Kubota, Katsuaki Konishi, and Masaaki Murakami "Gold-nanocluster-mediated microinflammation detection by using a tissue clearing method." Bio-Protocol, Accepted.
2. Ibrahim Fouad Elesh, Mohamed Ali Marey, Mohammed Ali Zinnah, Ihshan Akthar, Tomoko Kawai **Fayrouz Naim**,Wael Goda et al. "Peptidoglycan switches off the TLR2-Mediated sperm recognition and triggers sperm localization in the bovine endometrium." Frontiers in immunology 11 (2021): 619408.
3. **Fayrouz S. Naim**, Samy A. Khalil and Helmy A. Torky. "Comparative Study of Cellular and Humoral Immune Response to BHV-1 Vaccines in Cattle and Buffalo Calves." Alexandria Journal of Veterinary Sciences 51.2 (2016), 367373.

List of Presentations:

- **Fayrouz Naim**, Daisuke Kamimura, Masaaki Murakami. Role of Schizophrenia associated genes in induction of inflammation amplifier (IL6 amplifier). Integrations of Life and Material Science by Young Researchers! The 6th Hokkaido University Cross-Departmental Symposium. 2020 October 19, Graduate School of Medicine, Hokkaido University. (Poster)

Summary

Background and purpose:
Inflammation is a part of biological homeostatic response triggered by an entry of foreign substances into the body, such as pathogens, damaged cells, or irritants, and is a series of biochemical events by mobilizing local immune system, vascular system and various cells within damaged tissues. Upon inflammation, immune system can form a sophisticated immune memory mechanism, which eliminates the previously-encountered infectious agents quickly and strongly. On the other hand, when inflammation is prolonged, chronic inflammation such as autoimmune diseases develop, the state of cells present at the site of inflammation alters, resulting in permanent tissue destruction.
Using mouse models of inflammatory diseases and clinical specimens, my laboratory has previously shown that stimulation of Toll-like receptor ligands, Tumor necrosis factor-α (TNF-α), Interleukin-1(IL-1) or growth factors in tissue-specific non-immune cells causes simultaneous activation of Nuclear factor kappa-light-chain-enhancer of activated B cells (NF-κB) and Signal transducers and activators of transcription 3 (STAT3) in concert with Interleukin-6 (IL-6), and lead to excessive and sustained activation of NF-κB, so called "IL-6 amplifier", resulting in various chronic inflammatory diseases including autoimmune diseases. More recently, we reported the hypothesis that novel coronavirus disease 2019 (COVID-19) caused by severe acute respiratory syndrome coronavirus-2 (SARS-CoV-2) infection may be lethal via IL-6 amplifier, in which the induction of cytokine storms may lead to severe disease. Thus, understanding of inflammatory mechanisms will lead to development of effective vaccines for prevention and treatment against emerging infectious and other diseases, and of methods to detect microinflammation as a cause of chronic inflammatory diseases.
In my doctoral research projects, I aimed at (1) exploring and establishing methodology to examine the reactivity and immunodominance of immune memory cluster of differentiation 4 T-cells ($CD4^+$T-cells) against SARS-CoV-2 viral antigens, which could contribute to the future development of highly effective vaccines against emerging infectious diseases, using COVID-19 as a subject; (2) developing the detection method of microinflammation as a potential cause of chronic inflammatory diseases, in 3D-image with gold nanoclusters and tissue-clearing method in active and pathogenic $CD4^+$T-cells transfer model of experimental autoimmune encephalomyelitis (EAE; multiple sclerosis model).

Materials and methods:
(1) Twenty-four histidine (His)-tagged SARS-CoV-2 recombinant proteins, including non-structural (NSPs); nsp1, nsp2, nsp5, nsp7, nsp8, nsp9, nsp10, nsp12, nsp13, nsp14, nsp15 and nsp16 and structural (SPs) proteins; orf3a, E protein, M protein, orf6, orf7a, orf7b, orf8, N protein and orf10, and were synthesized in cell-free system, purified, and bound to Dynabeads. To first determine an optimal incubation time for in vitro study of $CD4^+$ T-cell reactivity and immunodominance, peripheral blood mononuclear cells (PBMCs) from recovered patients from COVID-19 were cultured for 4 or 6 days in the presence of Dynabeads-bound viral antigens. The population of activated $CD4^+$ T-cells in the culture was then assessed. Next, to actually investigate the reactivity and immunodominance of $CD4^+$T-cells in healthy individuals, PBMCs were cultured for 6 days in the presence of viral antigens and the population of activated $CD4^+$ T-cells was assessed using flow cytometry analysis for CD3, CD4, CD8, CD19, CD137, OX40 surface markers. Data analysis was carried out by FlowJo™ 10 software.

(2) Following induction of active and passive EAE mice model, the mice treated with Au_{13} nanocluster solution at concertation of 32 μM with saline, and 200 μl of the dilutant was injected i.v. to EAE mice with score 2-3. After 2 hrs, the mice are anesthetized with isoflurane, and perfused with 25 ml of cold phosphate buffer saline (PBS), followed by 20 ml cold 4% paraformaldehyde. The spine was taken out and post-fixed in 40 ml of 4% (w/v) PFA in a 50 ml tube at 4 °C for 24 hrs with shaking. The spine was washed with 40 ml of PBS at room temperature (RT) for 0.5 hr three times with shaking and lumber cord (L1-L6) were carefully excised under stereomicroscope system. L1-L6 were immersed in delipidation buffer in a 15 ml tube at 37℃ for 4 days with shaking, then washed with 10 ml of PBS at RT for 1 hr three times. The samples were stained with staining buffer contained a mouse monoclonal α-smooth muscle (SMA) antibody or purified rat anti-mouse CD31 at RT for 7 days with shaking at 100 rpm horizontally. Then samples were washed, postfixed and washed again. The samples were immersed in 1/2 CUBIC-R at RT for 5 hrs with shaking at 100 rpm horizontally. After discarding 1/2 CUBIC-R, the samples were further immersed in 10 ml of CUBIC-R at RT overnight with shaking at 100 rpm horizontally then replaced with fresh CUBIC-R, and further immersed at RT for 12 hrs with shaking. The cleared lumbar cords were subsequently subjected to an imaging analysis of the L5 using a light-sheet microscope.

Results:

(1) SARS-CoV-2 proteins were successfully synthesized and purified using a cell-free protein synthesis system. The optimal incubation time to examining $CD4^+$ T cell reactivity and immunodominance to viral proteins was 6 days. When PBMCs in healthy individuals were reactivated viral proteins under this culture condition, $CD4^+$ T cells were more reactive to NSPs than to SPs.

(2) Gold nanocluster particles administered to EAE mice were detected around the dorsal vessels of the L5, which were observed similarly in both active and T-cell-transferred-models of EAE.

Discussion:

(1) The present study supports the previous finding by others that memory T-cells exhibiting cross-reactivity between SARS-CoV-1, SARS-CoV-2 and HuCoV (a common cold coronavirus), exist in SARS-CoV-2-uninfected individuals. In this study, we found that the pre-existing memory $CD4^+$ T-cells in healthy donors reactive to viral NSPs are more frequently than those to SPs, probably being attributed to the high homology of the NSPs from SARS-CoV-2 to those in HuCoVs. My study suggests that NSPs may be more useful target than SPs to develop effective vaccines against SARS-CoV-2.

(2) In inflammatory diseases, single-cell events ultimately affect the health of whole organism. Although it has been desired to establish a detection system which enables rapidly to identify the occurrence and progression of microinflammation, that contributes to the pathogenesis of inflammatory disease, conventional detection methods of inflammation have mainly involved 2D-tissue analysis using reporter mice and antibodies for inflammation-related molecules. Through my study, I was able to establish a method to rapidly visualize inflammatory organs in 3D-image, and to corroborate our previous findings that microinflammation at L5 triggers the onset of EAE.

Conclusion:

immunodominance search and microinflammation detection methods established in my study will further contribute to the establishment of preventive and therapeutic methods for various inflammatory diseases in the future.

List of Abbreviations

AIM	Activation-induced markers
ARDS	Acute respiratory distress syndrome
CD	Cluster of differentiation
CNS	Central nervous system
COVID-19	Coronavirus disease 2019
CSF	Cerebrospinal fluid
DNA	Deoxyribonucleic acid
EAE	Experimental autoimmune encephalomyelitis
His	Histidine
HLA	Human leukocyte antigen
IFN	Interferon
IL	Interleukin
MBP	Myelin basic protein
MERS-CoV	Middle East respiratory syndrome cronavirus
2-ME	2-mercaptoethanol
MHC	Major histocompatibility complex
MOG	Myelin oligodendrocyte glycoprotein
MS	Multiple sclerosis
NSP	Non-structural protein
ORF	Open reading frame
PBS	Phosphate-buffered saline
PCR	Polymerase chain reaction
PMBCs	Peripheral blood mononuclear cells
PRR	Pattern recognition receptor
PTx	Pertussis toxin
RA	Rheumatoid arthritis
RBD	Receptor-binding domain
RNA	Ribonucleic acid
SAR	Sarilumab

SARS-CoV	Severe acute respiratory syndrome coronavirus
SDS-PAGE	Sodium dodecyl sulfate-polyacrylamide gel electrophoresis
SP	Structural protein
TCR	T-cell receptor
TNFRSF	Tumor necrosis factor receptor superfamily
Th	T helper

Keywords

Chapter #1

- COVID-19
- SARS-CoV-2
- AIM+CD4+T-cells
- NSPs
- SPs

Chapter #2

- EAE
- Gateway reflex
- Gold nanocluster
- CUBIC tissue-clearing

Chapter #1

Molecular mechanism for SARS-CoV-2-specific $CD4^+$ T cell activation in healthy people

1.Introduction

1-1. COVID-19

In December 2019, the first case of the newly emerging coronavirus disease 2019 (COVID-19) was identified in patients with respiratory disease in Wuhan, China. The disease is reported to be caused by a severe acute respiratory syndrome coronavirus 2 (SARS-CoV-2), and has spread rapidly all over the world, resulting in the pandemic. The virus is believed to have been originally carried by bats and other wild animals, which independently spread to humans and acquired the ability to human-to-human transmission (Phan et al., 2020). Since the end of 2020, new mutant variants with virus structural alterations in the spike protein have also emerged one after another, replacing previous strains and causing frequent outbreaks in various parts of the world. According to COVID-19 Map, Johns Hopkins University and Medicine (https://coronavirus.jhu.edu/map.html), the COVID-19 has been associated with 584,591,121 cases and 6,418,041 deaths.

While one third of people infected with SARS-CoV-2 are asymptomatic or develop only mild disease, some patients develop severe disease, leading to acute respiratory failure and multiple organ failure. The typical symptoms of the disease including fever, cough, headache, fatigue, breathing difficulties, loss of smell, and loss of taste occur within 5–6 days, when the viral load reaches a peak, and 97.5% of symptomatic patients further develop COVID-19 within 14 days. Proinflammatory cytokine release syndrome caused by activation of various immune cells by SARS-CoV-2 infection is characterized by hyperinflammation, which manifests as acute respiratory distress syndrome (ARDS), and other broad spectrum of severity such as multiorgan failure, blood clots, dyspnoea, and hyposia (Hirano and Murakami, 2020; Quan et al.,2020) that are associated with mortality and poor prognostic features even when patients are hospitalized (Jose and Manuel, 2020). Furthermore, some people continue to experience a variety of effects, so called long COVID (Mehandru and Merad, 2022), for months even after the recovery and damage to

organs in the major symptoms, has been observed. Therefore, a long-term study to further investigate effects of the disease and mechanism in long COVID has been intensively performed.

1-2. Viral entry of SARS-CoV-2 and host immune response

Over the past two decades, severe respiratory diseases were caused by zoonotic infections of SARS-CoV and Middle East respiratory syndrome coronavirus (MERS-CoV) from animals to humans in endemic areas. Genomic analysis revealed that SARS-CoV-2 shares about 80% genetic identity with SARS-CoV, around 50% with MERS-CoV, and around 90% with bat-SL-CoVZC45 and bat-SL-CoVZXC21 coronaviruses, suggesting bat-to-human zoonotic transmission of this new virus (Lu et al., 2020; McGonagle et al., 2020; Zhou et al., 2020b). Furthermore, proteomic characterization also showed that SARS-CoV-2 has seven conserved non-structural domains similar to SARS-CoV, suggesting a relationship between the two *Betacoronaviruses*.

SARS-CoV-2 utilizes angiotensin-converting enzyme II (ACE2) as the entry receptors, while MERS-CoV and HCoV-229E utilize dipeptidyl peptidase 4 or aminopeptidase N, respectively, to infect the host cells originated from humans, Chinese horseshoe bats, civet, and pigs (Hoffmann et al., 2020; Kuba et al., 2005; Li et al., 2003; Zhou et al., 2020b). The virus entry also occurs dependent on transmembrane serine protease 2 (TMPRSS2) and endosomal cysteine proteases cathepsin B and L (CatB/L) for viral spike (S) protein priming (Hoffmann et al., 2020). Upon SARS-CoV-2 infection, the endocytosis of ACE2 together with SARS-CoV occurs in target cells including epithelial cells and endothelial cells, resulting in an increase of serum angiotensin II (Ang II) levels due to the reduction of ACE2 surface expression **(Fig. 1)** (Kuba et al., 2005; Verdecchia et al., 2020). Ang II acts not only as a vasoconstrictor but also as a pro-inflammatory cytokine via Ang II type 1 receptor (AT1R) (Eguchi et al., 2018), suggesting that a renin-angiotensin system (RAS) may be involved in the ARDS development following SARS-CoV-2 infection (Hirano and Murakami, 2020). In fact, the pharmacological blockade of AT1R or treatment of exogenous recombinant ACE2 suppresses the development of ARDS induced by SARS-CoV infection (Kuba et al., 2005). The Ang II-AT1R signaling axis activates ADAM metallopeptidase domain 17 (ADAM17), which in turn digests the membrane forms of epidermal growth factor family members (EGF, epiregulin, amphiregulin, transforming growth factor-alpha ,etc.) and tumor necrosis factor (TNF)-α, all of which stimulate the NF-κB pathway **(Fig. 1)** (Eguchi et al., 2018; Hirano and

Murakami, 2020; Scheller et al., 2011). ADAM17 also processes membrane-bound interleukin (IL)-6 receptor alpha (IL-6Rα) to the soluble form (sIL-6Rα), and the resultant sIL-6R-IL-6 complex then binds to gp130 expressed on non-immune cells including endothelial cells, epithelial cells, and fibroblasts even without membrane IL-6R expression, and can activate Janus kinase (JAK)/STAT3 (Murakami et al., 2019). Thus, Ang II-AT1R signaling may lead to an IL-6-mediated positive feedback loop of NF-κB signaling, so called "IL-6 amplifier", during inflammation, followed by an exacerbation of COVID-19 with ARDS, multiorgan failure, and coagulation **(Fig. 1)**.

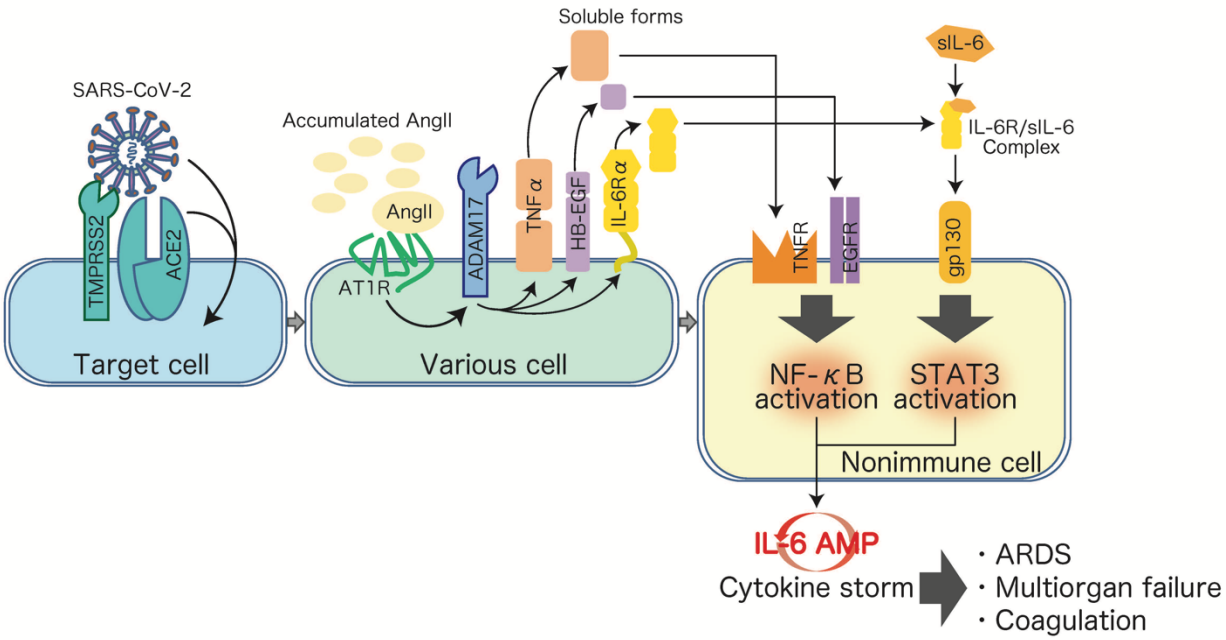

Fig. 1: IL-6-STAT3 signaling may be involved in severe COVID-19

SARS-CoV-2 enters cells via cell membrane-localized ACE2 depending on TMPRSS2 and CatB/L activities for viral S protein priming. The viral pathogen-associated molecular patterns trigger IL-6 production followed by activation of the NF-κB pathway via PRRs in both immune and non-immune cells, leading to an inflammatory response. On the other hand, upon the occupancy of ACE2 by SARS-CoV-2, the increased serum level of free Ang II due to a reduction of ACE2-mediated degradation also promotes activation of the NF-κB pathway via AT1R, followed by IL-6 production. Simultaneously, Ang II-AT1R signaling activates ADAM17 and ADAM10 protease activity, and the resulting production of TNF-α, sIL-6Rα, and EGF initiates the TNFR-NF-κB, IL-

6R-STAT3, and EGF-NF-κB signaling pathways. Consequently, the concomitant inflammatory cascades of NF-κB- and STAT3-mediated signaling further augment NF-κB activity and establish an inflammatory circuit, the IL-6 amplifier (IL-6 AMP), which describes an IL-6-based positive feedback loop for inflammation in non-immune cells. Thus, the cytokine storm caused by the hyper-activation of NF-κB in IL-6 AMP may cause fatal symptoms such as ARDS, severe pneumonia, multiorgan failure, and coagulation in a subgroup of hospitalized COVID-19 patients. In line with this, the blockade of IL-6-STAT3 signaling should shed light on the treatment of severe COVID-19.

1-3. Interleukin-6 (IL-6)

IL-6, which was discovered in 1986, is a pleiotropic cytokine involved not only in immune responses but also in inflammation, hematopoiesis, bone metabolism, embryonic development, and other fundamental processes **(Fig. 2)** (Hirano, 1998).

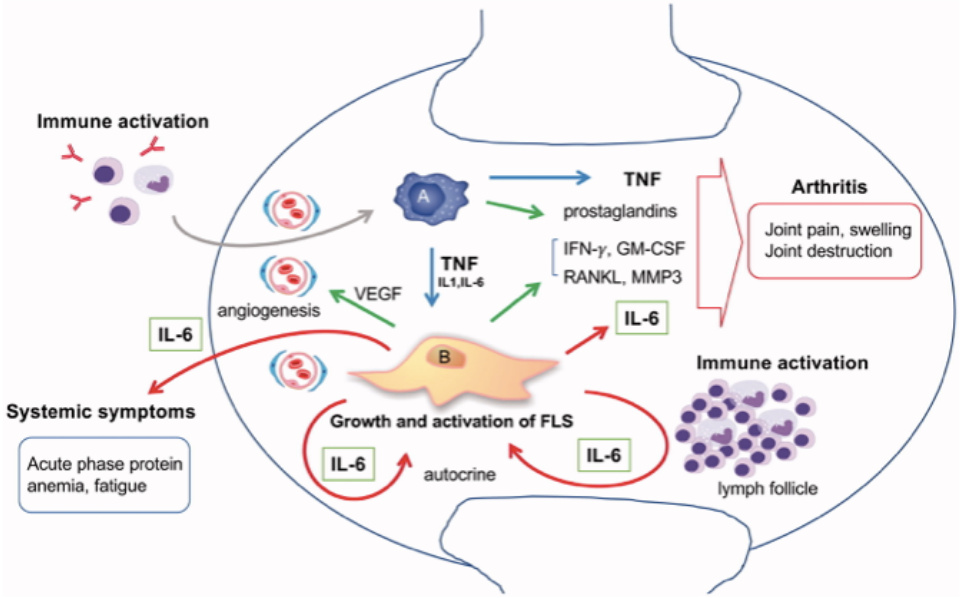

Fig. 2: Summary of pathogenic role of IL-6 in RA (Raimondo et al., 2017)

IL-6 is a prototypical member of the IL-6 family of cytokines, which is composed of 10 members including IL-6, IL-11, IL-27, oncostatin M (OSM), leukemia inhibitory factor (LIF), ciliary neurotrophic factor (CNTF), cardiotrophin 1 (CT-1), cardiotrophin-like cytokine factor1 (CLCF1), IL-35 and IL-39 (Murakami et al., 2019). Studies in the 1980s showed that IL-6 is produced by

cardiac myxoma cells (Hirano et al., 1987) and Castleman's germinal center cells (Yoshizaki et al., 1989), and is present at high amounts in the synovial fluid of RA patient (Hirano et al., 1988; Houssiau et al., 1988), suggesting its pathogenic role in autoimmune diseases and chronic inflammatory diseases (Hirano, 1992, 1998).

IL-6 is a multifunctional cytokine with biological activities that include regulation of immune response, inflammation, and hematopoiesis. IL-6 also possesses several proinflammatory properties, such as stimulating the production of chemokines and adhesion molecules in lymphocytes, inducing acute-phase proteins in liver cells and increasing neutrophil counts in the blood (Hashizume and Mihara, 2011).

1-4. The role of IL-6 amplifier in autoimmune diseases

IL-6 amplifier is a fundamental molecular mechanism of tissue-specific inflammation and enhances the activation of NF-κB in non-immune cells including synovial fibroblasts, endothelial cells, and chondrocytes, followed by regionally expressing excessive chemokines, cytokines, and growth factors in animal models and patients of RA and osteoarthritis **(Fig. 3)** (Harada et al., 2015; Murakami et al., 2013; Murakami et al., 2011; Ogura et al., 2008). In this system, hyper-activation of the NF-κB signal is induced by the simultaneous stimulation of NF-κB and STAT3, followed by the local induction of inflammation (Atsumi et al., 2014; Atsumi et al., 2017; Fujita et al., 2019; Harada et al., 2015; Higuchi et al., 2020; Lee et al., 2013; Lee et al., 2012; Meng et al., 2016; Ogura et al., 2008; Okuyama et al., 2018; Ota et al., 2020; Takada et al., 2020; Tanaka et al., 2018). Because one NF-κB target, IL-6, stimulates STAT3 during inflammation, its autocrine and/or paracrine action helps maintain STAT3 activation to express inflammatory mediators via the IL-6 amplifier in various inflammatory diseases (Hirano and Murakami, 2020; Murakami et al., 2019). We further showed that the IL-6 amplifier plays a role in other tissue-specific inflammatory diseases in many organs including the skin, kidney, central nervous system (CNS), and lung (Atsumi et al., 2014; Atsumi et al., 2017; Fujita et al., 2019; Harada et al., 2015; Higuchi et al., 2020; Lee et al., 2013; Lee et al., 2012; Meng et al., 2016; Ogura et al., 2008; Okuyama et al., 2018; Ota et al., 2020; Takada et al., 2020; Tanaka et al., 2018). Accordingly, we have defined inflammation as an IL-6-mediated accumulation of immune cells and/or proliferation of immune cells and regional non-immune cells, followed by the dysregulation of local homeostasis including

the dysfunction of tissues and/or organs. It has been proposed that autoimmune diseases are caused by a break-down of self-tolerance due to multiple genetic and/or environmental factors, suggesting that the dysregulation of immune system is causative for autoimmune diseases. This agrees with the theory that certain autoimmune diseases like RA, develop in specific tissues as a result of cognate antigen-recognition by $CD4^+$ T cells, particularly, when these diseases are associated with MHCII alleles. Consistent with this, joint-specific antigen specific peptides such as derivatives of aggrecan, fibrillin, and collagen have been identified in humans (Murakami and Hirano, 2011).

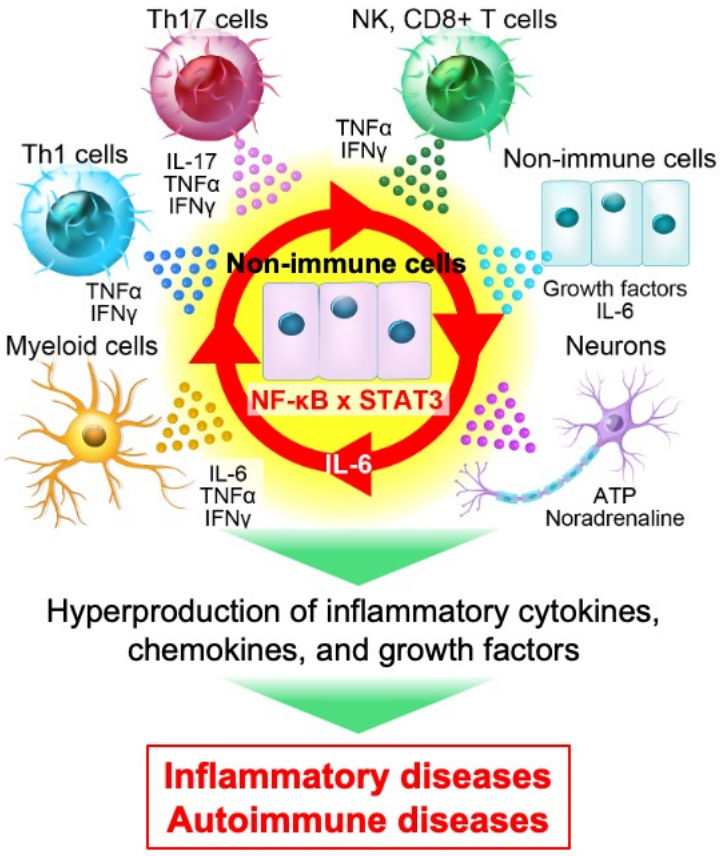

Fig. 3: IL-6 amplifier

In the IL-6 amplifier, a concurrent activation of the transcription factors NF-κB and STATs in non-immune cells including vascular endothelial cells and fibroblasts induces a multiplier effect on the production of growth factors, chemokines, and cytokines such as IL-6. Various factors activating NF-κB and STATs can operate the amplifier. IL-6 can act on non-immune cells to form an amplifying loop. Excessive production of chemokines and growth factors through activation of the

inflammation amplifier play a key role in the pathogenesis of many chronic inflammatory diseases. NK, natural killer cells; Th, helper T cells**.**

1-3. SARS-CoV-2 proteins

SARS-CoV-2 is RNA virus with an approximately 30,000 nucleotides in a single-stranded RNA genome (Alexandersen et al., 2020; Manfredonia et al., 2020), which encodes 29 proteins, including 16 nonstructural proteins (NSPs), 4 structural proteins (SPs), and 9 accessory proteins **(Fig. 4)** (Gorkhali et al., 2021). The viral genome consists of 14 functional open reading frames (ORFs) including 2 non-coding regions (Lu et al., 2020; Wu et al., 2020). The ORF1a and ORF1b encode nsp1-16, which have significant roles in virus replication and transcription in the host cells. The ORF2, 4, 5, and 9a encodes for S (spike), E (envelope), M (membrane), and N (nucleocapsid) proteins that are essential for host membrane attachment and fusion, viral membrane formation, viral assembly, and nucleocapsid formation, respectively. Furthermore, the ORF3a, 3b, 6, 7a, 7b, 8b, 9b, 9c, and 10 encode for other accessory proteins like ORF3a, ORF7a, and ORF8 are essential for selective advantage in viral pathogenesis. (Arya et al., 2021; Bartlam et al., 2007; Solanki et al., 2021; Ziebuhr, 2004).

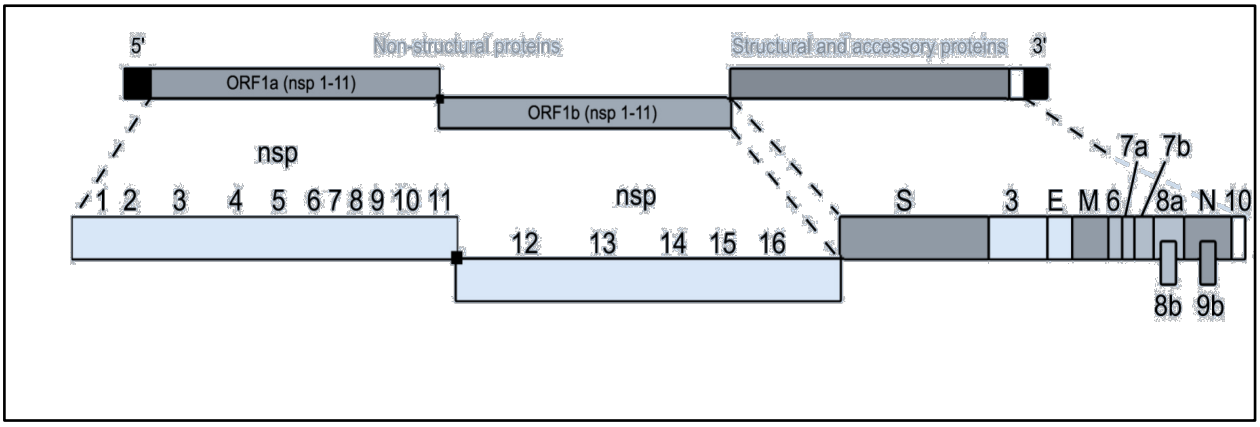

Fig. 4: Genome organization of the SARS-CoV-2

The viral genome encodes 16 NSPs required for replication/transcription along with the structural proteins and accessory proteins required for the assembly of new virions and viral pathogenesis.

1-4. Pre-existing adaptive immune response to SARS-CoV-2

There are seven coronaviruses associated with disease in humans, which mostly lead to mild respiratory illness (Fung and Liu, 2019). Among them, SARS-CoV, MERS-CoV, and SARS-CoV-2 are exceptional and highly pathogenic, leading to death in some cases. Difference in the mortality cases among different regions around the world, could be due to distinct levels of adaptive immune response that is armed by an exposure to coronaviruses in past time. SARS-CoV and SARS-CoV-2 share significant sequence homology, and share antigenic epitopes capable of inducing an adaptive immune response especially SARS-CoV, which share 80% of genetic identity (Lu et al., 2020; Zhou et al., 2020b). Thus, pre-exposure to one virus might lead to partial immunity to another. Using human leukocyte antigen (HLA) class, I and II predicted peptide megapools, Grifoni et al. has found that SARS-CoV-2-reactive $CD4^+$ T-cells present in 40%–60% of peripheral blood of unexposed individuals between 2015 and 2018 before SARS-CoV-2 emerged (Grifoni et al., 2020). Weiskopf et al. showed that $CD4^+$ T-cells from one of ten and two of ten unexposed people exhibit the reactivity to spike peptides and non-spike peptides of SARS-CoV-2, respectively (Weiskopf et al., 2020). Furthermore, Braun reported that positive T-cell responses to spike peptides were observed in 34% of SARS-CoV-2 seronegative healthy donors (Braun et al., 2020). Thus, these findings suggest that pre-existing T cells in healthy donors, which might experience an exposure to "common cold" coronaviruses, have cross-reactivity against SARS-CoV-2 (Grifoni et al., 2020).

1-5. Hypothesis and Objectives

Since the previous report showed that non-spike-specific AIM^+CD4^+ T-cell responses were above the limit of detection in 50% of healthy donors based on the method using HLA class I- and II-predicted peptide (megapools)(Grifoni et al., 2020), I aimed at investigating AIM^+CD4^+ T cell responses to 24 SARS-CoV-2 proteins in healthy donors, which might help for developing of future vaccines to SARS-CoV-2 .

2. Materials and Methods

2-1. Cloning of SARS-CoV-2 genes encoding SPs and NSPs

Template cDNA was synthesized with the SMARTScribe Reverse Transcriptase (TAKARA #639538) using total RNA which was extracted from VeroE6/TMPRSS2 cells (Matsuyama et al., 2020) infected with SARS-CoV-2, using ISOGEN reagent (NIPPON GENE, #319-90211). The cDNA fragments, which includes the entire open reading frame of each of the genes encoding SPs; orf3a, E protein, M protein, orf6, orf7a, orf7b, orf8, N protein and orf10, and NSPs; nsp1, nsp2, nsp5, nsp7, nsp8, nsp9, nsp10, nsp12, nsp13, nsp14, nsp15 and nsp16, were amplified from the template cDNA using the corresponding pair of oligonucleotide primers in **Table 1** with PrimeSTAR GXL DNA Polymerase (Takara, #R050B(Ax4)). The PCR products were cloned into pCR Blunt II-TOPO with Zero Blunt TOPO PCR Cloning Kit (ThermoFisher Scientific, #451245). Plasmid including cDNA fragment encoding SARS-CoV-2 spike protein is a kind gift from Dr. Mutsuura (Osaka University).

Table 1. Oligonucleotide primer pairs used for cDNA cloning of SARS-CoV-2 genes

Protein	**Forward primer (5' – 3')**	**Reverse primer (5' – 3')**
nsp1	Atggagagccttgtccctgg	Ccctccgttaagctcacgc
nsp2	Gcatacactcgctatgtcga	Accgcctttgagtgtgaagg
nsp5	Agtggttttagaaaaatggc	Ttggaaagtaacacctgagc
nsp7	Tctaaaatgtcagatgtaaa	Ttgtaaggttgccctgttgt
nsp8	Gctatagcctcagagtttag	Ctgtaatttgacagcagaat
nsp9	Aataatgagcttagtcctgt	Ttgtagacgtactgtggcag
nsp10	Gctggtaatgcaacagaagt	Ctgaagcatgggttcgcgga
nsp1	Tcagctgatgcacaatcgtttttaaaccgggtttgcggtgtaagtgcagcccgtcttacaccgtgcggcacaggcactag	Ctgtaagactgtatgcggtg
nsp13	Gctgttggggcttgtgttct	Ttgtaaagttgccacattcc
nsp14	Gctgaaaatgtaacaggact	Ctgaagtcttgtaaaagtgt
nsp15	Agtttagaaaatgtggcttt	Ttgtaattttgggtaaaatg
nsp16	Tctagtcaagcgtggcaacc	Gttgttaacaagaacatcac
orf3a	Atggatttgtttatgagaat	Ttacaaaggcacgctagtag
E protein	Atgtactcattcgtttcgga	Ttagaccagaagatcaggaa
M protein	Atggcagattccaacggtac	Ttactgtacaagcaaagcaa
orf6	Atgtttcatctcgttgactt	Ttaatcaatctccattggtt
orf7a	Atgaaaattattcttttctt	Tcattctgtctttcttttga
Orf7b	Atgattgaactttcattaat	Ttaggcgtgacaagtttcat
orf8	Atgaaatttcttgttttctt	Ttagatgaaatctaaaacaa
N protein	Atgtctgataatggacccca	Ttaggcctgagttgagtcag

orf10	Atgggctatataaacgttttcgcttttccgtttacgat atatagtctactcttgtgcagaatgaattctc	Ctatgtgagattaaagttaactacatctacttgtgctatgt agttacgagaattcattctgcacaagagt

2-2. Cell-free synthesis of SARS-CoV-2 SPs and NSPs

Cell-free protein synthesis was performed using the PUREfrex 2.1 kit, according to the manufacturer's instructions (GeneFrontier, # PF213-0125-5). Briefly, each of the genes encoding SPs and NSPs (spike protein S1, spike protein S2, orf3a, E protein, M protein, orf6, orf7a, orf7b, orf8, N protein, orf10, nsp1, nsp2, nsp5, nsp7, nsp8, nsp9, nsp10, nsp12, nsp13, nsp14, nsp15 and nsp16), which were fused with 6 x histidine (His)-tag sequence at the N or C-terminus are amplified from the plasmids including each of the cDNA fragment by PCR, using the corresponding pair of oligonucleotide primers in **Table 2**. Then, second PCR was performed with the corresponding pair of oligonucleotide primers in **Table 3**, using each of the first PCR products as a template. After purified with GenElute PCR Clean-Up Kit (Merck, #NA1020), the second PCR products were used as the template DNA for the cell-free protein synthesis with the PUREfrex 2.1 kit. Nsp11 fused with 6 x His-tag was prepared by peptide synthesis. The synthesized proteins were immobilized on magnetic beads; Dynabeads His-Tag Isolation & Pulldown (ThermoFisher Scientific, #DB10104), in binding buffer containing 50 mM Tris-HCl (pH 8.0), 500 mM NaCl, 20 mM $MgCl_2$, and 20 mM imidazole, washed with the binding buffer twice, and subsequently with wash buffer containing 50 mM Tris-HCl (pH 8.0), 500 mM NaCl, and 20 mM imidazole twice. The synthesized protein immobilized on the magnetic beads were stored at 4ºC until use.

Table 2. Oligonucleotide primer pairs used for the first PCR

Protein	**Forward primer (5' – 3')**	**Reverse primer (5' – 3')**
nsp1	aaggagatataccaatgCATCACCATCA CCATCACatggagagccttgtccctgg	Ggattagttattcattaccctccgttaagctcacgc
nsp2	aaggagatataccaatgCATCACCATCA CCATCACgcatacactcgctatgtcga	Ggattagttattcattaaccgcctttgagtgtgaag g
nsp5	aaggagatataccaatgCATCACCATCA CCATCACagtggttttagaaaaatggc	Ggattagttattcattattggaaagtaacacctgag c
nsp7	aaggagatataccaatgCATCACCATCA CCATCACtctaaaatgtcagatgtaaa	Ggattagttattcattattgtaaggttgccctgttgt
nsp8	aaggagatataccaatgCATCACCATCA CCATCACgctatagcctcagagtttag	Ggattagttattcattactgtaatttgacagcagaat
nsp9	aaggagatataccaatgCATCACCATCA CCATCACaataatgagcttagtcctgt	Ggattagttattcattattgtagacgtactgtggcag
nsp10	aaggagatataccaatgCATCACCATCA CCATCACgctggtaatgcaacagaagt	Ggattagttattcattactgaagcatgggttcgcgg a

nsp12	aaggagatataccaatgCATCACCATCACCATCACtcagctgatgcacaatcgtt	Ggattagttattcattactgtaagactgtatgcggtg
nsp13	aaggagatataccaatgCATCACCATCACCATCACgctgttggggcttgtgttct	Ggattagttattcattattgtaaagttgccacattcc
nsp14	aaggagatataccaatgCATCACCATCACCATCACgctgaaaatgtaacaggact	Ggattagttattcattactgaagtcttgtaaaagtgt
nsp15	aaggagatataccaatgCATCACCATCACCATCACagtttagaaaatgtggcttt	Ggattagttattcattattgtaattttgggtaaaatg
nsp16	aaggagatataccaatgCATCACCATCACCATCACtctagtcaagcgtggcaacc	Ggattagttattcattagttgttaacaagaacatcac
Spike protein S1	Aaggagatataccaatgcagtgtgttaatcttacaac	ggattagttattcattaGTGATGGTGATGGTGATGacgtgcccgccgaggagaat
Spike protein S2	Aaggagatataccaatgagtgtagctagtcaatccat	ggattagttattcattaGTGATGGTGATGGTGATGtgtgtaatgtaatttgactc
orf3a	Aaggagatataccaatggatttgtttatgagaat	ggattagttattcattaGTGATGGTGATGGTGATGcaaaggcacgctagtag
E protein	aaggagatataccaatgCATCACCATCACCATCACatgtactcattcgtttcgga	Ggattagttattcattagaccagaagatcaggaa
M protein	aaggagatataccaatgCATCACCATCACCATCACatggcagattccaacggtac	Ggattagttattcattactgtacaagcaaagcaa
orf6	aaggagatataccaatgCATCACCATCACCATCACatgtttcatctcgttgactt	Ggattagttattcattaatcaatctccattggtt
orf7a	aaggagatataccaatgCATCACCATCACCATCACatgaaaattattcttttctt	Ggattagttattcattattctgtctttcttttga
orf7b	aaggagatataccaatgCATCACCATCACCATCACatgattgaactttcattaat	Ggattagttattcattaggcgtgacaagtttcat
orf8	aaggagatataccaatgCATCACCATCACCATCACatgaaatttcttgttttctt	Ggattagttattcattagatgaaatctaaaacaa
N protein	aaggagatataccaatgCATCACCATCACCATCACatgtctgataatggacccca	Ggattagttattcattaggcctgagttgagtcag
orf10	aaggagatataccaatgCATCACCATCACCATCACatgggctatataaacgtttt	Ggattagttattcattatgtgagattaaagttaa

*DNA sequences described by capital letter show sequences corresponding to 6 x His-tag.

Table 3. Oligonucleotide primer pairs used for the second PCR

Protein	**Forward primer (5' – 3')**	**Reverse primer (5' – 3')**
nsp1	Gaaattaatacgactcactatagggagaccacaacggtttccctctagaaataattttgtttaactttaagaaggagatatacca	Ggattagttattcattaccctccgttaagctcacgc
nsp2	Gaaattaatacgactcactatagggagaccacaacggtttccctctagaaataattttgtttaactttaagaaggagatatacca	Ggattagttattcattaaccgcctttgagtgtgaagg
nsp5	Gaaattaatacgactcactatagggagaccacaacggtttccctctagaaataattttgtttaactttaagaaggagatatacca	Ggattagttattcattattggaaagtaacacctgagc

nsp7	Gaaattaatacgactcactatagggagaccacaacggtttccctctagaaataattttgtttaactttaagaaggagatatacca	Ggattagttattcattattgtaaggttgccctgttgt
nsp8	Gaaattaatacgactcactatagggagaccacaacggtttccctctagaaataattttgtttaactttaagaaggagatatacca	Ggattagttattcattactgtaatttgacagcagaat
nsp9	Gaaattaatacgactcactatagggagaccacaacggtttccctctagaaataattttgtttaactttaagaaggagatatacca	Ggattagttattcattattgtagacgtactgtggcag
nsp10	Gaaattaatacgactcactatagggagaccacaacggtttccctctagaaataattttgtttaactttaagaaggagatatacca	Ggattagttattcattactgaagcatgggttcgcggga
nsp12	Gaaattaatacgactcactatagggagaccacaacggtttccctctagaaataattttgtttaactttaagaaggagatatacca	Ggattagttattcattactgtaagactgtatgcggtg
nsp13	Gaaattaatacgactcactatagggagaccacaacggtttccctctagaaataattttgtttaactttaagaaggagatatacca	Ggattagttattcattattgtaaagttgccacattcc
nsp14	Gaaattaatacgactcactatagggagaccacaacggtttccctctagaaataattttgtttaactttaagaaggagatatacca	Ggattagttattcattactgaagtcttgtaaaagtgt
nsp15	Gaaattaatacgactcactatagggagaccacaacggtttccctctagaaataattttgtttaactttaagaaggagatatacca	Ggattagttattcattattgtaattttgggtaaaatg
nsp16	Gaaattaatacgactcactatagggagaccacaacggtttccctctagaaataattttgtttaactttaagaaggagatatacca	Ggattagttattcattagttgttaacaagaacatcac
Spike protein S1	Gaaattaatacgactcactatagggagaccacaacggtttccctctagaaataattttgtttaactttaagaaggagatatacca	Ggattagttattcattagtgatggtgatggtgatgacgtgcccgccgaggagaat
Spike protein S2	Gaaattaatacgactcactatagggagaccacaacggtttccctctagaaataattttgtttaactttaagaaggagatatacca	Ggattagttattcattagtgatggtgatggtgatgtgtgtaatgtaatttgactc
orf3a	Gaaattaatacgactcactatagggagaccacaacggtttccctctagaaataattttgtttaactttaagaaggagatatacca	Ggattagttattcattagtgatggtgatggtgatgcaaaggcacgctagtag
E protein	Gaaattaatacgactcactatagggagaccacaacggtttccctctagaaataattttgtttaactttaagaaggagatatacca	Ggattagttattcattagaccagaagatcaggaa
M protein	Gaaattaatacgactcactatagggagaccacaacggtttccctctagaaataattttgtttaactttaagaaggagatatacca	Ggattagttattcattactgtacaagcaaagcaa
orf6	Gaaattaatacgactcactatagggagaccacaacggtttccctctagaaataattttgtttaactttaagaaggagatatacca	Ggattagttattcattaatcaatctccattggtt

orf7a	Gaaattaatacgactcactatagggagaccacaa cggtttccctctagaaataattttgtttaactttaagaa ggagatatacca	Ggattagttattcattattctgtctttcttttga
orf7b	Gaaattaatacgactcactatagggagaccacaa cggtttccctctagaaataattttgtttaactttaagaa ggagatatacca	Ggattagttattcattaggcgtgacaagtttcat
orf8	Gaaattaatacgactcactatagggagaccacaa cggtttccctctagaaataattttgtttaactttaagaa ggagatatacca	Ggattagttattcattagatgaaatctaaaacaa
N protein	Gaaattaatacgactcactatagggagaccacaa cggtttccctctagaaataattttgtttaactttaagaa ggagatatacca	Ggattagttattcattaggcctgagttgagtcag
orf10	Gaaattaatacgactcactatagggagaccacaa cggtttccctctagaaataattttgtttaactttaagaa ggagatatacca	Ggattagttattcattatgtgagattaaagttaa

2-3. Detection of purified His-tagged SARS-CoV-2 recombinant proteins by SDS-PAGE

On ice box, bovine serum albumin (BSA; stock concentration of 10 µg/µl) as a standard was serially diluted with phosphate buffered saline (PBS) to 500, 250, 125, and 62.5 ng/µl. 10 µl of 2 x SDS-PAGE sample buffer (0.125M Tris-HCl, 4w/v% SDS, 20w/v% Glycerol, 0.002w/v% BPB, 10vol% 2-ME (a reducing agent to dissociate the proteins from Dynabeads), pH6.8) was added to 10 µl of the standard or His-tagged SARS-CoV-2 recombinant protein in a DNA LoBind® tube. Each sample or standard was heated at 95ºC for 5 min, and immediately put on ice. And 20 µl of protein, standard, and 4 µl of XL-ladder broad (APRO, #SP2120) were loaded onto a Multigel® II mini 4/20 (13W) (Cosmo Bio Co., LTD., #414879) and electrophoresed in 1 x SDS-PAGE running buffer (25 mM Tris, 192 mM glycine, 0.1%(w/v) SDS) at 140 V, 30 mA for 1.5 hrs. The gel was washed with milli-Q water, with shaking at a reciprocating type shaker, speed 30 on a shaker Wave-SI (TAITEC, #0054334-000) for 5 min three times, followed by Coomassie Brilliant Blue (CBB; Nacalai Tesque, #1164231) staining with further shaking for 30 min, covering with aluminum foil for light shielding. The gel was then washed with milli-Q water for 30 min twice in the same shaking condition. The stained protein bands were detected by Bio-Rad chemotic™ touch imaging system, and the analysis was done by Image lab software 2020 (Bio-Rad laboratories).

2-4. Peripheral blood mononuclear cells (PBMCs) isolation and *ex vivo* stimulation with SARS-CoV-2 recombinant proteins with Dynabeads

Fresh blood samples from a total number of 5 healthy volunteers and 1 recovered donor from COVID-19 (Mild case) were heparinized. The samples were collected under the approval of clinical research IRB No. 020-0094 in Hokkaido University. Ficoll-Paque™ PLUS (Cytiva; #17-1440-02) was inverted several times to ensure mixing of the content. 3 ml of Ficoll-Paque PLUS was added in 15 ml polypropylene conical tube (Corning, Falcon®, #352096), and 5 ml of heparin-treated blood samples were then carefully layered onto. The tubes were centrifuged at 400 x g for 20 min at 18 °C by Hitachi CF7D2 himac CENTRIFUGE. Each PBMC layer was separately transferred to a clean 50 mL polypropylene conical tube (Corning, Falcon®, #352070) containing 30 ml of PBS, and suspended by gently pipetting using a clean transfer pipette. Then PBS was added up to 50 ml, and the PBMCs were centrifuged at 400 x g for 5 min at 4°C. After discarding the supernatant, the PBMCs were resuspended in 10 ml of RP10 medium (RPMI medium 1640 basic (1 x) (Thermo Fisher Scientific, Gibco™, #C11875500BT) containing 10% heat-inactivated fetal bovine serum (FBS; GE Healthcare, HyClone™, #SH30910.03) and 50 µM 2-mercaptoethanol (Nacalai Tesque, #21417)), transferred to a new 15 ml polypropylene conical tube, and centrifuged at 400 x g for 5 min at 4°C. The PBMCs were then resuspended in 5 ml of RP10 medium to count the cell numbers using hemocytometer. 1 x 10^5 cells were seeded on U-bottom 96 well-plate (Corning, Falcon®, #353077) at 200 µl per well using a multichannel pipette. And 1 µl of respective SARS-CoV-2 recombinant protein (NSP1,2,5,7,8,9,10,11,12,13,14,15,16, S1, S2, Orf3a, E, M, N, Orf6, Orf7a,7b, Orf8, Orf10) bound to Dynabeads was added to the well and mixed with the cells. 0.5 µl of CD3 and CD28 antibody each, or Dynabeads only (without protein) or medium only (without stimulation) was added to the well, as a positive or negative control for T-cell activation. The cells were incubated in an incubator (Panasonic Healthcare, model: MCO-175) at 37°C, 5% CO_2 for 4 or 6 days for the samples of recovered patients from COVID-19 for an experimental setting and optimization, and for 6 days for the samples of healthy donors.

2-5. Flow cytometric analysis of PBMCs

In the culture of PBMCs, 150 µl of cultured medium was aspirated carefully without disturbing the cells. And 100 µl of 5 mM ethylenediaminetetraacetic acid (EDTA) in PBS was added, and the cells were gently mixed by pipetting and left for 5 min at room temperature on a magnetic field.

The PBMCs away from the Dynabeads were then transferred to V-bottom 96-well plate, carefully. This step was repeated twice to collect almost all PBMCs. The cells were centrifuged at 400 x g, at 4°C for 5 min, and resuspended in 200 µl of MACS buffer (0.5% FBS and 2 mM EDTA in PBS) containing Brilliant Violet (BV)510-conjugated anti-human CD3 (clone: OKT3, BioLegend, #317332), BV650-anti-CD4 (clone: RPA-T4, BD Biosciences, #740563), BV421-anti-human CD8 (clone: RPA-T8, BD Biosciences, #562428), Alexa fluor (AF)488-conjugated anti-human CD19 (clone: HIB19, BioLegend, #302219), phycoerythrin (PE)-conjugated anti-human CD137 (clone: 4B4-1, BioLegend, #309804), and allophycocyanin (APC)-conjugated anti-human OX40 (clone: Ber-ACT35, BioLegend, #350008), diluted to 1:100. The cells were covered with aluminum foil and incubated for 30 min on ice. The cells were washed twice with 200 µL of MACS buffer, pipetted, and then centrifuged at 400 x g for 3 min at 4ºC. After discarding the supernatant, the cells were resuspended in 200 µl of MACS buffer, and subjected to flowcytometric analysis using CytoFLEX S (Beckman Coulter Life Sciences) to examine the activation status of $CD4^+$ T-cells. Data analysis was carried out by FlowJo™ 10 software (BD Biosciences).

3. Results

3-1. Detection of synthesized and purified His-tagged SARS-CoV-2 recombinant proteins by SDS-PAGE

In my doctoral research, I aimed at investigating the immunodominance of SARS-CoV-2 proteins using the 24 viral proteins synthesized *in vitro* and *ex vivo* stimulation system. The synthesis of His-tagged recombinant viral proteins; NSP1,2,5,7,8,9,10,11,12,13,14,15,16, S1, S2, Orf3a, E, M, N, Orf6, 7a, 7b, 8, and 10, were made using the PURExpress® kit, a reconstituted coupled transcription and translation system, and isolated by Dynabeads-based pulldown method. **(Fig. 5)**, shows Detection of some of synthesized and purified His-tagged SARS-CoV-2 recombinant proteins by SDS-PAGE.

3-2. The reactivity of AIM^+CD4^+ T-cells of Recovered donor from COVID-19 (Mild case), to each His-tagged SARS-CoV-2 recombinant protein with Dynabeads and control condition.

Using the purified viral proteins, I first optimized the culture conditions by examining the reactivity of $CD4^+$ T-cells of Recovered donor from COVID-19 (mild case), to each viral component. Fresh PBMCs were isolated from heparinized blood. The PBMCs were isolated using Ficoll-Paque plus then were washed with 200 µl of RP10 medium containing 10% FBS, and seeded at 1 x 10^5 cells per well of U-bottom 96-well plate. The PBMCs were incubated with 1µl of His-tagged SARS-CoV-2 recombinant protein with Dynabeads or with 0.5 µl of CD3/CD28 activator as a positive control for PBMCs stimulation or with 1 µl of Dynabeads only (protein-) or without stimulation (medium) for a culture period either at 4-days or 6-days in 5% CO_2 incubator for 37ºC.

Following the Dynabeads removal using magnetic plate, the PBMCs were collected and stained with antibodies against CD3, CD4, CD8, CD19, CD137 and OX40 at the concentration of 1/100 diluted in MACS buffer. The PBMCs were incubated for 30 min on ice, then washed 3 times by adding 200 µl of MACS buffer, and resuspended finally in 200 µl of MACS buffer.

Activated AIM^+CD4^+ T-cells percentage was evaluated by flow cytometric analysis (CytoFLEX S). Data analysis was carried out by FlowJo 10 software. The gating strategy used for identification of activated AIM^+CD4^+ T-cells gated as singlets, $CD3^+CD19^-CD4^+CD8^-CD137^+OX40^+$ lymphocyte population, is shown in **Fig. 6**.

The results of activated AIM^+CD4^+ T-cells plots has been shown for each of His-tagged SARS-CoV-2 recombinant protein with Dynabeads or control conditions (CD3/CD28 activator, Dynabeads (protein-), or medium only (without stimulation)) following 4- or 6-days of PBMCs.

with NSPs after 4- or 6-days (**Fig. 7 and 8)** and for SPs and control conditions after 4- or 6-days **(Figure 9 and 10)**.

In 24 His-tagged SARS-CoV-2 recombinant proteins with Dynabeads and control conditions, we found that 6-days of culture give differences in AIM^+CD4^+ T-cells % among the different protein stimulated conditions, especially with NSP1, 2, 5, 7, 10, 11, 16, Orf3a, and M. And expectedly the AIM^+CD4^+ T-cells % stimulated with CD3/CD28 activator reduced after 6-days, probably due to apoptosis of overstimulated PBMCs **(Fig. 11)**.

3-3. The reactivity of AIM^+CD4^+ T-cells of Healthy donors to each His-tagged SARS-CoV-2 recombinant protein with Dynabeads and control condition.

On 6-days culture of healthy donors-derived fresh PBMCs (n=5), the representative dot blots might show differences in percentage of AIM^+CD4^+ T-cells stimulated with either NSPs (**Fig. 12,14,16,18,20**) or SPs (**Fig. 13,15,17,19,21**). **Fig. 22** shows the collective data of AIM^+CD4^+ T-cells from 5 healthy donors, that were stimulated with each protein and controls. Using two tailed student t-test (paired), we found that the stimulations with NSPs cause highly significant increase in AIM^+CD4^+ T-cells %, in comparison to those with SPs, P-value<0.0001 (**Fig. 23)**.

It has been shown that AIM^+CD4^+ T-cells reactivity in culture with NSPs and SPs is not significantly increased (P-value=0.18 and 0.62, respectively), in comparison to the culture with Dynabeads only (Protein-) **Fig. 24** which could not be enough for statistically analysis to get results, because of the limited number of healthy donors.

Altogether, these data suggest that SARS-CoV-2 proteins were successfully synthesized and purified using a cell-free protein synthesis system. AIM^+CD4^+ T cells reactivity to SARS-CoV-2 NSPs is more than SPs in PBMCs culture of unexposed healthy donors.

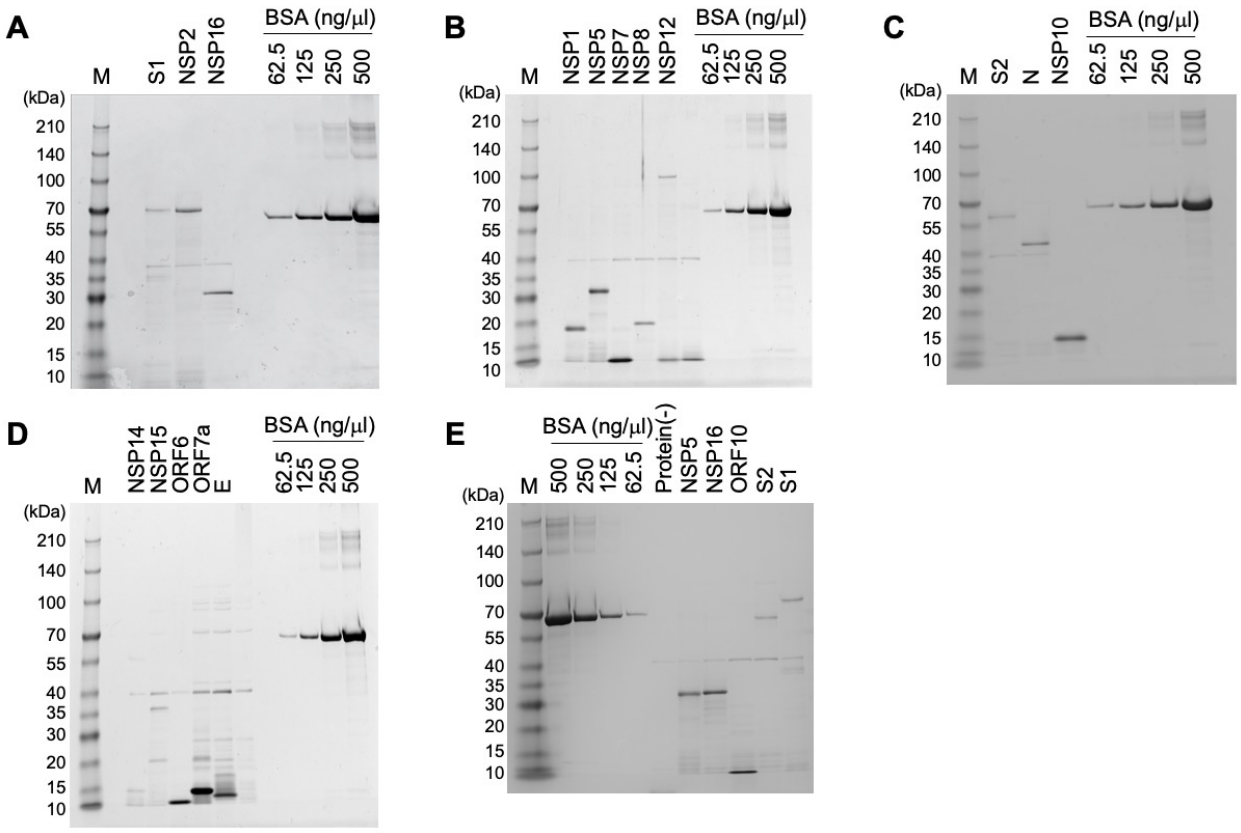

Fig. 5: *in vitro* synthesis of some of His-tagged SARS-CoV-2 recombinant proteins

The recombinant proteins of each SARS-CoV-2 component were obtained by *in vitro* translation and purification. The synthesized proteins were subjected to SDS-PAGE, followed by CBB staining. **(A**) S1, NSP2, and NSP16, (**B)** NSP1, 5, 7, 8, and 12, **(C)** S2, N, and NSP10, (**D)** NSP14, 15, ORF6, ORF7a, and E protein, and **(E)** Dynabeads only (protein-), NSP5, 16, ORF10, S2, S1proteins are shown. A protein ladder marker was loaded on the well at the left side. BSA serially diluted to 500, 250, 125, and 62.5 ng/ μ l was used for standards to estimate protein concentration of the synthesized viral components *in vitro*. The proteins which are not exist here have been done by other staff.

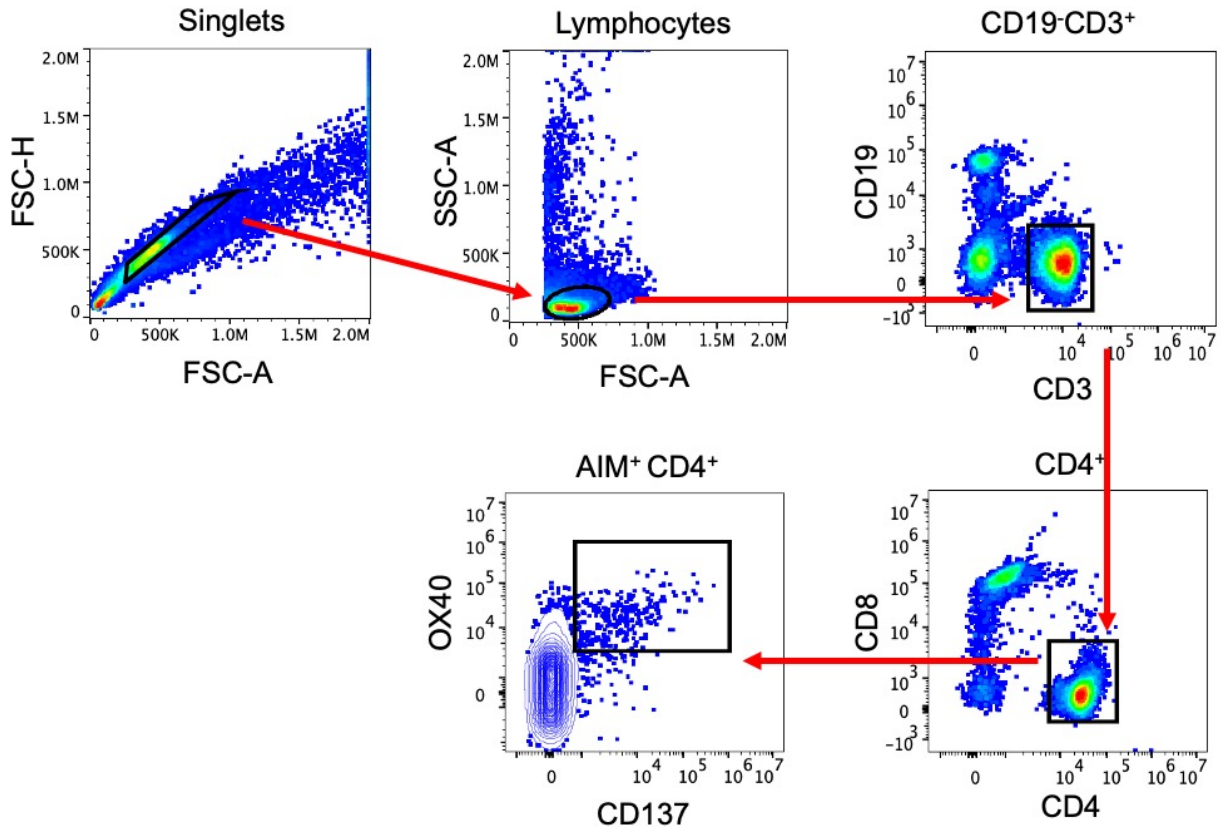

Fig. 6: Gating strategy

The gating strategy used to evaluate the activation status of $CD4^+$ T cells from healthy donors and people recovered from COVID-19 is shown. Following PBMCs culture in the presence of SARS-CoV-2 components, the cells were stained with antibodies specific for human CD3, 4, 8, 19, OX40, and CD137 and analyzed by flow cytometry. The $CD4^+$ T cells co-expressing OX40 and CD137 show activated status.

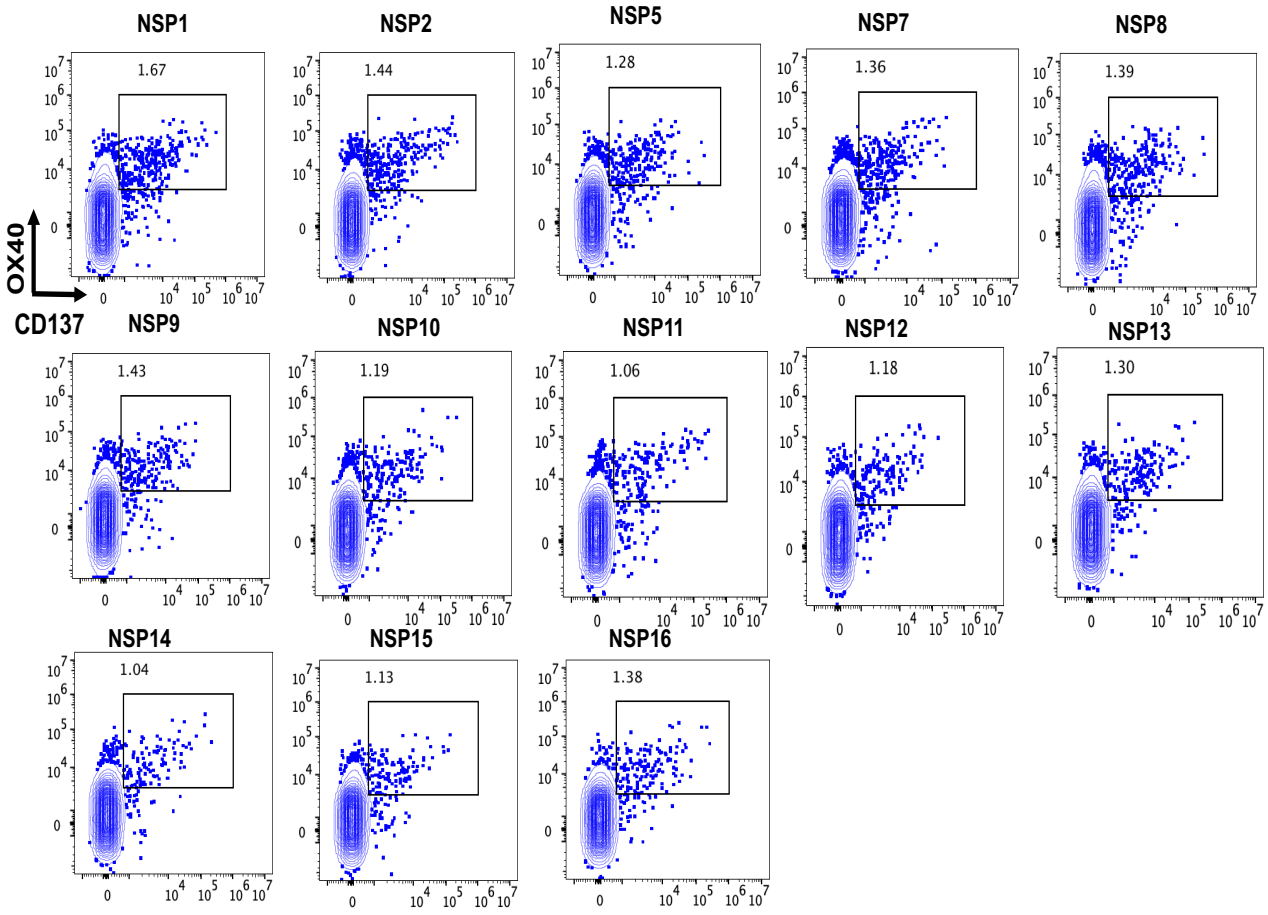

Fig. 7: Optimization of culture condition to examine an activation status of $CD4^+$ T-cells to NSPs in culture of PBMCs from COVID-19-recovered donor (Mild case) after 4-days.

Fresh PBMCs from the blood sample of one recovered COVID-19 donor (n=1) were isolated using Ficoll-Paque PLUS, and stimualted with the indicated SARS-CoV-2 protein components for 4-days. Gating plots show the activated AIM^+ $CD4^+$Tcells population in $CD3^+CD4^+CD8^-CD19^-$ cells

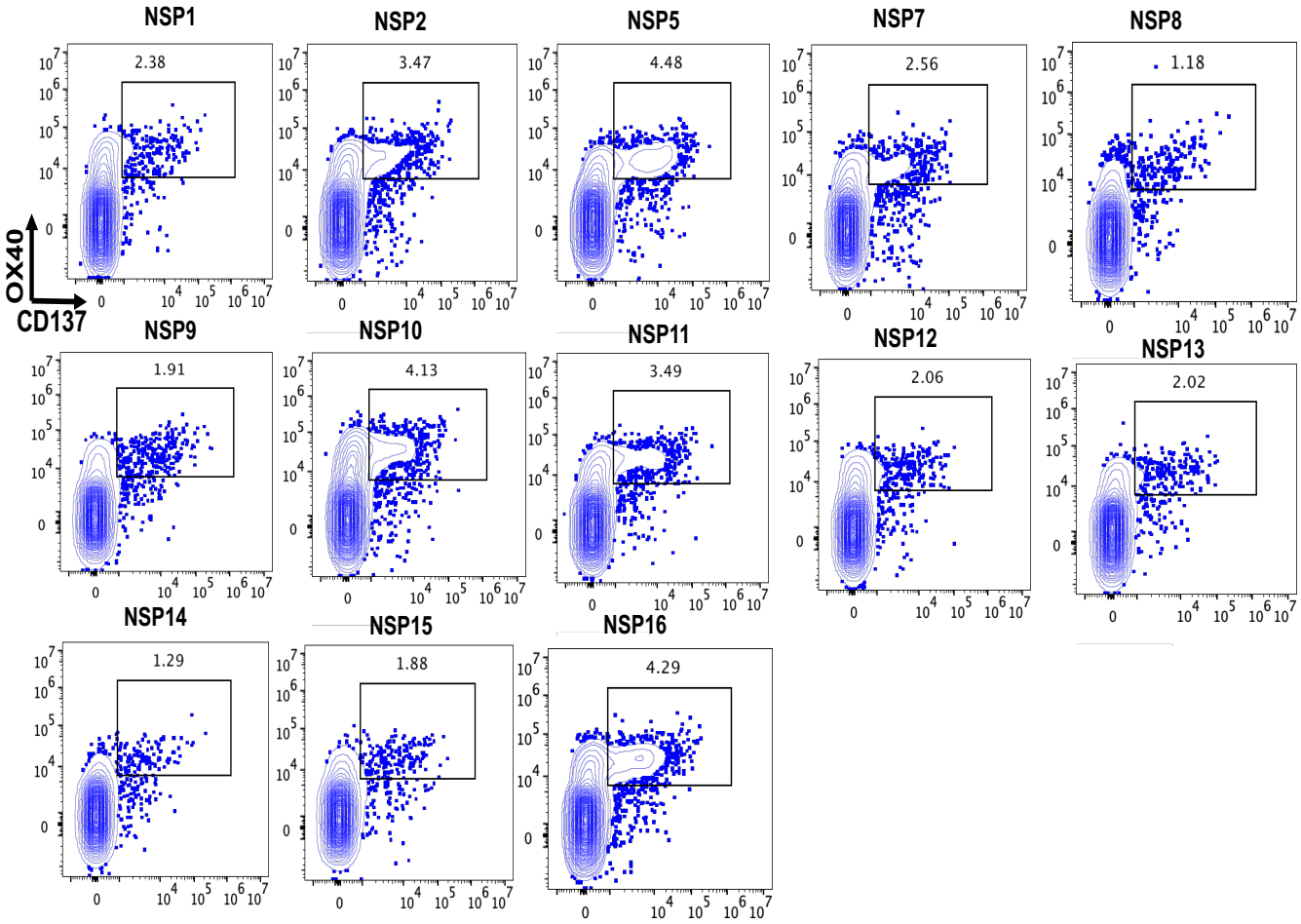

Fig. 8: Optimization of culture condition to examine an activation status of CD4^{+} T cells to NSPs in culture of PBMCs from COVID-19 recovered donor (Mild case) after 6-days.

Fresh PBMCs from the blood sample of one recovered COVID-19 donor (n=1) were isolated using Ficoll-Paque PLUS, and stimualted with the indicated SARS-CoV-2 protein components for 6-days. Gating plots show the activated AIM^{+} CD4^{+}Tcells population in CD3^{+}CD4^{+}CD8^{-}CD19^{-} cells

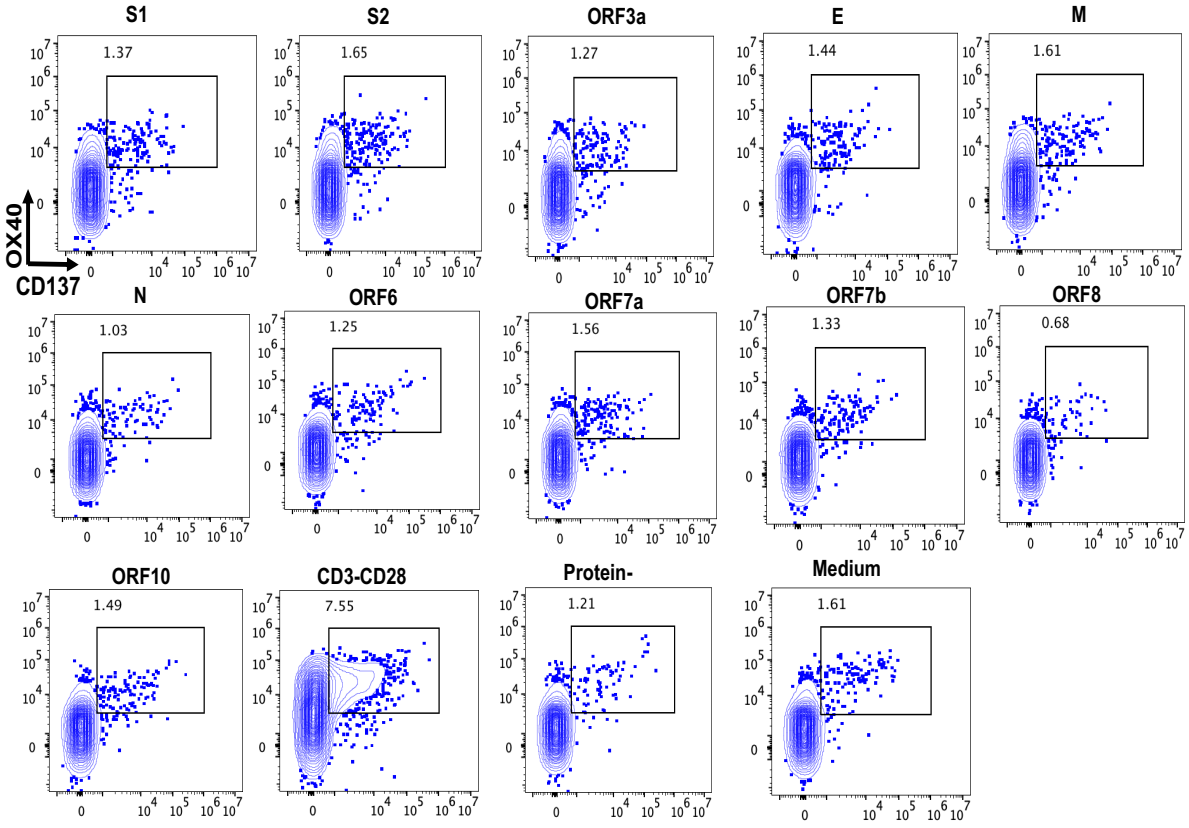

Fig. 9: Optimization of culture condition to examine an activation status of CD4$^+$ T cells to SPs in culture of PBMCs from COVID-19 recovered donor (Mild case) after 4-days.

Fresh PBMCs from the blood sample of one recovered COVID-19 donor (n=1) were isolated using Ficoll-Paque PLUS, and stimualted with the indicated SARS-CoV-2 protein components for 4-days. Gating plots show the activated AIM$^+$ CD4$^+$T-cells population in CD3$^+$CD4$^+$CD8$^-$CD19$^-$ cells. CD3/CD28: positive control, protein (-): Dynabeads only as a negative control, Medium: no-Dynabeads and no-protein as a negative control.

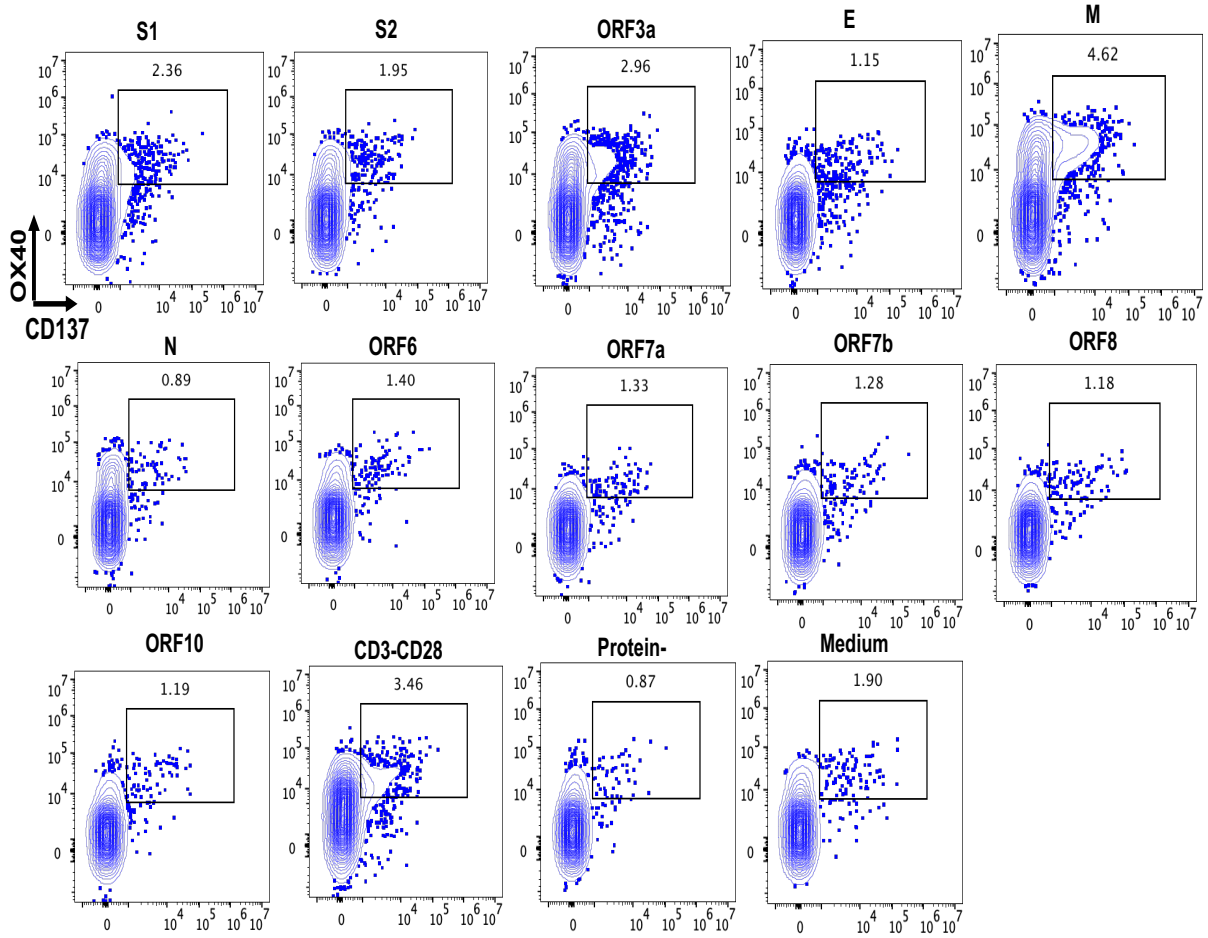

Fig. 10: Optimization of culture condition to examine an activation status of CD4$^+$ T-cells to SPs in culture of PBMCs from COVID-19 recovered donor (Mild case) after 6-days.

Fresh PBMCs from the blood sample of one recovered COVID-19 donor (n=1) were isolated using Ficoll-Paque PLUS, and stimualted with the indicated SARS-CoV-2 protein components for 6-days. Gating plots show the activated AIM$^+$ CD4$^+$T-cells population in CD3$^+$CD4$^+$CD8$^-$CD19$^-$ cells. CD3/CD28: positive control, protein (-): Dynabeads only as a negative control, Medium: no-Dynabeads and no-protein as a negative control.

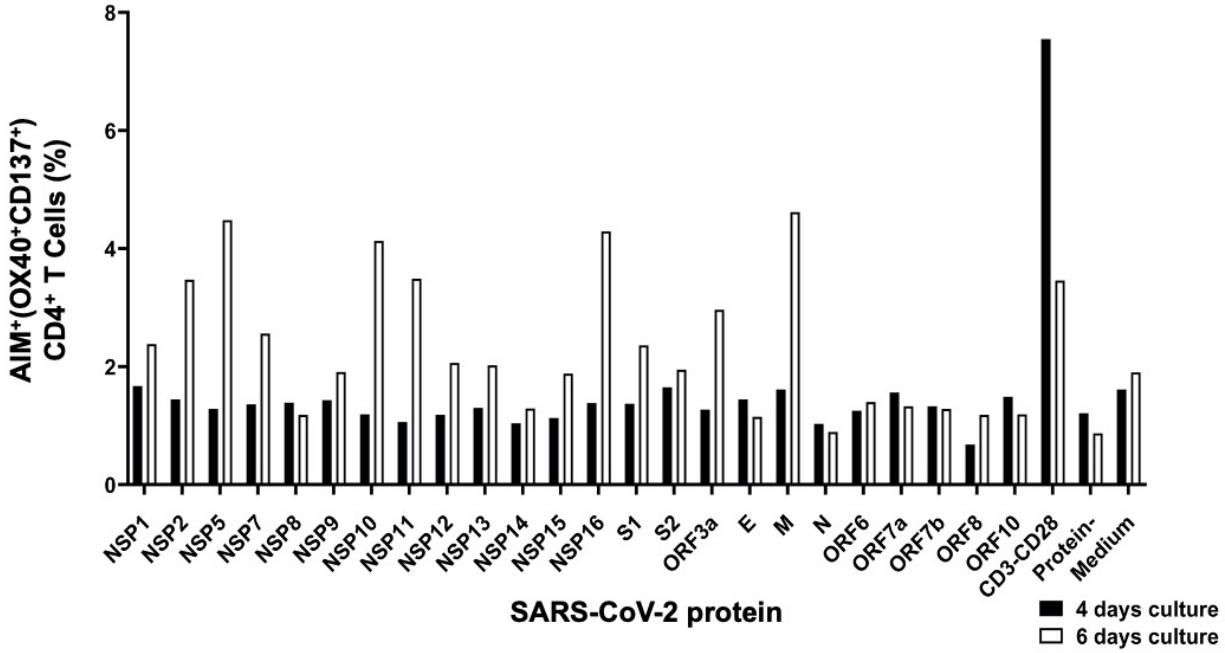

Fig. 11: Optimization of culture condition to examine an activation status of $CD4^+$ T-cells in PBMCs from COVID-19 recovered donor (Mild case).

Fresh PBMCs from the blood sample of one recovered donor COVID-19 (n=1) were isolated using Ficoll-Paque PLUS, and stimualted with the indicated SARS-CoV-2 protein components for either 4- or 6-days. The AIM^+ population in whole $CD4^+$ T-cells after the stimulation is shown in each column. CD3/CD28: positive control, protein (-): Dynabeads only as a negative control, Medium: no-Dynabeads and no-protein as a negative control.

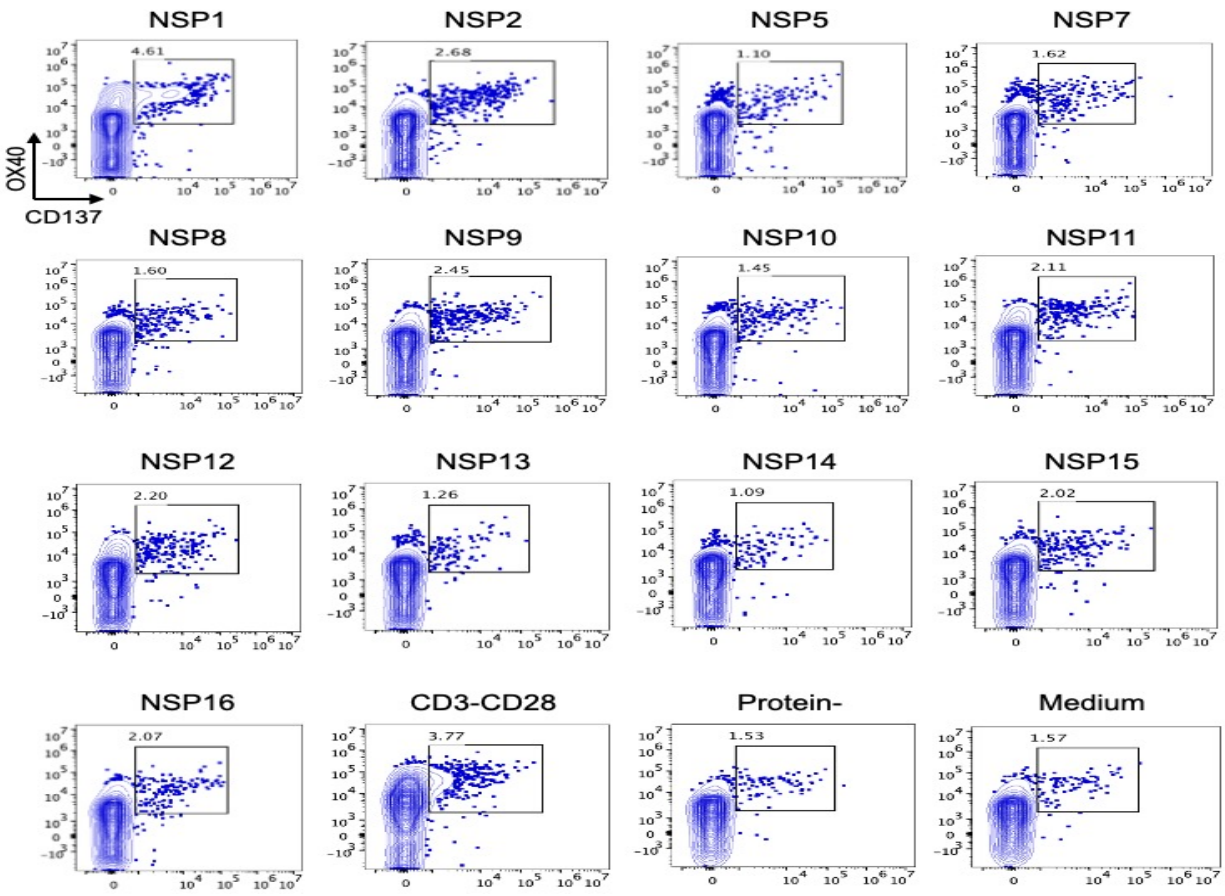

Fig. 12: Reactivity of pre-existing $CD4^+$ T-cells in PBMCs of healthy donor 1 (H1) against SARS-CoV-2 NSPs

The PBMCs from healthy donor (1) were activated in the presence of SARS-CoV-2 NSPs bound to Dynabeads for 6-days. Gating plots show the activated AIM^+CD4^+ T-cell population in $CD3^+CD4^+CD8^-CD19^-$ cells. CD3/CD28: positive control, protein (-): Dynabeads only as a negative control, Medium: no-Dynabeads and no-protein as a negative control

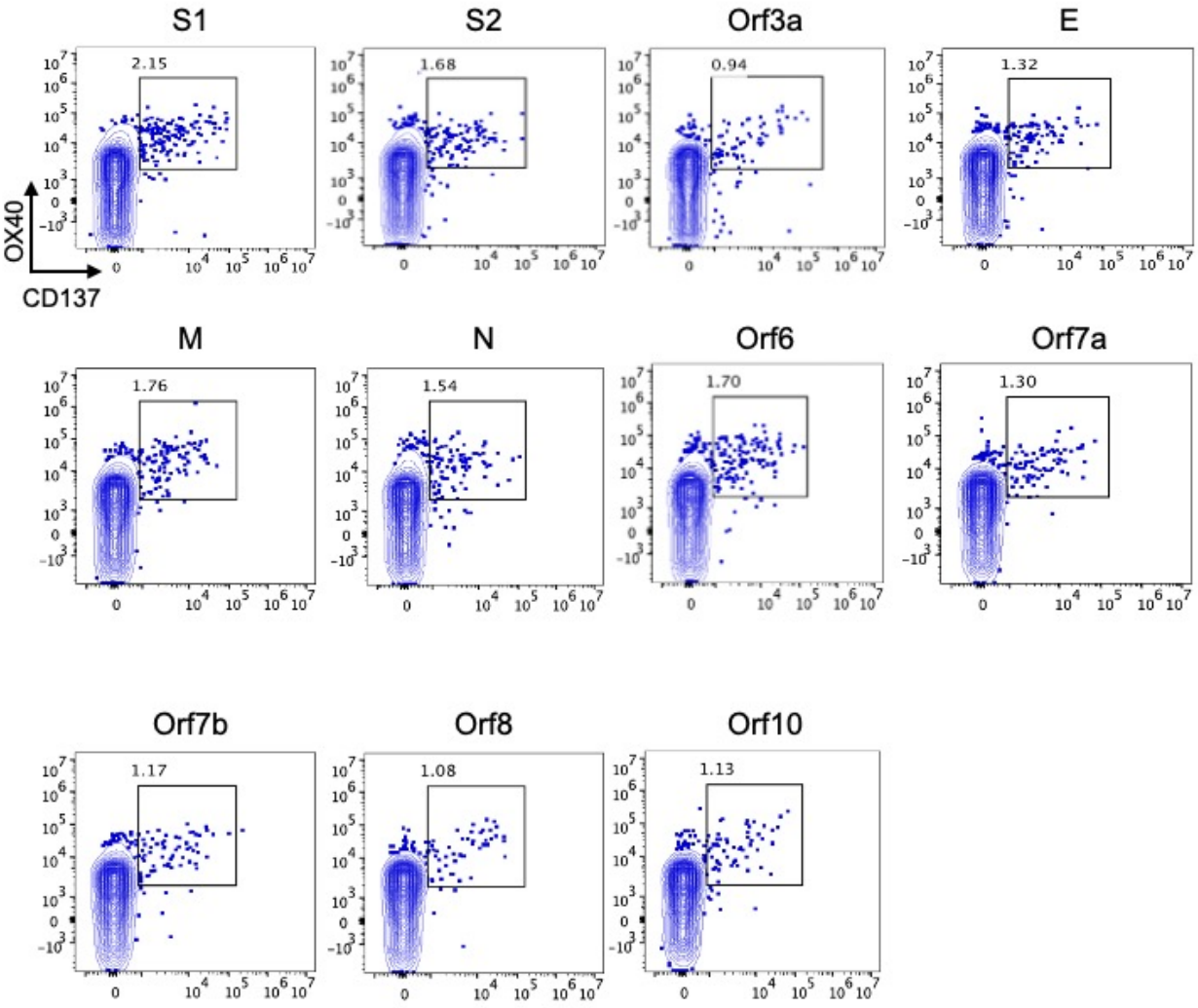

Fig. 13: Reactivity of pre-existing $CD4^+$ T cells in PBMCs of healthy donor 1 (H1) against SARS-CoV-2 SPs

The PBMCs from healthy donor (1) were activated in the presence of SARS-CoV-2 SPs bound to Dynabeads for 6-days. Gating plots show the activated AIM^+CD4^+ T-cell population in $CD3^+CD4^+CD8^-CD19^-$cells.

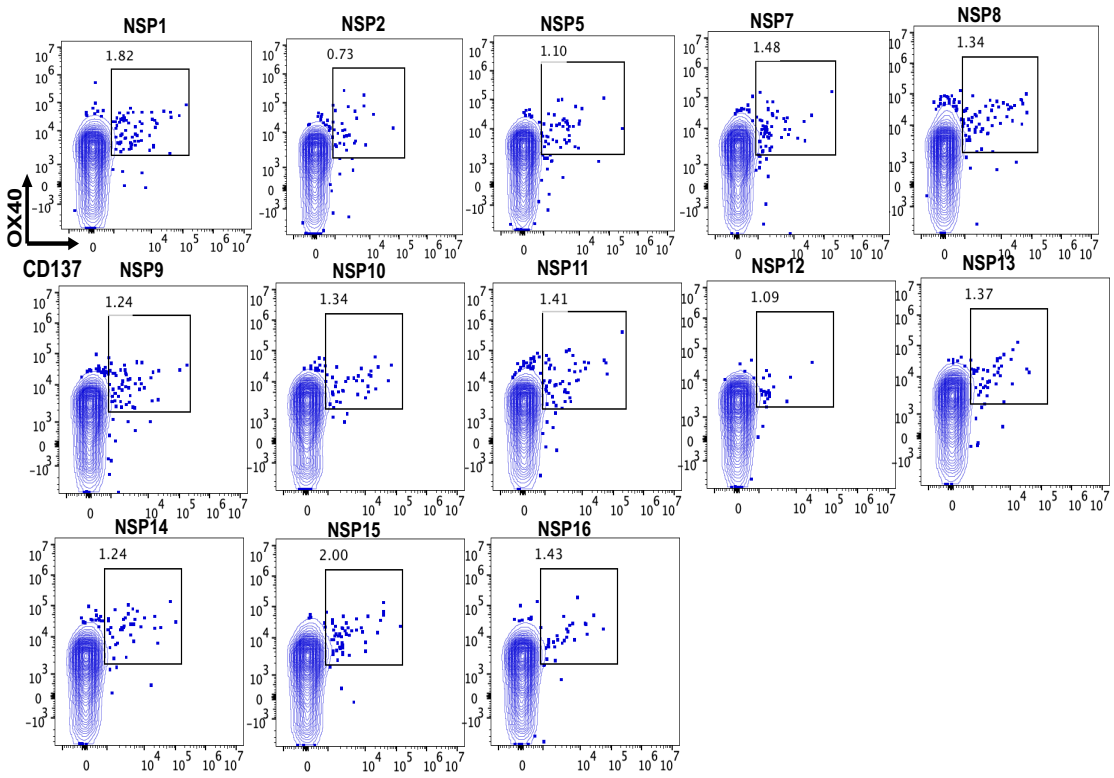

Fig. 14: Reactivity of pre-existing CD4$^+$ T-cells in PBMCs of healthy donor 2 (H2) against SARS-CoV-2 NSPs

The PBMCs from healthy donor (2) were activated in the presence of SARS-CoV-2 NSPs bound to Dynabeads for 6-days. Gating plots show the activated AIM$^+$CD4$^+$ T-cell population in CD3$^+$CD4$^+$CD8$^-$CD19$^-$ cells.

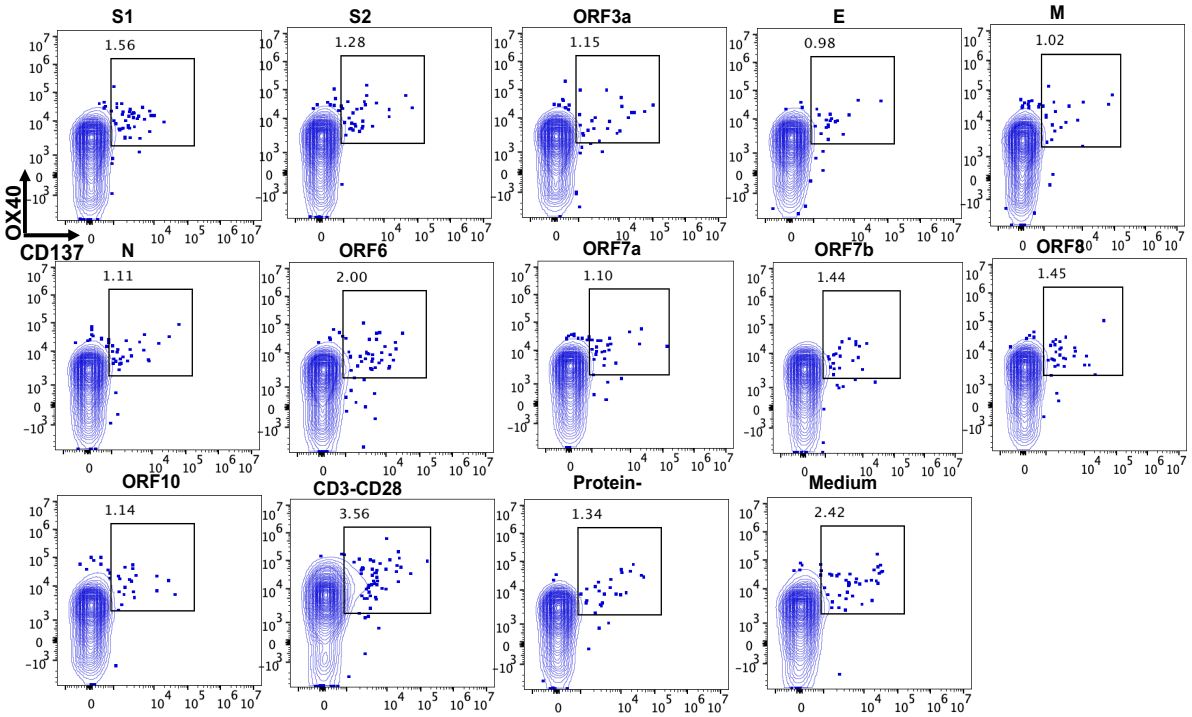

Fig. 15: Reactivity of pre-existing CD4$^+$ T-cells in PBMCs of healthy donor 2 (H2) against SARS-CoV-2 SPs

The PBMCs from healthy donor (2) were activated in the presence of SARS-CoV-2 SPs bound to Dynabeads for 6-days. Gating plots show the activated AIM$^+$CD4$^+$ T-cell population in CD3$^+$CD4$^+$CD8$^-$CD19$^-$cells. CD3/CD28: positive control, protein (-): Dynabeads only as a negative control, Medium: no-Dynabeads and no-protein as a negative control

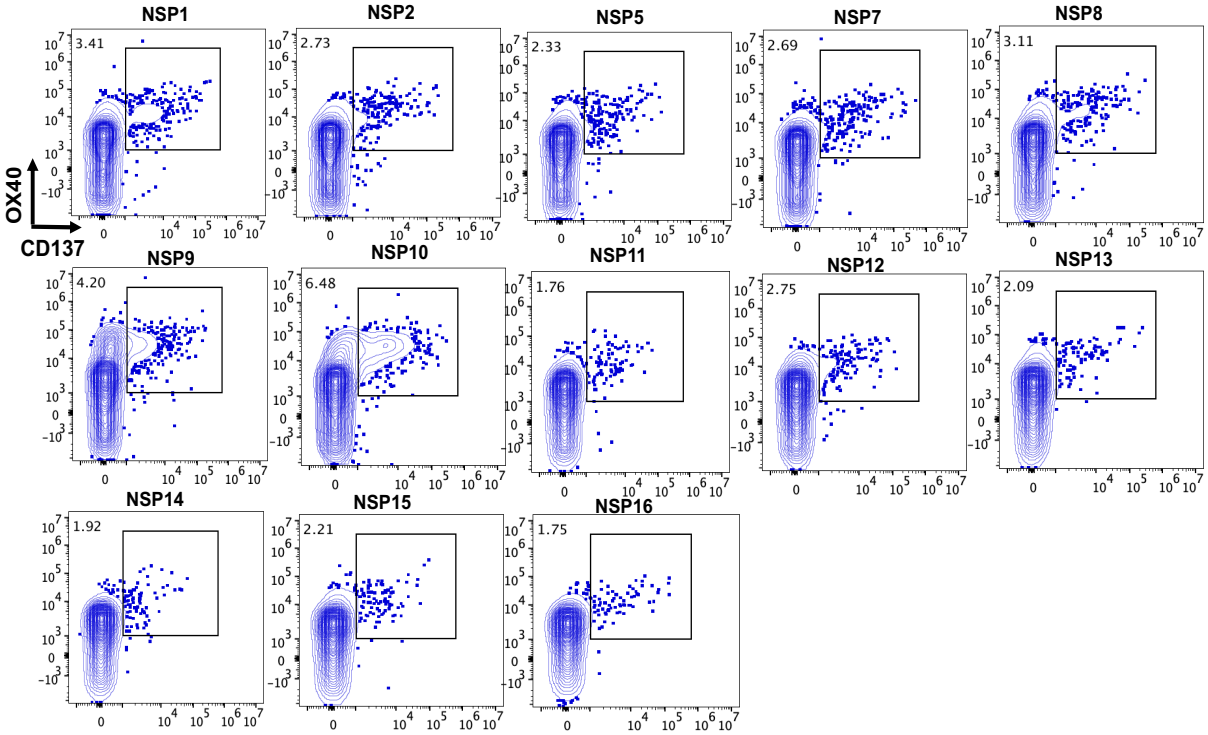

Fig. 16: Reactivity of pre-existing CD4$^+$ T-cells in PBMCs of healthy donor 3 (H3) against SARS-CoV-2 NSPs

The PBMCs from healthy donor (3) were activated in the presence of SARS-CoV-2 NSPs bound to Dynabeads for 6-days. Gating plots show the activated AIM$^+$CD4$^+$ T-cell population in CD3$^+$CD4$^+$CD8$^-$CD19$^-$ cells.

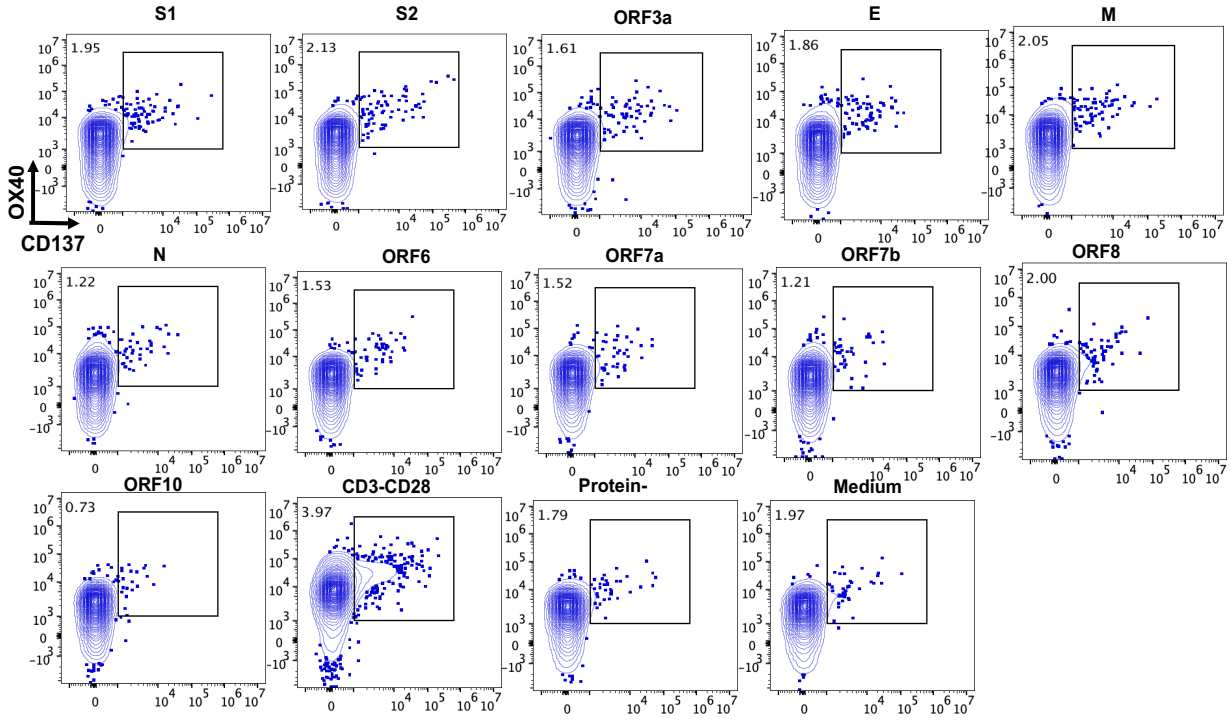

Fig. 17: Reactivity of pre-existing CD4$^+$ T cells in PBMCs of healthy donor 3 (H3) against SARS-CoV-2 SPs

The PBMCs from healthy donor (3) were activated in the presence of SARS-CoV-2 SPs bound to Dynabeads for 6-days. Gating plots show the activated AIM$^+$CD4$^+$ T-cell population in CD3$^+$CD4$^+$CD8$^-$CD19$^-$cells. CD3/CD28: positive control, protein (-): Dynabeads only as a negative control, Medium: no-Dynabeads and no-protein as a negative control

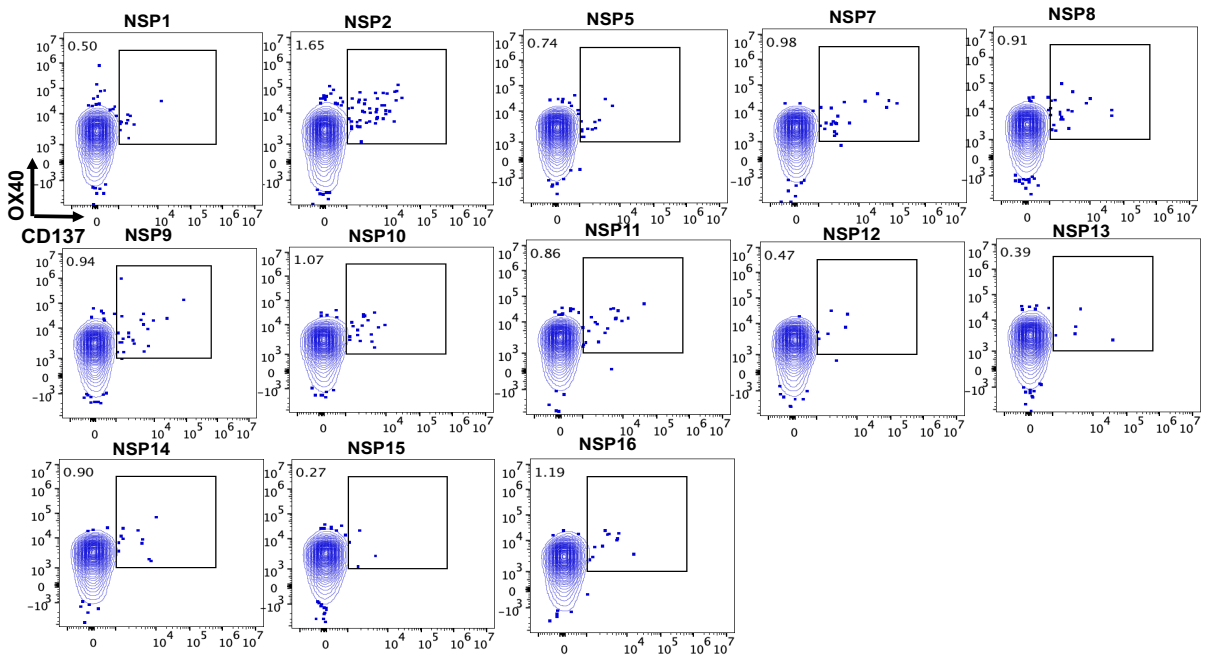

Fig. 18: Reactivity of pre-existing CD4$^+$ T-cells in PBMCs of healthy donor 4 (H4) against SARS-CoV-2 NSPs

The PBMCs from healthy donor (4) were activated in the presence of SARS-CoV-2 NSPs bound to Dynabeads for 6-days. Gating plots show the activated AIM$^+$CD4$^+$ T-cell population in CD3$^+$CD4$^+$CD8$^-$CD19$^-$ cells.

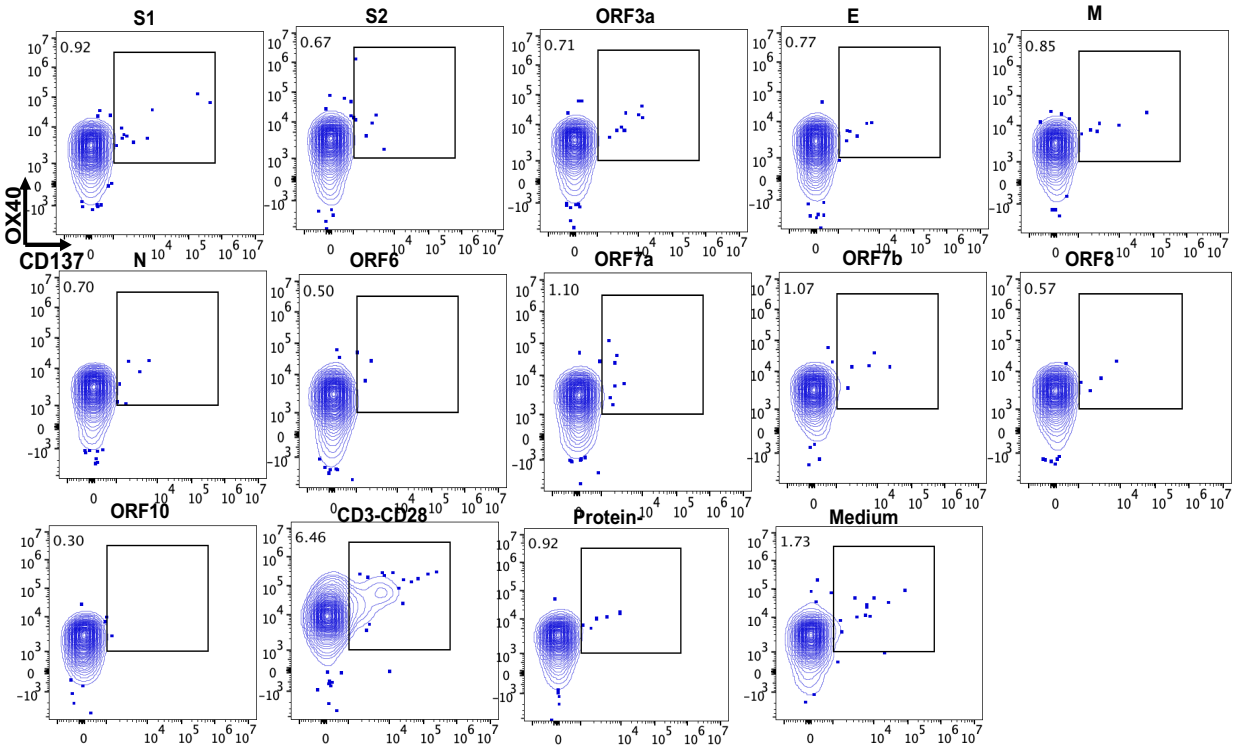

Fig. 19: Reactivity of pre-existing CD4$^+$ T cells in PBMCs of healthy donor 4 (H4) against SARS-CoV-2 SPs

The PBMCs from healthy donor (4) were activated in the presence of SARS-CoV-2 SPs bound to Dynabeads for 6-days. Gating plots show the activated AIM$^+$CD4$^+$ T-cell population in CD3$^+$CD4$^+$CD8$^-$CD19$^-$cells. CD3/CD28: positive control, protein (-): Dynabeads only as a negative control, Medium: no-Dynabeads and no-protein as a negative control

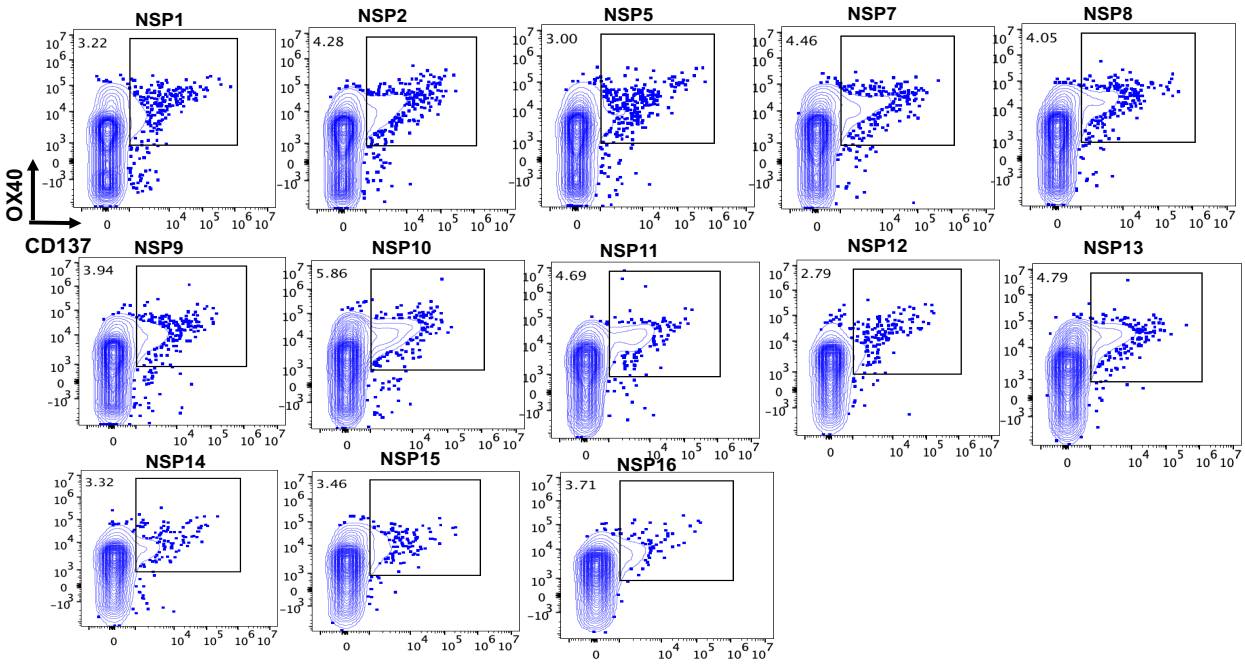

Fig. 20: Reactivity of pre-existing CD4$^+$ T-cells in PBMCs of healthy donor 5 (H5) against SARS-CoV-2 NSPs

The PBMCs from healthy donor (5) were activated in the presence of SARS-CoV-2 NSPs bound to Dynabeads for 6-days. Gating plots show the activated AIM$^+$CD4$^+$ T-cell population in CD3$^+$CD4$^+$CD8$^-$CD19$^-$ cells.

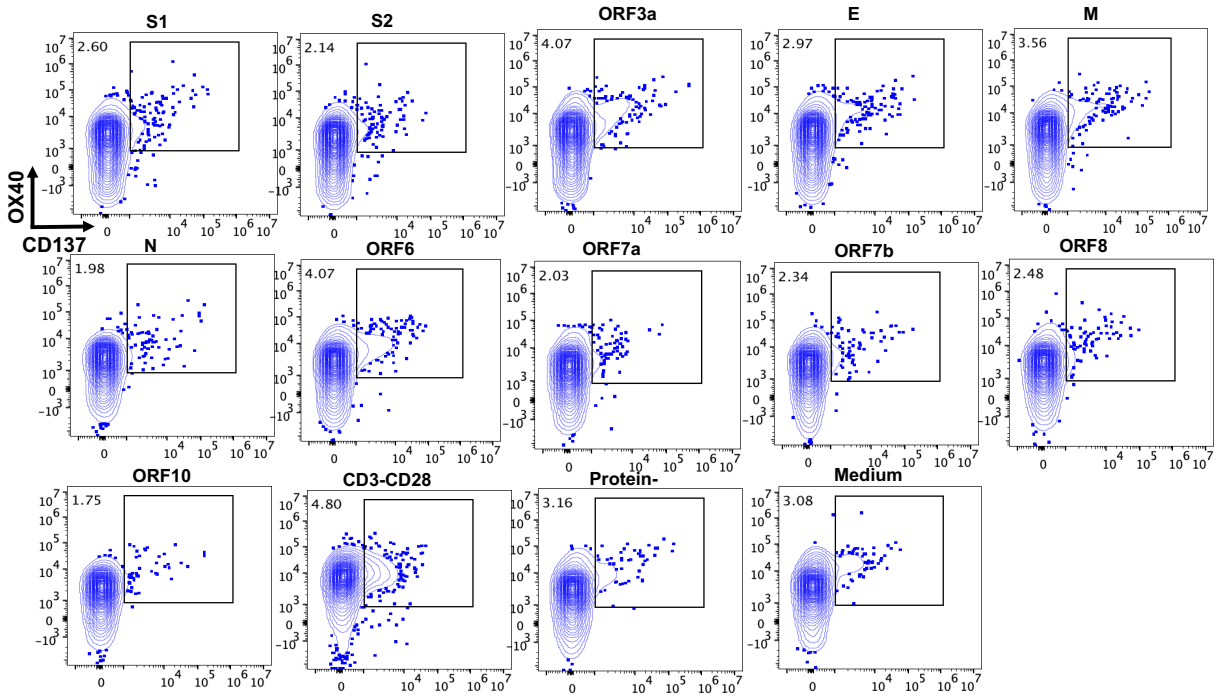

Fig. 21: Reactivity of pre-existing CD4$^+$ T cells in PBMCs of healthy donor 5 (H5) against SARS-CoV-2 SPs

The PBMCs from healthy donor (5) were activated in the presence of SARS-CoV-2 SPs bound to Dynabeads for 6-days. Gating plots show the activated AIM$^+$CD4$^+$ T-cell population in CD3$^+$CD4$^+$CD8$^-$CD19$^-$cells. CD3/CD28: positive control, protein (-): Dynabeads only as a negative control, Medium: no-Dynabeads and no-protein as a negative control

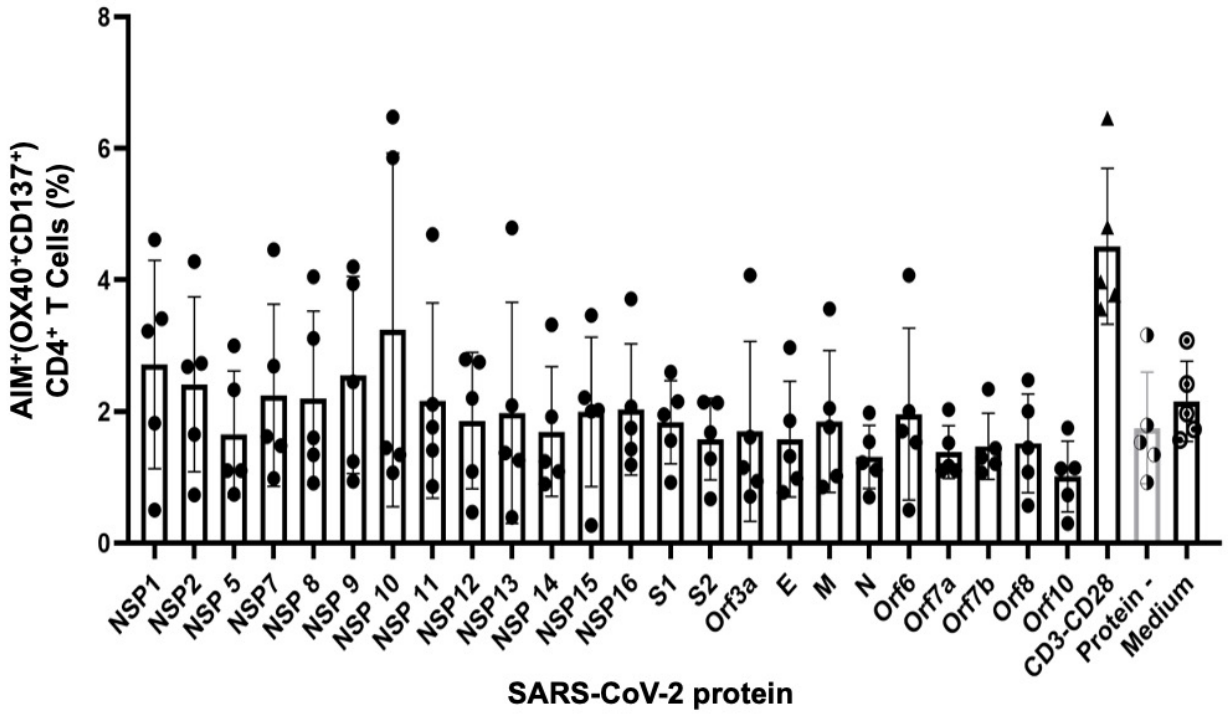

Fig. 22: AIM$^+$CD4$^+$ T-cell population activated by SARS-CoV-2 protein in healthy donors

Fresh PBMCs from the blood samples of heathy donors (n=5) were isolated using Ficoll-Paque PLUS, and stimualted with the indicated SARS-CoV-2 protein components for 6-days. The AIM$^+$ population in whole CD4$^+$ T-cells after the stimulation is shown for each protein. CD3/CD28: positive control, protein (-): Dynabeads only as a negative control, Medium: no-Dynabeads and no-protein as a negative control

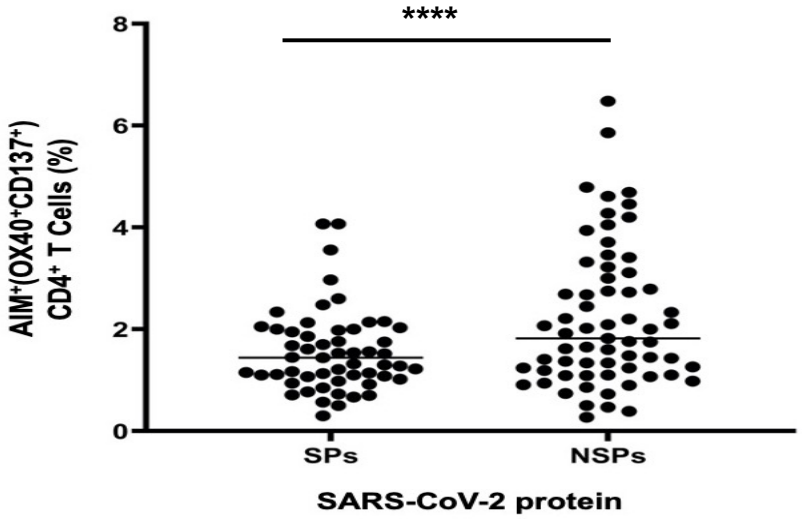

Fig. 23: AIM$^+$CD4$^+$ T-cell population in healthy donors activated by SARS-CoV-2 SPs and NSPs

Fresh PBMCs from the blood samples of heathy donors were isolated using Ficoll-Paque PLUS, and stimualted with the SPs or NSPs of SARS-CoV-2 for 6-days. The CD4$^+$ T-cells in healthy donors show significantly stronger response to NSPs than SPs. The statistics were evaluated by two-tailed Student t-test (paired) **** P <0.0001.

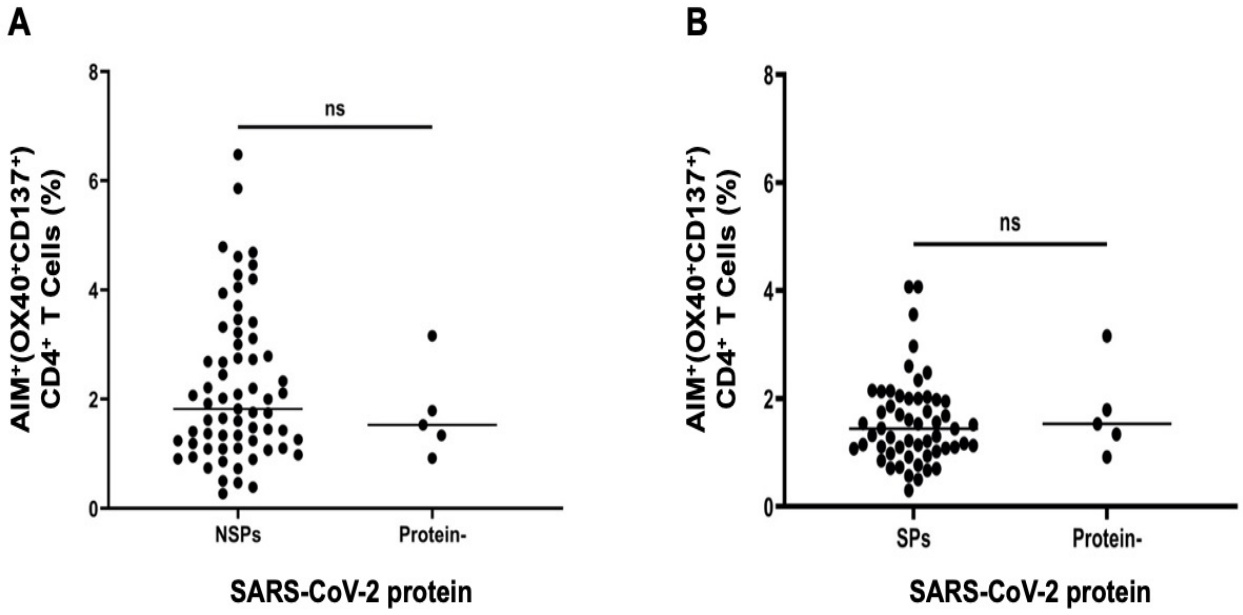

Fig. 24: The population of AIM$^+$CD4$^+$ T-cells stimulated with NSPs or SPs

Fresh PBMCs from the blood samples of heathy donors were isolated using Ficoll-Paque PLUS, and stimualted with the NSPs or SPs of SARS-CoV-2 for 6 days. No significant difference was seen in either condition. The statistics were evaluated by two tailed Student T test (paired). *p* value*<0.05.

Discussion

Previous reports used to investigate the $CD4^+$ T-cells immune response using HLA class I and II predicted peptide (megapools). Our study shows that we could detect SARS-CoV-2 $CD4^+$ T-cells immune response using synthesized and purified His-tagged SARS-CoV-2 recombinant proteins with Dynabeads. Moreover, the previous researchers focus mainly on immune responses to SPs, especially spike proteins. (Braun et al., 2020).

Interestingly, COVID-19 survivors and non-infected individuals have memory T-cells that exhibit cross-reactivity between SARS-CoV-1, SARS-CoV-2, and HCoV (Grifoni et al., 2020; Mateus et al., 2020). Overlapping peptides derived from the SARS-CoV-2 protein have been used to analyze overall T-cell responses to SARS-CoV-2, using IFN-γ ELISpot, and increased expression of activation markers as indicators. These analyses have revealed that T-cell responses to SARS-CoV-2 correlate with severity (Peng et al., 2022; Rydyznski Moderbacher et al., 2020). It was also revealed that COVID-19-uninfected individuals also responded to overlapping peptides derived from the SARS-CoV-2 protein, suggesting the existence of cross-reactive memory T cells (Grifoni et al., 2020).

Here we want to evaluate the preexisting memory $CD4^+$ T-cells not only to spike proteins but also for NSPs. One report has proved that non-spike-specific AIM^+CD4^+ T-cell responses were above the limit of detection in 50% of healthy donors Using sing HLA class I and II predicted peptide (megapools)(Grifoni et al., 2020). We here by using SARS-CoV-2 His-tagged proteins specified AIM^+CD4^+ T-cell responses to NSPs, which have been recognized among the healthy donors and strongly significantly increased in comparison to SPs. We could suggest the reason behind that increase due to amino acid sequence alignment, which revealed discrete areas of high homology in almost all SARS-CoV-2 proteins to the corresponding proteins in HCoVs. Highest degree of homology displayed by NSPs, such as NSP8, NSP10, and NSP12-16 (Loyal et al., 2021).While the overall homology of the amino acid sequences of the S protein is relatively low compared with spike glycoproteins from HCoV (Braun et al., 2020).

The SPs are under strong immune pressure from vaccination-induced antibodies, which can lead to vaccine-resistant mutant strains. On the other hand, the proteins targeted by cross-reactive T cells have few mutations (Young et al., 2020). Hence, they can maintain high efficacy against various mutant strains including latest Omicron variants. Further research is required to assess the role of cross-reactive T cell in SARS-CoV-2 unexperienced individuals in the context of COVID-19 pathogenesis.

We have found that NSPs $AIM^{+}CD4^{+}$ T cell responses non-significantly increased comparing to protein- $AIM^{+}CD4^{+}$ T cell responses which may be because of limited number of healthy donors.

We do suggest further studies for NSPs evaluation using large number of healthy donors and comparing them with COVID-19 patients which might help for developing effective COVID-19 vaccine in the future and could explain aspects of differential COVID-19 clinical outcomes, influence epidemiological models of herd immunity.

.

Chapter #2

Gold-nanocluster-mediated microinflammation detection using a tissue clearing method

1. Introduction

1-1. Multiple sclerosis (MS)

Multiple sclerosis (MS), an inflammatory T cell-mediated autoimmune disease with highly variable clinical manifestations, is the most common chronic inflammatory, demyelinating, and neurodegenerative disease of the central nervous system (CNS) in young adults. MS is influenced by both genetic and environmental factors, causes the demyelination of nerve cells, and destroys oligodendrocytes, neurons, and axons (Frohman et al., 2006; Lassmann et al., 2007). Such clinical manifestations of MS often include hyperreflexia, ataxia, spasticity, and visual defects (Frohman et al., 2006; Hafler et al., 2005; Keegan and Noseworthy, 2002; McFarland and Martin, 2007; Noseworthy et al., 2000), and in some cases there are sensory defects and partial or complete paralysis.

In the majority of patients, reversible episodes of neurological dysfunction lasting several days or weeks manifest as relapsing-remitting cycles of disease, and convert from the onset to a chronic progressive stage in 10–15% of patients in disease course (Frohman et al., 2006; McFarland and Martin, 2007; Sospedra and Martin, 2005; Steinman, 2009), resulting in irreversible clinical and cognitive deficits development over time. The pathological hallmark of MS is the formation of demyelinating lesions in the brain and spinal cord, which can be associated with neuro-axonal damage. Focal lesions are thought to be primarily caused by an inflammation triggered by infiltration of immune cells including T cells, B cells and myeloid cells, into the CNS parenchyma. The specific elements that start the CNS inflammation are largely unclear. Studies have suggested that genetic, environmental and infectious agents may be among the factors influencing the development of MS.

Since myelin-related protein, in particular, myelin basic protein (MBP) is a potential autoantigen in MS (Allegretta et al., 1990; Chou et al., 1992; Zhang et al., 1994), the role of T-cells in the

pathogenesis of MS have been considerably interested in development of immune responses to MBP (Jingwu et al., 1992). In fact, $CD3^+$ T cells have been demonstrated in all four of histopathologic subtypes of MS, although type III and IV lesions are additionally characterized by prominent oligodendrocyte degeneration (Lucchinetti et al., 2000), and characterize MS lesions by their perivascular infiltrates with macrophages (Prineas and Wright, 1978; Traugott et al., 1983). In addition, $CD4^+$ T cells are shown to predominately present in acute lesions, whereas $CD8^+$ T cells present more frequently in chronic lesions (Raine, 1994). Activated myelin-specific $CD4^+$ T cells are present in both blood and cerebrospinal fluid (CSF) of MS patients (Zhang et al., 1994), thus succeeding T-cell-targeted therapies in MS.

A MS-associated major histocompatibility complex class II (MHCII) allele, designated as DRB1*1501, effectively presents MBP-derived peptide antigen to T-cell clones isolated from MS patients (Wucherpfennig et al., 1997; Wucherpfennig et al., 1995), suggesting that MHCII genotype may play a role in VDJ rearrangements in MS lesions (Oksenberg et al., 1993). MBP-reactive T cells isolated from the CSF of MS patients display increased expression of IL-2 receptor (Zhang et al., 1994) and can be activated in the absence of CD28-B7 costimulation, consistent with a previously activated or memory phenotype (Markovic-Plese et al., 2001) . T cells in parenchymal MS lesions lacked CCR7, indicating a differentiation of central-memory T cells into effector memory cells presumably on restimulation by antigen within the CNS (Kivisakk et al., 2004). Furthermore, $CD4^+$ T-cell responses to another myelin-related protein, proteolipid protein (PLP), showed T-cell proliferation upon recognition of certain epitopes (Markovic-Plese et al., 2001; Pelfrey et al., 1994; Zhang et al., 1994). Moreover, CD4+ T-cell responses to myelin oligodendrocyte protein (MOG) increase reactivity (Kerlero de Rosbo et al., 1993) or altered T-cell properties (Van der Aa et al., 2003) in MS patients. Thus, many studies currently employ strategies to expand T cells using nonspecific methods or mixtures of myelin peptides.

Thus, multiple studies have demonstrated the presence of $CD4^+$ T cells in MS lesions, arguing for a central role in MS pathogenesis. The lack of consensus regarding T-cell specificities suggest a

heterogeneity in T-cell responses at the time of analysis, which may be a result of epitope spreading in chronic disease.

1-2. Experimental autoimmune encephalomyelitis (EAE)

Experimental autoimmune encephalomyelitis (EAE) is a $CD4^+$ T cell-mediated inflammatory demyelinating disease of the CNS. Although no animal model recapitulates all the underlying mechanisms of a complex human disease, much of the current understandings of pathological mechanism of MS have been obtained from EAE, since this model reproduces many clinical and immunologic features of MS, and has been widely used to study the mechanism of $CD4^+$ T-cell responses to myelin-related antigens (Bettelli et al., 1998; Chitnis et al., 2001), as well as to test potential therapies for MS (Aharoni et al., 1999; Yednock et al., 1992).

EAE can be induced via immunization with myelin-related protein or peptide antigen (aEAE). Initially, animals were actively immunized myelin components or CNS homogenates as self-antigen emulsified in adjuvant (Adelmann et al., 1995; Amor et al., 1994; Amor et al., 1996; Mendel et al., 1995; Tuohy et al., 1992; Wekerle et al., 1994; Zamvil et al., 1986). Later on, EAE was also passively induced by adoptive transfer of encephalitogenic T cells from aEAE mice (pEAE) (Kuchroo et al., 1992; Mendel et al., 1995; Pollinger et al., 2009; Stefferl et al., 2000; Zamvil et al., 1986). The aEAE is the easiest model for studying the mechanism of effector phase of disease utilizing gene-targeted recipient animal strains, and for providing the screening outcomes of the effects of drug candidates for autoimmune diseases (Batoulis et al., 2011; Kipp et al., 2012). By development of transgenic mice which bear MOG-specific TCR on T cells (Bettelli et al., 2003), C57BL/6 mice currently become more popular than Lewis rats, the most popular animal years ago due to reach 100% EAE incidence upon immunization of MBP (Bettelli et al., 2003). On the other hand, pEAE model is also useful to study the mechanism of stepwise development of CNS inflammation by donor $CD4^+$ T cells and following their localization, survival or interactions with other cell types in the recipient, and to also examine specific cytokines and other factors that affect pathology, avoiding simultaneous systemic effects of immunization as in aEAE.

It has been widely accepted that IFN-γ-producing Th1 cells are responsible for pathogenesis of MS and EAE, while Th2 cells are thought to be protective (Kuchroo et al., 2002). However, unexpectedly, mice lacking components of Th1-skewed factors such as IL-12α (IL-12p35) and IL-12Rβ2, or IFN-γ were more susceptible to EAE, while IL-12p40-deficient mice were resistant to disease (Ferber et al., 1996; Gran et al., 2002; Zhang et al., 2003). The series of discoveries of IL-23, which has the IL-12p40 subunit in common with IL-12, and IL-17-producing $CD4^+$ T cells (Th17) could explain this dichotomy. Mice deficient in IL-23 showed a defect of Th17 development, leading to a complete resistance to EAE (Ferber et al., 1996; Gran et al., 2002; Zhang et al., 2003). In contrast, myelin-specific $CD4^+$ T cells treated with IL-23 were more encephalitogenic than those treated with IL-12 (Cua et al., 2003; Langrish et al., 2004), suggesting that IL-23, but not IL-12, is critical in EAE pathogenesis.

1-3. Gateway reflex

Gateway reflex is a local neural regulation mechanism occurred during autoimmune responses, which involves changes in the status of regional blood vessels to create a vascular immune cell-gateway for autoreactive T cells to infiltrate from the blood flow to target organs **(Fig. 1)** (Murakami et al., 2019; Stofkova and Murakami, 2019). All gateways would be established through secretion of neurotransmitters such as noradrenaline and ATP from sympathetic pathway, and promote IL-6 amplifier with concomitant activation of NF-κB and STAT3 together with IL-17, TNF-α, and IL-6 from activated T cells in non-immune cells such as endothelial cells. The resultant synergistic enhancement of NF-κB activity enhances the expression of NF-κB-target genes including inflammatory cytokines, chemokines, and growth factors (Arima et al., 2012; Arima et al., 2017; Atsumi et al., 2014). Thus, the IL-6 amplifier in the endothelial cells in a specific vascular region is an underlying molecular mechanism of the gateway reflex.

We have found six types of gateway reflex that are mediated by gravity, electric stimulation, pain, stress, light, or remote inflammation so far (Arima et al., 2012; Arima et al., 2015; Arima et al., 2017; Hasebe et al., 2022; Stofkova et al., 2019). Among them, the gravity gateway reflex is the first gateway reflex discovered (Arima et al., 2012). Using a passive transfer EAE model, we found that the gravity stimulation leads to local inflammation at specific blood vessels in the CNS. At the pathogenesis in the EAE disease course, autoreactive T cells, which are myelin-specific, first

accumulated at specific blood vessels of the fifth lumbar spinal cord (L5), triggered IL-6 amplifier, followed by an overexpression of chemokines at the blood vessels. The IL-6 amplifier then synergistically recruited T cells and caused pathological consequences. The dorsal root ganglia (DRG) at the L5 are a region where sensory neurons of the soleus muscle (anti-gravity muscle) connect. The L5 DRG is the largest of the DRG in both mice and humans, most likely because of its constant stimulation by gravity (Ohira et al., 2004; Shen et al., 2006). In fact, the tail suspension model (also known as hindlimb-unloading model), in which gravity–soleus–L5 pathway can be blocked by being the hindlegs free from gravity, revealed that accumulation of pathogenic T-cells is markedly reduced due to the decreased chemokine expression at the L5, ameliorating the disease (Ohira et al., 2004; Shen et al., 2006). Further investigation showed that norepinephrine-mediated NF-κB and STAT3 activation along with CCL20 expression in endothelial cells of the blood vessels enabled accumulation of autoreactive T cells, followed by the infiltration of various immune cells at the L5 (Arima et al., 2012). Besides sensory nerves in the L5 DRG, the anti-gravity responses selectively stimulated several neurons in sympathetic ganglia at the L5 level. The pharmacological blockade of adrenergic receptor significantly lowered the grade of CNS inflammation by reduction of chemokine expression at the specific vessels around the L5. Thus, the gravity gateway reflex exerts a pro-inflammatory effect via modulation of the L5 dorsal vessels by a sensory-sympathetic crosstalk, although the precise neural connections remain unidentified (Arima et al., 2012; Kamimura et al., 2020; Uchida et al., 2022).

The gravity gateway reflex can be recapitulated by weak electric stimulation of muscles of interest. Electric stimulation of the soleus muscles mimics the effect of gravity, and induces chemokine production at the L5 dorsal vessels, whereas stimulation of the quadriceps or triceps promotes chemokine expression at the dorsal vessels of L3 or lower cervical to upper thoracic spinal levels, respectively (Arima et al., 2012). The concept of the electric gateway reflex suggests that a simple device like an electric muscle stimulator could deliver cells or antibodies to the CNS. This possibility has significant implications for immune-based therapeutic strategies including chimeric antigen-receptor (CAR) T-cell therapy for brain tumors and for vaccination-mediated or antibody-mediated clearance strategies of neurotoxic substances like tau or β-amyloid in neurodegenerative diseases including Alzheimer's disease (Bagley et al., 2018; Braczynski et al., 2017).

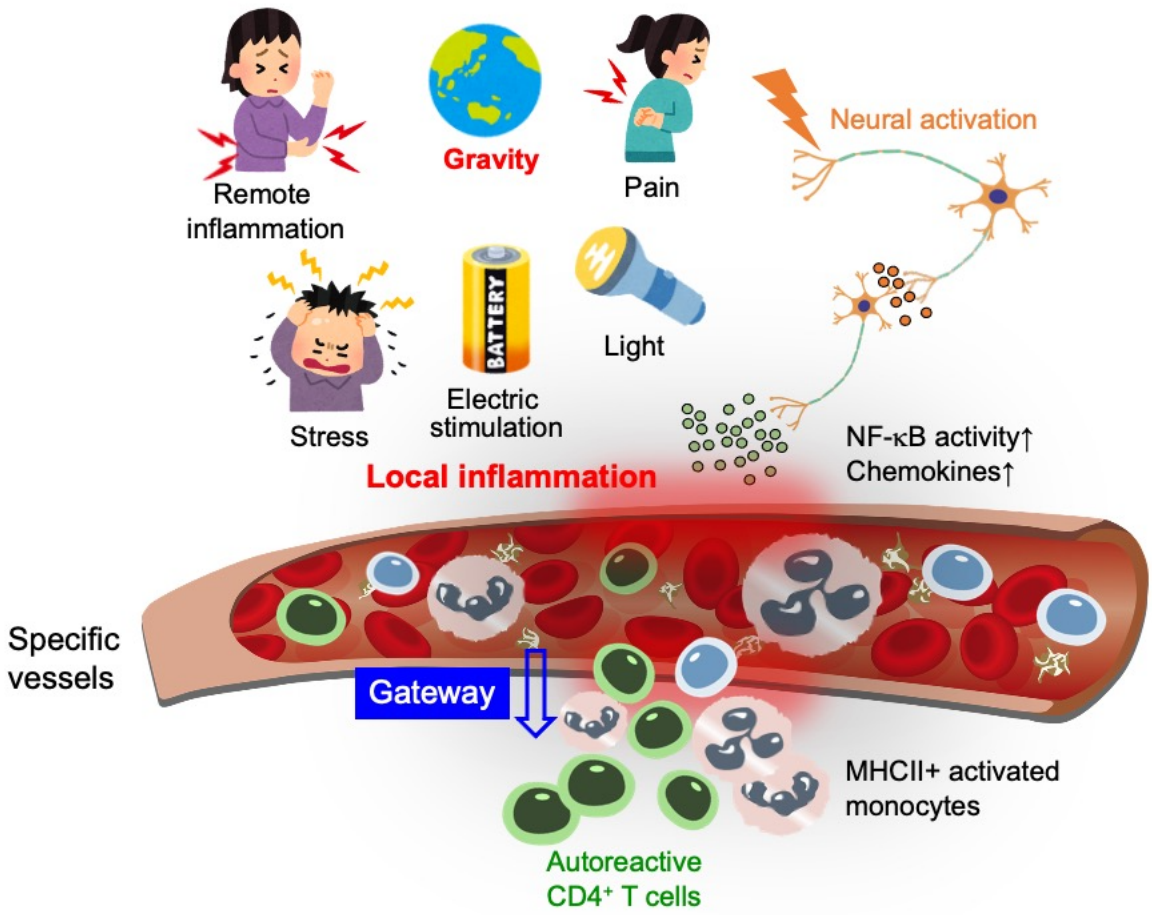

Fig.1: Gateway reflex

The activation of specific neural circuits by environmental stimuli as well as artificial electric stimulations on muscles results in the production of local neurotransmitters, such as noreadrenaline, and increases chemokine expression at specific blood vessels via IL-6 amplifier activation. When CNS-specific or retina-specific autoreactive CD4+ T cells are present in the blood, they accumulate at a specific blood vessel in the CNS or retina, respectively, to disrupt the blood barriers and induce inflammatory diseases. Six types of gateway reflexes triggered by gravity, pain, stress, light, electric stimulation, and remote inflammation have been reported.

1-4. Coordinated gold nanoclusters (AuNCs)

Coordinated gold nanoclusters (AuNCs) have been paid attention owing to the advantages of atomically precise molecular structure, ultrasmall size, facile surface modification, and characteristic optical property (Jin et al., 2016). Some of AuNCs have been reported to exhibit unique photoluminescence emission with long lifetime and large stoke shift in the broad region

ranging from visible to near-infrared (Jin et al., 2016), high compatibility, and photostability. Thus, they are good candidates of luminophores for long-term imaging, high-sensitivity detection, and target-specific treatment (Luo and Liu, 2022; Palmal and Jana, 2014; Zhang et al., 2022). Namely, AuNCs have brought significant impacts in the applications of imaging, detection, and therapy as fluorescent probes. Phosphine-coordinated AuNCs offer a representative luminescent gold cluster family (Konishi et al., 2018; Sugiuchi et al., 2017). Among them, Au_{13} clusters with an icosahedral gold core motif are interesting, because of easy accessibility, robustness, and moderately intense photoluminescence in near-infrared region (Shichibu and Konishi, 2010; Sugiuchi et al., 2015).

1-5. CUBIC tissue-clearing method

Histologically, the standard procedure to investigate tissues, were to perform immunohistochemistry to obtain 2D-image of the selected parts of tissue. However, a complete understanding of biological mechanisms in health and disease requires an unbiased exploration of the whole organism.

State-of-the-art tissue-clearing methods which provide three-dimensional (3D) imaging of intact tissues and even some entire organs at a subcellular level, has become a recent trend on the development of tissue-clearing reagents and protocols, efficient fluorescent labelling, and rapid volumetric imaging by light-sheet microscopy (Hama et al., 2015; Ueda et al., 2020). By combining the powerful labelling, clearing, imaging, and data-analysis tools, the structural and functional cellular and subcellular information can be obtained from complex mammalian bodies and large human specimens at an accelerated pace. Despite such tissue-clearing approach enabling high tissue-transparency within a few days using organic chemicals (e.g., benzy alcohol–methyl salicylate, benzyl alcohol–benzyl benzoate (BABB), researchers concerned about quenching of fluorescent proteins and safety issues. However, Tainaka and Kubota et al., took a system-level approach to identifying potent hydrophilic (aqueous) tissue-clearing reagents by comprehensive chemical profiling, and developed a tissue-clearing method with series of clear, unobstructed brain or body imaging cocktails and computational analysis (CUBIC) reagents for both delipidation and decolorization, which usually form hydrogen bonds with proteins and surrounding water molecules, contributing to preserve the 3D structure of tissue components and fluorescent proteins conjugated to antibodies (**Fig. 2** (Tainaka et al., 2014)).

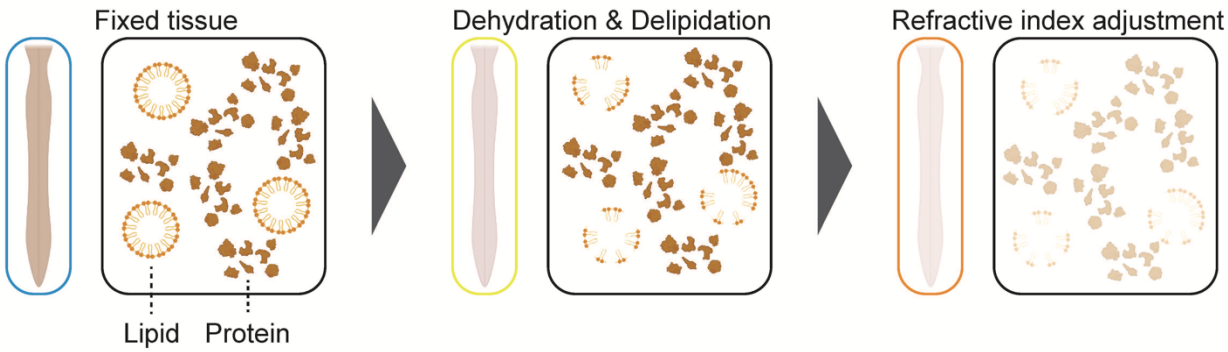

Fig. 2: Overview of tissue-clearing methods

(a) Organic solvent–based clearing methods include dehydration, delipidation, bleaching, and refractive index (RI) matching. Water-miscible polar solvents dehydrate tissue samples. Delipidation by THF or DCM contributes to clearing efficiency after RI matching. Although the water-free clearing method results in some tissue shrinkage and quenching of fluorescent proteins, these protocols are simple and fast and have high clearing performance. (b) Hydrophilic reagent–based clearing methods include delipidation, decolorizing, and RI matching. Detergents and aminoalcohols remove lipids from tissue samples. Delipidation is facilitated by chemically or physically induced molecular flux. Urea promotes the influx of aminoalcohol and detergent in the CUBIC protocol. Permeation of the ionic detergent SDS is driven by electric field potential (CLARITY), transcardial perfusion (PARS), or thermal energy (SWITCH). Highly water-soluble molecules such as sugars and contrast reagents are used as RI matching medium.

1-6. Hypothesis and Objectives

We hypothesized that using rapid 3D-imaging method may be useful method for detection of microinflammation at a vascular gate formed in the L5 of the CNS in mice induced EAE, by utilizing Au_{13} nanoclusters (Shichibu and Konishi, 2010) and hydrophilic CUBIC tissue-clearing method (Tainaka et al., 2014). Our method will be useful to specify the organ in various inflammatory diseases, where a stepwise development of microinflammation triggered by recruitment of pathogenic immune cells including $CD4^+$ T cells occurs, and will also provide future perspectives of Au_{13} nanocluster-based imaging technique for a complete understanding of biological mechanism of disease pathogenesis and practical biomedical applications.

2. Materials and Methods

2-1. Mouse strains

C57BL/6 mice were purchased from Japan SLC (Shizuoka, Japan). Adult (6–8 weeks of age) male mice were used in all experiments. Mice were maintained under specific pathogen-free conditions, according to the protocols of Hokkaido University Medical School. All animal experiments were performed following the guidelines of the Institutional Animal Care and Use Committees of the Institute for Genetic Medicine, Hokkaido University. The protocols for animal experiments were approved by the Institutional Animal Care and Use Committees of Hokkaido University.

2-2. Induction of active EAE and assessment of clinical scores

EAE was induced by immunization with 400 μg of $MOG_{35–55}$ peptide emulsified in complete Freund's adjuvant (Sigma-Aldrich) containing 200 μg of heat-killed *Mycobacterium tuberculosis* H37RA (DIFCO). The 200 μl of emulsion was subcutaneously (s.c.) injected to mice at the tail base (s.c.), and 200 ng of pertussis toxin (PTx) from *Bordetella pertussis* (Sigma-Aldrich) in 200 μl of PBS was intraperitoneally (i.p.) administered on the same day, on day 2 and day 7 after immunization. Clinical signs of EAE were assessed daily with a 0–5 scoring system (0, no signs; 1, flaccid tail; 2, impaired righting reflex and/or gait; 3, hind limb paralysis; 4, hind limb paralysis with partial fore limb paralysis; 5, moribund or dead).

2-3. Passive transfer EAE model

On day 10 after MOG/CFA immunization, the spleens of ten active EAE mice were collected, and homogenized on a cell strainer with plane RPMI medium flowing. After centrifugation at 600 x g for 5 min at 4 °C, the supernatant was discarded, and the cells were resuspended in 10 ml of RBC lysis buffer on ice for 1 min to remove red blood cells. The cells were then washed with plane RPMI medium, centrifuged, and resuspended in 1440 ul of MACS buffer (0.5% fetal bovine serum (FBS) and 2 mM EDTA in PBS) and 1440 ul of CD4 (L3T4) MicroBeads (Miltenyi Biotec) at 4 °C. After washing with 25 ml of MACS buffer, the cells were resuspended in 6 ml of MACS buffer, and divide into two 15 ml tubes (3ml/tube). And the cells were subjected to separation of $CD4^+$ T-cells on Depl05 separation program by autoMACS Pro Cell Separator. The purified $CD4^+$ T-cells (positive fraction) and $CD4^-$ cells containing antigen-presenting cells including B cells and

dendritic cells (negative fraction), were pooled and centrifuged. After discarding the supernatant, the cells in each fraction were further washed with 10% FBS-, 50 μM 2-ME-containing RPMI RP10 medium, twice, and resuspended with 1 ml (for $CD4^+$ T-cells) and 10 ml (for $CD4^-$ cells) of RP10 medium, respectively. The $CD4^+$ T cells and $CD4^-$ cells irradiated at 35 Gy were mixed at 6.25 x 10^6 cells/ml and 1.25 x 10^6 cells/ml in RP10 medium containing 75 ng/ml hIL-6, 7.5 ng/ml IL-1β, 7.5 ng/ml IL-23, and 6 μg/ml MOG_{35-55}, respectively, and seed 200 μl of the cell mixture per well of 96-well plate to reactivate $CD4^+$ T cells at 37 °C, 5% CO_2 for 24 hrs. And the cells were collected, centrifuged, and washed with 15 ml MACS buffer, twice. Then, the cells were resuspended in 1440 ul of MACS buffer (0.5% fetal bovine serum (FBS) and 2 mM EDTA in PBS) and 1440 ul of CD4 (L3T4) MicroBeads at 4 °C. After washing with 25 ml of MACS buffer, the cells were resuspended in 6 ml of MACS buffer, and divide into two 15 ml tubes (3ml/tube). And the $CD4^+$ T-cells were purified on Depl05 separation program by autoMACS Pro Cell Separator, and adjusted the cell density to 5 x 10^7/ml in saline after washing twice. Finally, 2 x 10^7 $CD4^+$ T-cells in 400 μl of saline were transferred i.v. to naïve B6 mouse, and the mice were measured clinical scores as described below, according to (Ogura et al., 2008; Arima et al., 2012; Arima et al., 2015a)

2-4. Preparation of Au_{13} nanoclusters

Au13 nanocluster was synthesized and isolated as crystalline solids, according to the following four procedures described in Shichibu and Konishi, 2010. (i) AuN:dppe preparation; 10 mL of $NaBH_4$ (66.2 mg, 1.75 mmol) ethanol solution was added to 240 mL of $Au_2(dppe)Cl_2$ (302 mg, 0.35 mmol) (Dichloromethane solution) and the mixture was stirred at room temperature for 3 hrs. After removal of the solvent, the residue was suspended in dichloromethane and filtered to remove insoluble materials. To give the mixture as a dark-brown solid (283.6 mg). The filtrate was evaporated to dryness. ESI-MS and transmission electron microscopy (TEM) analysis indicated that mixture was composed of ultrasmall gold clusters. The wt% of gold was estimated at 56% based on thermogravimetric analysis. (ii) $Au_{13}(dppe)_5Cl_2]$ Cl_3 preparation; AuN: dppe (283.6 mg) in ethanol (49 mL) was mixed with 12 M HCl (1 mL, 12 mmol) and the mixture was stirred at room temperature. The volatiles were evaporated After 24 h, and the residue was washed with acetone, suspended in methanol, and then filtered. The filtrate was evaporated to dryness to give (Au_{13} $(dppe)_5CI_2$) CI_3 as a red solid (75.9 mg; 30% based on the initial amount of $Au_2(dppe)Cl_2$).

Elemental analysis: Calcd (%) for $C_{130}H_{120}Au_{13}Cl_5P_{10}$: C 33.01, H 2.56, Cl 3.75; found: C 33.13, H2.64, Cl 3.57; no nitrogen was found. (iii) $Au_{13}(dppe)_5Cl_2](PF_6)_3$ preparation; 2.3 mg, 0.49 mmol of $[Au_{13}(dppe)_5Cl_2]Cl_3$ and $NaPF_6$ (excess) were mixed in ethanol and the resulting reddish precipitate was collected by filtration. Red needle-shaped crystals of $[Au_{13}(dppe)_5Cl_2](PF_6)_3$ suitable for X-ray analysis were grown from ethanol/ dichloromethane (1:1). ESI-MS spectra were recorded on a Bruker micrOTOF-HS and optical absorption spectra were recorded using a JASCO V-670 double-beam spectrometer. Photoluminescence and excitation spectra were recorded on a HORIBA Jobin Yvon SPEX Fluorolog-3 spectrofluorometer equipped with a Hamamatsu Photonics R928 photomultiplier tube detector. 31P NMR spectra were collected at ambient temperature on a JEOL EX-400 NMR spectrometer. Chemical shifts (in ppm) were referenced to 85% H_3PO_4 (external standard). Crystalline solids of the Au_{13} nanoclusters were weighed (~3 mg), and were dissolved in dimethyl sulfoxide (final concentration: 160 µM).

2-5. Preparation of the lumbar cords from Au_{13} nanoclusters-treated EAE mice

Au_{13} nanocluster solution (160 µM) was diluted to 32 µM with saline, and 200 µl of the dilutant was injected i.v. to aEAE mice with score 2-3, using 27 G x 1/2 needle. After 2 hrs, the mice are anesthetized with isoflurane, and perfused with 25 ml of cold PBS, followed by 20 ml cold 4% paraformaldehyde (PFA; Nacalai Tesque). Then, the spine was taken out and post-fixed in 40 ml of 4% (w/v) PFA in a 50 ml tube at 4 °C for 24 hrs with shaking on TAITEC Shake-LR (reciprocating type, speed 60). And the spine was washed with 40 ml of PBS at room temperature (RT) for 0.5 hr three times with shaking on TAITEC Wave-SI (reciprocating type, speed 30), and the 1st to 6th lumbar spinal cords (L1-L6) were carefully excised under stereomicroscope system OLYMPUS SZ61.

2-6. Tissue-clearing

An overview of tissue-clearing method used in the study is shown in **Fig. 3**.

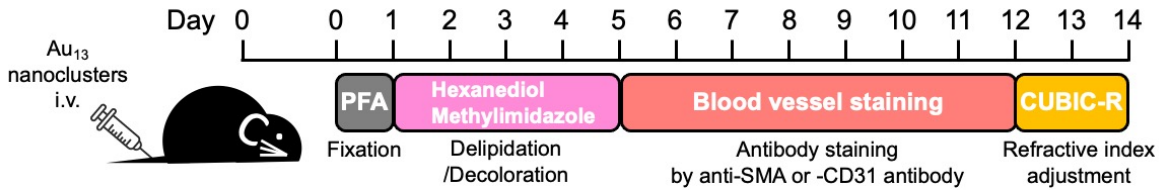

Fig. 3: Overview of procedures for detecting microinflammation using Au_{13} nanoclusters and CUBIC tissue-clearing method

Mice were injected with Au_{13} nanoclusters intravenously (i.v.), anesthetized after 2hrs, and transcardially perfused with PBS, followed by 4% PFA. After excising the spine, it was further subjected to PFA fixation for 1-day. Next, the lumbar cords were taken out carefully, and immersed in delipidation reagent (hexanediol/methylimidazole) for 4-days with shaking. After the delipidation and decoloration, the lumbar cords were stained with anti-SMA or -CD31 for 7-days with shaking, and subjected to postfixation in 1% PFA, followed by adjustment of refractive index in CUBIC-R reagent.

For the preparation of tissue-clearing samples, the post-fixed lumbar cords were immersed in delipidation/decoloration buffer (10% (w/w) 1,2-Hexanediol and 2% (w/w) 1-Methylimidazole (Tokyo Chemical Industry) in PBS) in a 15 ml tube at 37°C for 4 days with shaking at 80 rpm horizontally on AS ONE Neo Shaker, and then washed with 10 ml of PBS at RT for 1 hr three times on TAITEC Wave-SI (reciprocating type, speed 30). For antibody staining, the samples were immersed in 1.5 ml of antibody solution of FITC-conjugated mouse monoclonal α-smooth muscle (SMA) antibody (clone: 1A4, Sigma-Aldrich) or purified rat anti-mouse CD31 (clone: MEC 13.3, BD Biosciences) diluted at 1:50 with staining buffer (0.5% Triton X-100 (Sigma-Aldrich), 0.01% sodium azide (FUJIFILM Wako), 0.5% casein (Sigma-Aldrich) in PBS) at RT for 7 days with shaking at 100 rpm horizontally on TAITEC Double Shaker NR-3. After that, the samples were washed with 10 ml of PBS in a 15 ml tube at RT for 0.5 hr three times with shaking on TAITEC Wave-SI (reciprocating type, speed 30). For anti-CD31 staining, the samples were further immersed in 1.5 ml of Alexa Fluor 555-conjugated goat anti-rat IgG Goat anti-Rat IgG (H+L) cross-absorbed secondary antibody (Thermo Fisher Scientific) diluted at 1:200 with staining buffer at RT for 2-days, and then washed with 10 ml of PBS in a 15 ml tube at RT for 0.5 hr three times on TAITEC Wave-SI (reciprocating type, speed 30). Following the antibody staining steps, the samples were postfixed with 10 ml of 1% PFA in PBS at RT for 5 hrs on TAITEC Wave-SI (reciprocating type, speed 30), and washed with 10 ml of PBS at RT for 0.5 hr three times on TAITEC Wave-SI (reciprocating type, speed 30). For refractive index adjustment, the samples were immersed in 10 ml of 1/2 CUBIC-R (45% (w/w) 2,3-Dimethyl-1-phenyl-5-pyrazolone and 30% (w/w) nicotinamide (Tokyo Chemical Industry)) at RT for 5 hrs with shaking at 100 rpm

horizontally on TAITEC Double Shaker NR-3. After discarding 1/2 CUBIC-R, the samples were further immersed in 10 ml of CUBIC-R at RT overnight with shaking at 100 rpm horizontally on TAITEC Double Shaker NR-3, replaced with fresh CUBIC-R, and further immersed at RT for 12 hrs with shaking. In all steps following antibody staining, the samples were covered with aluminum foil for full light shielding. The cleared lumbar cords were subsequently subjected to an imaging analysis of the L5.

2-7. Microscopy

The 3D lumbar cord images were acquired with light-sheet fluorescence microscopy (LSFM) (UltraMicroscope II-Light sheet microscopy, LaVision BioTec, Germany) as reported previously (Dodt et al., 2007; Susaki et al., 2014) with a custom-build LSFM (developed by Olympus, Tokyo, Images were captured at 0.63 × objective lens (numerical aperture = 0.15, working distance = 87 mm) with digital zoom from 1 × to 6.3 × zoom. Lasers of 488 nm, 532 nm, 590 nm, and 639 nm were used for image acquisition. To cover the L1-L6, the stage was moved both in the lateral direction and axial direction. When the stage was moved to the axial direction, the detection objective lens was synchronically moved to the axial direction to avoid defocusing. High resolution images for cell profiling were acquired with CLSM (FLUOVIEW FV1200, Olympus). Images were captured at 25 × objective lens (numerical aperture = 1.0, working distance = 8.0 mm) with digital zoom from 1 × to 2 × zoom. Lasers of 473 nm, 559 nm, and 635 nm were used for image acquisition. RI matched sample was immersed in a mixture of silicon oil HIVAC-F4 (RI = 1.555, Shin-Etsu Chemical Co., Ltd., Tokyo, Japan) and mineral oil (RI = 1.467, M8410, Sigma-Aldrich) during image acquisition. All raw image data were collected in a lossless 16-bit TIFF format. 3D-rendered images were visualized, captured, and analyzed with Imaris software (version 9.0.0, Bitplane AG, Zurich, Switzerland).

2-8. Image data processing and analysis

All raw image data were collected in a loss less 16-bit TIFF format. 3D-rendered images were visualized, captured, and analyzed with Imaris software (version 9.0.0, Bitplane AG, Zurich, Switzerland). Brightness, contrast, and gamma of the 3D-rendered images were manually adjusted with the software at minimum when visualized. The 3D images were then used for image analysis with Imaris software. Noise signals were obtained via excitation at 555nm in alexa488 channel were manually excluded with the software at minimum when visualized.

3. Results

3-1. Microinflammation was detected at the dorsal vessel of the L5 in aEAE mice by Au_{13} nanoclusters

We previously showed by immunohistochemistry on sections, that during the development of EAE pathogenesis in pEAE model, pathogenic $CD4^+$ T cells in the blood, which recognize myelin-derived antigens, accumulate at the dorsal vessels of the L5, followed by development of CNS inflammation, in a mechanism of IL-6 amplifier following gateway reflex triggered by gravity **(Arima et al., 2012)**.

To create a new method to identify the site of microinflammation, which triggers an onset of chronic inflammatory diseases, we first applied an ultrasmall coordinated Au_{13} nanoclusters with high photostability, compatibility and sensitivity, as an inflammation probe (tracer) and CUBIC tissue-clearing method to EAE model.

Mice were induced by immunization of MOG/CFA with PTx administration (**Fig. 4**; aEAE), and injected a luminescent Au_{13} nanoclusters, when they showed impaired righting reflex and/or gait, or paralysis of hind limbs, that is assessed as clinical score 2 or 3. Two-hours later, the spine was excised and subjected to tissue-clearing protocol with an antibody specific for smooth muscle enables to detect artery (SMA) **(Fig. 5)**. As a result, the Au_{13} nanoclusters were preferentially leaked at the dorsal vessels (stained with anti-SMA antibody) of the L5 in aEAE mice **(Fig. 6A left and 6B left)**, whereas they were only detected within the blood flow in naïve mice **(Fig. 6A middle and 6B right)** with a sharp contrast to no Au_{13} signal in aEAE mice injected the solvent as a negative control **(Fig. 6A right)**. Furthermore, tissue-clearing was also performed with anti-CD31 antibody to detect endothelial cells of blood vessels (CD31). Similar to **Fig. 6**, Au_{13} nanoclusters were also preferentially detected extravascularly at the L5 of aEAE mice **(Fig.7)**.

3-2. Microinflammation was also detected at the L5 in pEAE mice by Au_{13} nanoclusters

The pEAE model established by transfer of MOG-specific $CD4^+$ T cells, are suitable to track autoreactive $CD4^+$ T cells *in vivo*. The clinical signs usually appear from day 5 after adoptive transfer of $CD4^+$ T cells, peak on around day 10-14 with score more than 3, and then will decline **(Arima et al., 2015).** In this remission phase, the mice look healthy. However, activated monocytes remain in the spinal cords, and paralysis returns upon specific neural activation including pain sensation.

To further examine whether the Au_{13} nanoclusters-based microinflammation detection method can also apply for pEAE model, the $CD4^+$ T cells were purified from mice with aEAE on day 10, and transferred to naïve C57BL/6 mice after reactivation with $CD4^-$ cells as APCs in the presence of MOG_{35-55} and cytokines. The lumbar spinal cords of pEAE mice with score 2-3 excised were first subjected to tissue-clearing protocol with 200 µl of injection with 3.2 µM Au_{13} nanoclusters and staining SMA using Cy3- and Alexa-Fluor 594-conjugated specific antibodies. In this condition, the co-location of Au_{13} nanoclusters and SMA out of blood vessels around the L5 of pEAE mice was hardly detected **(Fig. 8)**. However, when a 10-fold higher amount of Au_{13} nanoclusters corresponding to the amount used in aEAE was injected **(Fig. 6 and 7)**, the Au_{13} nanoclusters were also preferentially detected at the L5 of pEAE mice, although unspecific signals were observed in both pEAE and naïve mice without transferring $CD4^+$ T cells **(Fig.9)**.

Taken together, these data suggest that microinflammation predominantly occurs at the dorsal vessel of the L5 during EAE course, which could support our previous findings in pEAE model, that this site is primary for a vascular gate formation, that facilitates pathogenic immune cells including myelin-specific $CD4^+$ T-cells to leak out of blood vessels and enter the CNS, through an initiation of IL-6 amplifier.

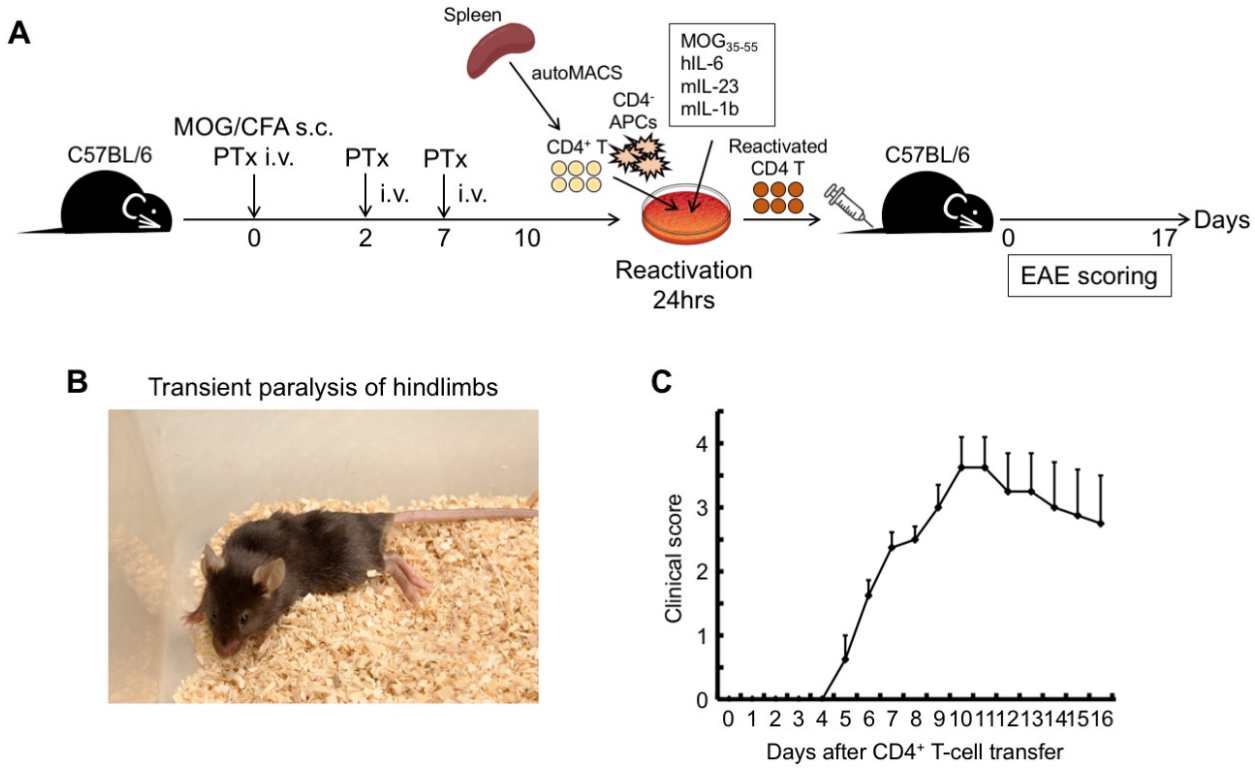

Fig. 4: aEAE and pEAE models

A. C57BL/6 mice were immunized s.c. with $MOG_{35–55}$ peptide emulsified in CFA, containing heat-killed *Mycobacterium tuberculosis* H37RA at the tail base, and administered i.v. PTx on the same day, on day 2 and day 7 after immunization (aEAE). On day 10, aEAE mice were sacrificed, and the spleens were homogenized to separate $CD4^+$ T cells and $CD4^-$ cells as antigen-presenting cells by autoMACS Pro Separator. The $CD4^+$ T cells were then reactivated by culturing with irradiated $CD4^-$ cells in RP10 medium containing hIL-6, mIL-23, and IL-1β for 24 hrs. After the reactivation, the $CD4^+$ T cells were also purified by autoMACS Pro Cell Separator, and transferred to naïve B6 mice (pEAE). **B.** pEAE mice with transient paralysis of hindlimbs (clinical score 3). **C.** Clinical scores during EAE course after transfer of encephalitogenic $CD4^+$ T cell fraction from aEAE mice.

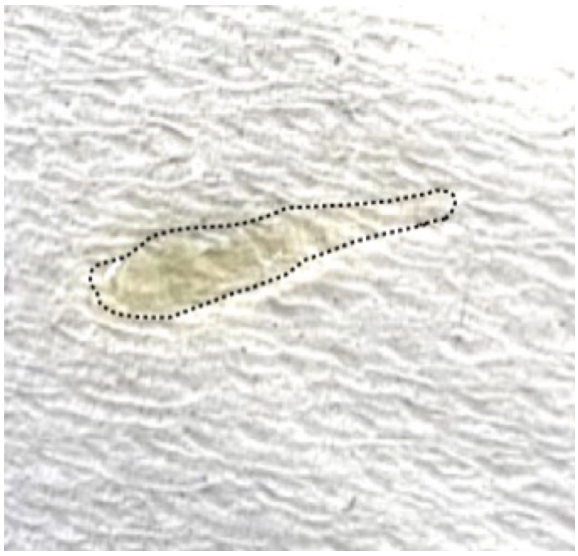

Fig. 5: Cleared lumbar cords

Bright-field image of the lumbar cords after CUBIC-R treatment overnight at RT with shaking is shown. Dashed line indicates the outline of L1-L6, (From left to right).

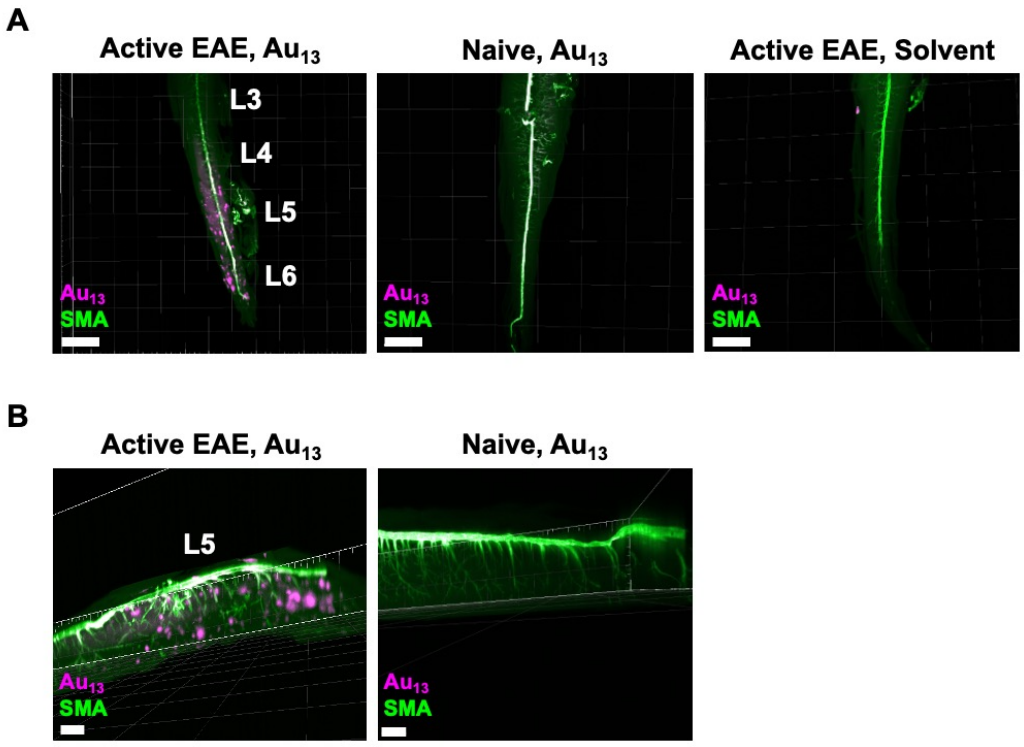

Fig. 6: Detection of microinflammation at the L5 in aEAE mice, by CUBIC tissue-clearing method with Au_{13} nanoclusters and anti-SMA antibody

(A) aEAE with score 2-3 and naïve mice were intravenously injected with 200 µl of 32 µM of Au_{13} nanoclusters Au_{13} nanoclusters or solvent. Figures show the L3-L6 from each mouse. The signal of Au_{13} nanoclusters was recognized as a punctate signal with a diameter of 50-200 nm in the dorsal blood vessels centered on the L5 and in the parenchyma of the spinal cords. Intravascular signals were also observed, when naive mouse was injected with Au_{13} nanoclusters. Bar indicates 1,500 µm. magenta: Au_{13} nanocluster, green: SMA (artery).

(B) Magnified image of the L5 from aEAE mouse stained with Au_{13} nanoclusters and anti-SMA. Bar indicates 1,000 µm. magenta: Au_{13} nanocluster, green: SMA (artery).

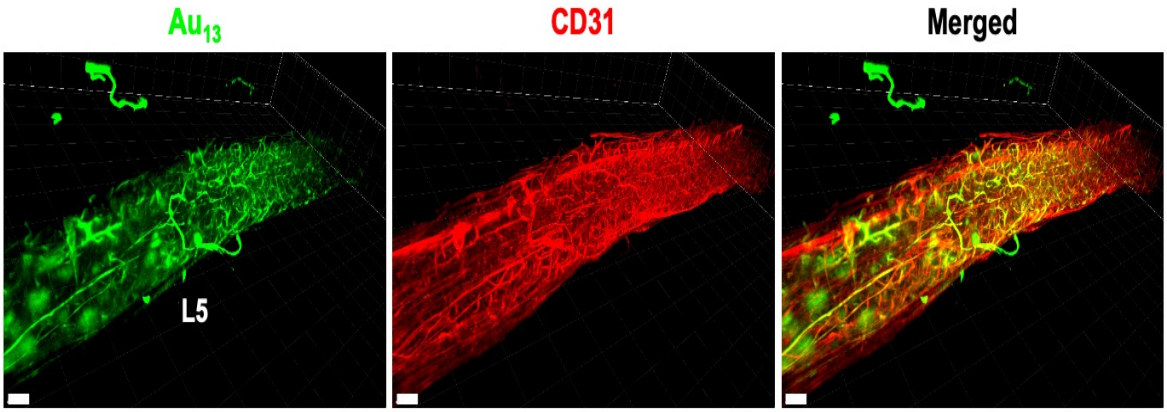

Fig.7: Detection of microinflammation at the L5 in aEAE mice, by CUBIC tissue-clearing method with Au_{13} nanoclusters and anti-CD31 antibody

aEAE mouse with score 2-3 was intravenously injected with 200 µl of 32 µM of Au_{13} nanoclusters. Figures show the L5. Bar indicates 400 µm. green: Au_{13} nanocluster, red: CD31 (blood vessel).

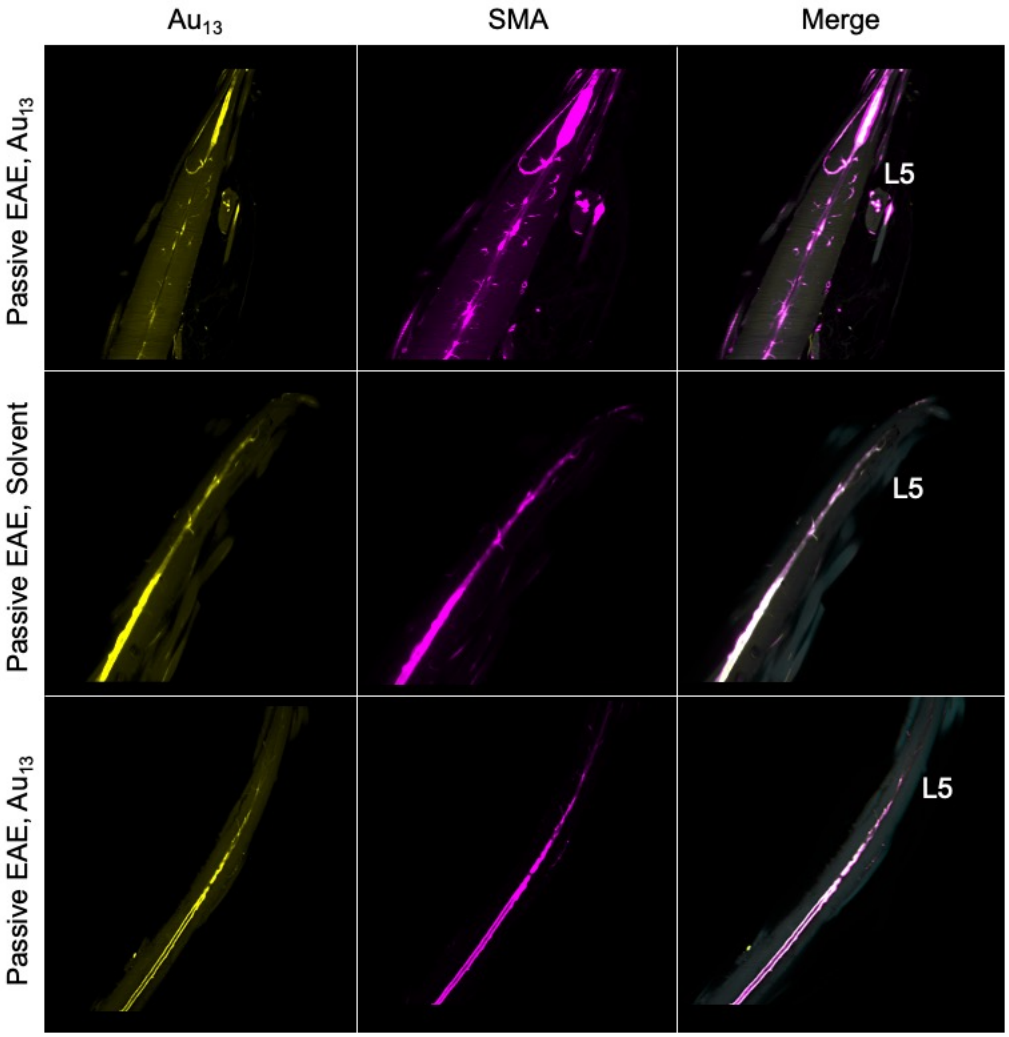

Fig. 8: Attempt of microinflammation detection at the L5 in pEAE mice, by CUBIC tissue-clearing method with Au_{13} nanoclusters

pEAE with score 2-3 were intravenously injected with 200 µl of 3.2 µM Au_{13} nanoclusters or solvent. Upper and middle panels, and lower panel show the co-location of Au_{13} nanoclusters and SMA at the L1-6 from each mouse, when Cy3- and Alexa-Fluor 594-conjugated anti-SMA antibodies were used, respectively. With the amount of Au_{13} nanoclusters used, the signal of Au_{13} nanoclusters around the blood vessels at the L5 of aEAE mouse was hardly detected. Bar indicates 1,000 µm. yellow: Au_{13} nanocluster, magenta: SMA

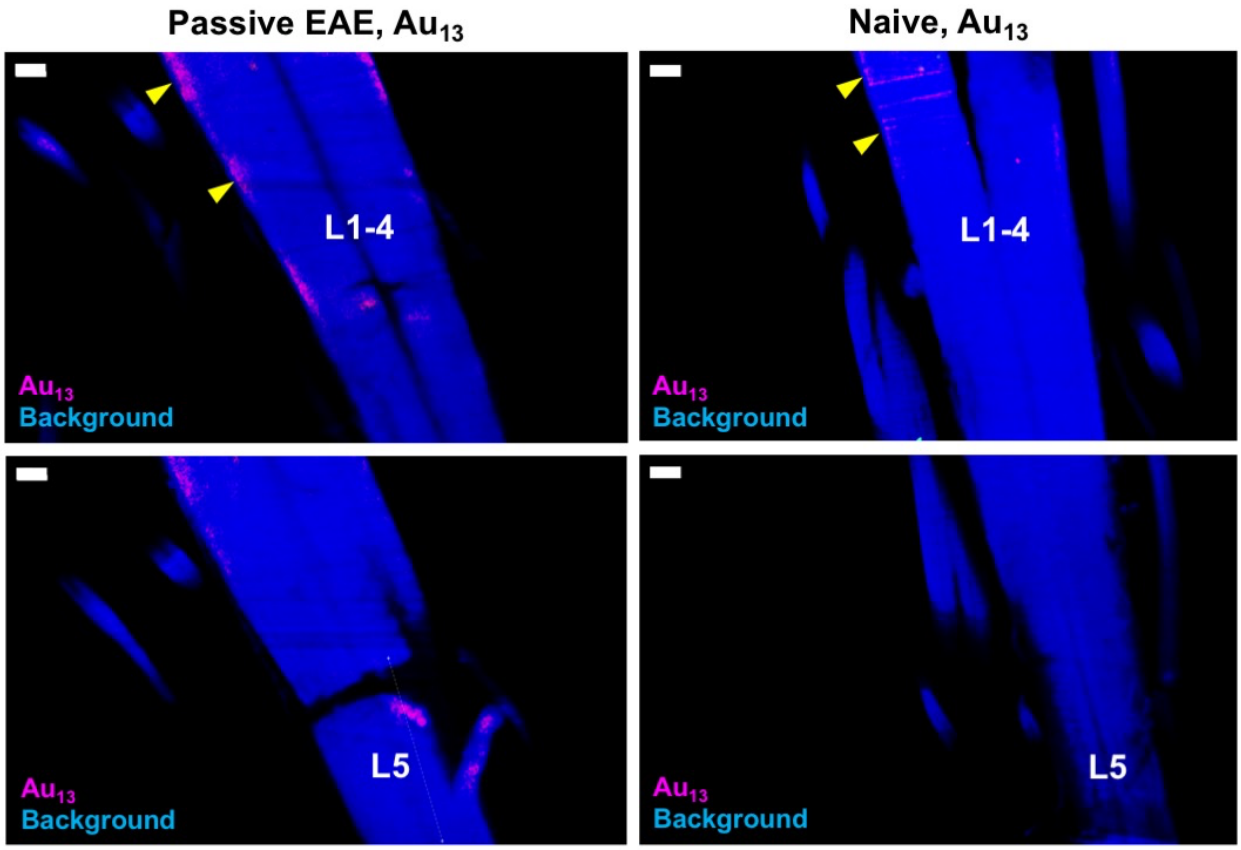

Fig. 9: Detection of microinflammation at the L5 in pEAE mice, by CUBIC tissue-clearing method with Au_{13} nanoclusters

pEAE with score 2-3 and naïve mice were intravenously injected 200 µl of 32 µM Au_{13} nanoclusters. The upper and lower panels show the L1-4 and the L5 from each mouse, respectively. The signal of Au_{13} nanoclusters was detected in the L5 of aEAE mouse, but not that of naïve mouse. Yellow arrowheads in the L1-4 indicate unspecific signals of Au_{13} nanoclusters. Bar indicates 100 µm. magenta: Au_{13} nanocluster, blue: background.

4. Discussion

We previously showed by immunohistochemistry on sections, that during the development of EAE pathogenesis, pathogenic $CD4^+$ T cells in the blood, which recognize myelin-derived antigens, accumulate at the dorsal vessels of the L5, followed by development of CNS inflammation, in a mechanism of IL-6 amplifier following gateway reflex triggered by gravity **(Arima et al., 2012)**.

In inflammatory diseases with stochastic and proliferative processes, including autoimmune diseases, single-cell events ultimately affect the health status of the entire organism. Therefore, it is desirable to establish a detection system that enables to quickly identify the development (Shichibu and Konishi, 2010; Sugiuchi et al., 2015) and progression of microinflammation, which contributes to inflammatory disease pathogenesis. However, the conventional protocols for identifying inflammatory sites are mainly based on 2D-histological analysis using inflammatory mediator-specific reporter mice or antibodies, and methods for rapid 3D-visualization of inflamed organs have not been established.

With an ultrasmall coordinated Au_{13} nanoclusters and CUBIC tissue-clearing method, we here established a new method of microinflammation detection in the L5. Mice induced aEAE or pEAE were intravenously injected a luminescent Au_{13} nanoclusters with high photostability, compatibility and sensitivity, as an inflammation probe (tracer) of microinflammation, and then subjected the lumbar cords to tissue-clearing method, in combination with the staining of artery and blood vessels using fluorescence-labeled anti-SMA and -CD31 antibodies, respectively. This protocol successfully detected a microinflammation site at the L5 in a 3D-image, that is consistent with the location of vascular gate toward the CNS for pathogenic immune cells, as shown in our previous report **(Arima et al., 2012)**.

Thus, our protocol will be not only useful for specifying and tracking a stepwise development of microinflammation triggered by a recruitment of pathogenic immune cells including $CD4^+$ T cells at specific blood vessels in multiple inflammatory disease models, but will also provide future perspectives of Au_{13} nanocluster-based imaging technique for a complete understandings of biological mechanism of disease pathogenesis and practical biomedical applications in fields of basic and clinical medicine, immunology, pathology.

Conclusion

- His-tagged SARS-CoV-2 recombinant proteins, including NSPs and SPs, were made success to synthesize, purify, and bound to Dynabeads in cell-free system.
- The PBMCs in healthy individuals contain more $CD4^+$ T cells reactive to SARS CoV-2 NSPs than SPs.
- Gold nanoclusters were detected microinflammation at the blood vessels around L5 spinal cords of active EAE and pathogenic $CD4^+$ T cell-transferred EAE models in 3D-image, where we previously reported in 2D-image by means of immunohistochemistry.

In conclusion, based on the results of this study of immunodominance and microinflammation detection methods. AIM^+CD4^+T cells strongly respond to NSPs than to SPs and successfully we detected the microinflammation at the blood vessels around L5 spinal cords of active EAE and pathogenic CD4 $^+$T cell-transferred EAE models using CUBIC tissue clearing method and 3D-image. Further studies required to use CUBIC tissue clearing method and 3D-image methods for detection of other inflammatory diseases in the future using different type of Gold-nano-clusters. Moreover, more experiments required to focus on NSPs evaluation using large number of healthy donors and comparing them with COVID-19 patients might help us for developing effective COVID-19 vaccine in the future.

Acknowledgements

At this moment while ending up my Ph.D., I want to express my deep gratitude for those whom with their support and guidance I reached this point. As an International student I want to thank the Ministry of Education, Culture, Sports, Science, and technology (MEXT) for the financial support. Thanks for Prof. Dr. Masaaki Murakami for his guidance, supervision. Thanks for Dr. Shintaro Hojyo for mentoring to me, Thanks for Dr. Rie Hasebe and Dr.Shimpei Kubota for supporting, me during the second part of my Ph.D, and for Dr. Daiskue Kamimura for supporting and advising me during the first part of my Ph.D. as well during applying to the MEXT scholarship. I also thank to Dr. Kazuki Tainaka for providing protocol and technical assistance of CUBIC tissue-clearing method, and to Dr. Katsuaki Konishi and Dr. Yukatsu Shichibu for providing Au_{13} nanoclusters. Thanks for Dr Kumiko Tanaka for sharing some of Purified SARS-CoV-2 proteins such as M protein. I would like to express my gratitude for being a PhD student at Hokkaido University. In addition to my sincere Thanks to Alexandria University for belonging to it in Egypt. Finally, I am very thankful to Abdelrhman for sharing my time in Japan.

Disclosure of Conflict of Interest

I declare that the research shown in the thesis was conducted in the absence of any commercial or financial relationships that could be construed as a potential conflict of interest.

References

Adelmann, M., Wood, J., Benzel, I., Fiori, P., Lassmann, H., Matthieu, J.M., Gardinier, M.V., Dornmair, K., and Linington, C.(1995). The N-terminal domain of the myelin oligodendrocyte glycoprotein (MOG) induces acute demyelinating experimental autoimmune encephalomyelitis in the Lewis rat. J.Neuroimmunol.*63*, 17-27.

Aharoni, R., Teitelbaum, D., Arnon, R., and Sela, M. (1999). Copolymer 1 acts against the immunodominant epitope 82-100 of myelin basic protein by T cell receptor antagonism in addition to major histocompatibility complex blocking. Proc.Natl.Acad.Sci U.S.A.*96*, 634-639.

Alexandersen, S., Chamings, A., and Bhatta, T.R.(2020).SARS-CoV-2 genomic and subgenomic RNAs in diagnostic samples are not an indicator of active replication.Nat. Commun.*11*, 6059.

Allegretta, M., Nicklas, J.A., Sriram, S., and Albertini, R.J.(1990).T cells responsive to myelin basic protein in patients with multiple sclerosis. Science *247*, 718-721.

Amor, S., Groome, N., Linington, C., Morris, M.M., Dornmair, K., Gardinier, M.V., Matthieu, J.M., and Baker, D. (1994). Identification of epitopes of myelin oligodendrocyte glycoprotein for the induction of experimental allergic encephalomyelitis in SJL and Biozzi AB/H mice. J Immunol. *153*, 4349-4356.

Amor, S., O'Neill, J.K., Morris, M.M., Smith, R.M., Wraith, D.C., Groome, N., Travers, P.J., and Baker, D. (1996). Encephalitogenic epitopes of myelin basic protein, proteolipid protein, myelin oligodendrocyte glycoprotein for experimental allergic encephalomyelitis induction in Biozzi ABH (H-2Ag7) mice share an amino acid motif. J.Immunol.*156*, 3000-3008.

Arima, Y., Harada, M., Kamimura, D., Park, J.H., Kawano, F., Yull, F.E., Kawamoto, T., Iwakura, Y., Betz, U.A., Marquez, G.*, et al.* (2012). Regional neural activation defines a gateway for autoreactive T cells to cross the blood-brain barrier. Cell. *148*, 447-457.

Arima, Y., Kamimura, D., Atsumi, T., Harada, M., Kawamoto, T., Nishikawa, N., Stofkova, A., Ohki, T., Higuchi, K., Morimoto, Y.*, et al.* (2015). A pain-mediated neural signal induces relapse in murine autoimmune encephalomyelitis, a multiple sclerosis model. Elife *4*.

Arima, Y., Ohki, T., Nishikawa, N., Higuchi, K., Ota, M., Tanaka, Y., Nio-Kobayashi, J., Elfeky, M., Sakai, R., Mori, Y.*, et al.* (2017). Brain micro-inflammation at specific vessels dysregulates organ-homeostasis via the activation of a new neural circuit. Elife *6*.

Arya, R., Kumari, S., Pandey, B., Mistry, H., Bihani, S.C., Das, A., Prashar, V., Gupta, G.D., Panicker, L., and Kumar, M. (2021).Structural insights into SARS-CoV-2 proteins. J.Mol.Biol. *433*, 166725.

Atsumi, T., Singh, R., Sabharwal, L., Bando, H., Meng, J., Arima, Y., Yamada, M., Harada, M., Jiang, J.J., Kamimura, D.*, et al.* (2014). Inflammation amplifier, a new paradigm in cancer biology.Cancer.Res. *74*, 8-14.

Atsumi, T., Suzuki, H., Jiang, J.J., Okuyama, Y., Nakagawa, I., Ota, M., Tanaka, Y., Ohki, T., Katsunuma, K., Nakajima, K.*, et al.* (2017). Rbm10 regulates inflammation development via alternative splicing of Dnmt3b. Int.Immunol.*29*, 581-591.

Bagley, S.J., Desai, A.S., Linette, G.P., June, C.H., and O'Rourke, D.M. (2018).CAR T-cell therapy for glioblastoma: recent clinical advances and future challenges. Neuro.Oncol *20*, 1429-1438.

Bartlam, M., Xu, Y., and Rao, Z. (2007). Structural proteomics of the SARS coronavirus: a model response to emerging infectious diseases. J.Struct.Funct.Genomics.*8*, 85-97.

Batoulis, H., Recks, M.S., Addicks, K., and Kuerten, S. (2011). Experimental autoimmune encephalomyelitis--achievements and prospective advances. APMIS.*119*, 819-830.
Bettelli, E., Das, M.P., Howard, E.D., Weiner, H.L., Sobel, R.A., and Kuchroo, V.K. (1998). IL-10 is critical in the regulation of autoimmune encephalomyelitis as demonstrated by studies of IL-10- and IL-4-deficient and transgenic mice. J.Immunol.*161*, 3299-3306.
Bettelli, E., Pagany, M., Weiner, H.L., Linington, C., Sobel, R.A., and Kuchroo, V.K. (2003). Myelin oligodendrocyte glycoprotein-specific T cell receptor transgenic mice develop spontaneous autoimmune optic neuritis. J.Exp.Med.*197*, 1073-1081.
Braczynski, A.K., Schulz, J.B., and Bach, J.P. (2017). Vaccination strategies in tauopathies and synucleinopathies. J.Neurochem. *143*, 467-488.
Braun, J., Loyal, L., Frentsch, M., Wendisch, D., Georg, P., Kurth, F., Hippenstiel, S., Dingeldey, M., Kruse, B., Fauchere, F.*, et al.* (2020). SARS-CoV-2-reactive T cells in healthy donors and patients with COVID-19. Nature.*587*, 270-274.
Chitnis, T., Najafian, N., Abdallah, K.A., Dong, V., Yagita, H., Sayegh, M.H., and Khoury, S.J. (2001). CD28-independent induction of experimental autoimmune encephalomyelitis. J. Clin.Invest *107*, 575-583.
Chou, Y.K., Bourdette, D.N., Offner, H., Whitham, R., Wang, R.Y., Hashim, G.A., and Vandenbark, A.A. (1992). Frequency of T cells specific for myelin basic protein and myelin proteolipid protein in blood and cerebrospinal fluid in multiple sclerosis. J.Neuroimmunol. *38*, 105-113.
Cua, D.J., Sherlock, J., Chen, Y., Murphy, C.A., Joyce, B., Seymour, B., Lucian, L., To, W., Kwan, S., Churakova, T.*, et al.* (2003). Interleukin-23 rather than interleukin-12 is the critical cytokine for autoimmune inflammation of the brain. Nature. *421*,744-748.
Dodt, H.U., Leischner, U., Schierloh, A., Jahrling, N., Mauch, C.P., Deininger, K., Deussing, J.M., Eder, M., Zieglgansberger, W., and Becker, K. (2007). Ultramicroscopy: three-dimensional visualization of neuronal networks in the whole mouse brain.Nat.Methods. *4*, 331-336.
Eguchi, S., Kawai, T., Scalia, R., and Rizzo, V. (2018). Understanding Angiotensin II Type 1 Receptor Signaling in Vascular Pathophysiology. Hypertension *71*, 804-810.
Ferber, I.A., Brocke, S., Taylor-Edwards, C., Ridgway, W., Dinisco, C., Steinman, L., Dalton, D., and Fathman, C.G. (1996). Mice with a disrupted IFN-gamma gene are susceptible to the induction of experimental autoimmune encephalomyelitis (EAE). J. Immunol.*156*, 5-7.
Frohman, E.M., Racke, M.K., and Raine, C.S. (2006). Multiple sclerosis--the plaque and its pathogenesis. N. Engl. J.Med. *354*, 942-955.
Fujita, M., Yamamoto, Y., Jiang, J.J., Atsumi, T., Tanaka, Y., Ohki, T., Murao, N., Funayama, E., Hayashi, T., Osawa, M.*, et al.* (2019). NEDD4 Is Involved in Inflammation Development during Keloid Formation. J.Invest. Dermatol.*139*, 333-341.
Fung, T.S., and Liu, D.X. (2019). Human Coronavirus: Host-Pathogen Interaction. Annu.Rev.Microbiol. *73*, 529-557.
Gorkhali, R., Koirala, P., Rijal, S., Mainali, A., Baral, A., and Bhattarai, H.K. (2021). Structure and Function of Major SARS-CoV-2 and SARS-CoV Proteins. Bioinform. Biol.Insights. *15*, 11779322211025876.
Gran, B., Zhang, G.X., Yu, S., Li, J., Chen, X.H., Ventura, E.S., Kamoun, M., and Rostami, A. (2002). IL-12p35-deficient mice are susceptible to experimental autoimmune encephalomyelitis: evidence for redundancy in the IL-12 system in the induction of central nervous system autoimmune demyelination. J.Immunol.*169*, 7104-7110.
Grifoni, A., Weiskopf, D., Ramirez, S.I., Mateus, J., Dan, J.M., Moderbacher, C.R., Rawlings, S.A., Sutherland, A., Premkumar, L., Jadi, R.S.*, et al.* (2020). Targets of T Cell Responses to SARS-

CoV-2 Coronavirus in Humans with COVID-19 Disease and Unexposed Individuals. Cell. *181*, 1489-1501e1415.
Hafler, D.A., Slavik, J.M., Anderson, D.E., O'Connor, K.C., De Jager, P., and Baecher-Allan, C. (2005). Multiple sclerosis. Immunol. Rev. *204*, 208-231.
Hama, H., Hioki, H., Namiki, K., Hoshida, T., Kurokawa, H., Ishidate, F., Kaneko, T., Akagi, T., Saito, T., Saido, T.*, et al.* (2015). ScaleS: an optical clearing palette for biological imaging. Nat.Neurosci. *18*, 1518-1529.
Harada, M., Kamimura, D., Arima, Y., Kohsaka, H., Nakatsuji, Y., Nishida, M., Atsumi, T., Meng, J., Bando, H., Singh, R.*, et al.* (2015). Temporal expression of growth factors triggered by epiregulin regulates inflammation development. J.Immunol.*194*, 1039-1046.
Hasebe, R., Murakami, K., Harada, M., Halaka, N., Nakagawa, H., Kawano, F., Ohira, Y., Kawamoto, T., Yull, F.E., Blackwell, T.S.*, et al.* (2022). ATP spreads inflammation to other limbs through crosstalk between sensory neurons and interneurons. J.Exp.Med *219*.
Hashizume, M., and Mihara, M. (2011). The roles of interleukin-6 in the pathogenesis of rheumatoid arthritis. Arthritis.*2011*, 765624.
Higuchi, H., Kamimura, D., Jiang, J.J., Atsumi, T., Iwami, D., Hotta, K., Harada, H., Takada, Y., Kanno-Okada, H., Hatanaka, K.C.*, et al.* (2020). Orosomucoid 1 is involved in the development of chronic allograft rejection after kidney transplantation. Int.Immunol.*32*, 335-346.
Hirano, T. (1992). Interleukin-6 and its relation to inflammation and disease. Clin.Immunol. Immunopathol.*62*, S60-65.
Hirano, T. (1998). Interleukin 6 and its receptor: ten years later.Int.Rev.Immunol.*16*, 249-284.
Hirano, T., Matsuda, T., Turner, M., Miyasaka, N., Buchan, G., Tang, B., Sato, K., Shimizu, M., Maini, R., Feldmann, M.*, et al.* (1988). Excessive production of interleukin 6/B cell stimulatory factor-2 in rheumatoid arthritis. Eur.J.Immunol.*18*,1797-1801.
Hirano, T., and Murakami, M. (2020).COVID-19: A New Virus, but a Familiar Receptor and Cytokine Release Syndrome.Immunity.*52*,731-733.
Hirano, T., Taga, T., Yasukawa, K., Nakajima, K., Nakano, N., Takatsuki, F., Shimizu, M., Murashima, A., Tsunasawa, S., Sakiyama, F.*, et al.* (1987). Human B-cell differentiation factor defined by an anti-peptide antibody and its possible role in autoantibody production. Proc.Natl.Acad. Sci.U.S.A. *84*, 228-231.
Hoffmann, M., Kleine-Weber, H., Schroeder, S., Kruger, N., Herrler, T., Erichsen, S., Schiergens, T.S., Herrler, G., Wu, N.H., Nitsche, A.*, et al.* (2020). SARS-CoV-2 Cell Entry Depends on ACE2 and TMPRSS2 and Is Blocked by a Clinically Proven Protease Inhibitor. Cell *181*, 271-280 e278.
Hojyo, S., Uchida, M., Tanaka, K., Hasebe, R., Tanaka, Y., Murakami, M., and Hirano, T. (2020). How COVID-19 induces cytokine storm with high mortality. Inflamm Regen *40*, 37.
Houssiau, F.A., Devogelaer, J.P., Van Damme, J., de Deuxchaisnes, C.N., and Van Snick, J. (1988). Interleukin-6 in synovial fluid and serum of patients with rheumatoid arthritis and other inflammatory arthritides. Arthritis.Rheum.*31*, 784-788.
Jin, R., Zeng, C., Zhou, M., and Chen, Y. (2016). Atomically Precise Colloidal Metal Nanoclusters and Nanoparticles: Fundamentals and Opportunities.Chem.Rev.*116*,10346-10413.
Jingwu, Z., Medaer, R., Hashim, G.A., Chin, Y., van den Berg-Loonen, E., and Raus, J.C. (1992). Myelin basic protein-specific T lymphocytes in multiple sclerosis and controls: precursor frequency, fine specificity, and cytotoxicity. Ann.Neuro. *32*, 330-338.
Jose, R.J., and Manuel, A. (2020). COVID-19 cytokine storm: the interplay between inflammation and coagulation. Lancet. Respir.Med.*8*, e46-e47.
Kamimura, D., Tanaka, Y., Hasebe, R., and Murakami, M. (2020). Bidirectional communication between neural and immune systems. Int. Immunol.*32*, 693-701.

Keegan, B.M., and Noseworthy, J.H. (2002). Multiple sclerosis. Annu.Rev.Med. *53*, 285-302.
Kerlero de Rosbo, N., Milo, R., Lees, M.B., Burger, D., Bernard, C.C., and Ben-Nun, A. (1993). Reactivity to myelin antigens in multiple sclerosis. Peripheral blood lymphocytes respond predominantly to myelin oligodendrocyte glycoprotein. J Clin Invest *92*, 2602-2608.
Kipp, M., van der Star, B., Vogel, D.Y., Puentes, F., van der Valk, P., Baker, D., and Amor, S. (2012). Experimental in vivo and in vitro models of multiple sclerosis: EAE and beyond. Mult Scler Relat Disord *1*, 15-28.
Kivisakk, P., Mahad, D.J., Callahan, M.K., Sikora, K., Trebst, C., Tucky, B., Wujek, J., Ravid, R., Staugaitis, S.M., Lassmann, H.*, et al.* (2004). Expression of CCR7 in multiple sclerosis: implications for CNS immunity. Ann.Neurol. *55*, 627-638.
Konishi, K., Iwasaki, M., and Shichibu, Y. (2018). Phosphine-Ligated Gold Clusters with Core+ exo Geometries: Unique Properties and Interactions at the Ligand-Cluster Interface. Acc.Chem. Res. *51*, 3125-3133.
Kuba, K., Imai, Y., Rao, S., Gao, H., Guo, F., Guan, B., Huan, Y., Yang, P., Zhang, Y., Deng, W.*, et al.* (2005).A crucial role of angiotensin converting enzyme 2 (ACE2) in SARS coronavirus-induced lung injury.Nat.Med.*11*, 875-879.
Kuchroo, V.K., Anderson, A.C., Waldner, H., Munder, M., Bettelli, E., and Nicholson, L.B. (2002). T cell response in experimental autoimmune encephalomyelitis (EAE): role of self and cross-reactive antigens in shaping, tuning, and regulating the autopathogenic T cell repertoire. Annu. Rev.Immunol.*20*, 101-123.
Kuchroo, V.K., Sobel, R.A., Laning, J.C., Martin, C.A., Greenfield, E., Dorf, M.E., and Lees, M.B. (1992). Experimental allergic encephalomyelitis mediated by cloned T cells specific for a synthetic peptide of myelin proteolipid protein. Fine specificity and T cell receptor V beta usage. J.Immunol. *148*, 3776-3782.
Langrish, C.L., McKenzie, B.S., Wilson, N.J., de Waal Malefyt, R., Kastelein, R.A., and Cua, D.J. (2004). IL-12 and IL-23: master regulators of innate and adaptive immunity. Immunol.Rev.*202*, 96-105.
Lassmann, H., Bruck, W., and Lucchinetti, C.F. (2007). The immunopathology of multiple sclerosis: an overview.Brain.Pathol. *17*, 210-218.
Lee, J., Nakagiri, T., Kamimura, D., Harada, M., Oto, T., Susaki, Y., Shintani, Y., Inoue, M., Miyoshi, S., Morii, E.*, et al.* (2013). IL-6 amplifier activation in epithelial regions of bronchi after allogeneic lung transplantation. Int.Immunol.*25*, 319-332.
Lee, J., Nakagiri, T., Oto, T., Harada, M., Morii, E., Shintani, Y., Inoue, M., Iwakura, Y., Miyoshi, S., Okumura, M.*, et al.* (2012). IL-6 amplifier, NF-kappaB-triggered positive feedback for IL-6 signaling, in grafts is involved in allogeneic rejection responses. J.Immunol. *189*, 1928-1936.
Li, W., Moore, M.J., Vasilieva, N., Sui, J., Wong, S.K., Berne, M.A., Somasundaran, M., Sullivan, J.L., Luzuriaga, K., Greenough, T.C.*, et al.* (2003). Angiotensin-converting enzyme 2 is a functional receptor for the SARS coronavirus. Nature. *426*, 450-454.
Loyal, L., Braun, J., Henze, L., Kruse, B., Dingeldey, M., Reimer, U., Kern, F., Schwarz, T., Mangold, M., Unger, C.*, et al.* (2021). Cross-reactive CD4(+) T cells enhance SARS-CoV-2 immune responses upon infection and vaccination. Science.*374*, eabh1823.
Lu, R., Zhao, X., Li, J., Niu, P., Yang, B., Wu, H., Wang, W., Song, H., Huang, B., Zhu, N.*, et al.* (2020). Genomic characterisation and epidemiology of 2019 novel coronavirus: implications for virus origins and receptor binding. Lancet. *395*, 565-574.
Lucchinetti, C., Bruck, W., Parisi, J., Scheithauer, B., Rodriguez, M., and Lassmann, H. (2000). Heterogeneity of multiple sclerosis lesions: implications for the pathogenesis of demyelination. Ann.Neurol. *47*, 707-717.

Luo, X., and Liu, J. (2022). Ultrasmall Luminescent Metal Nanoparticles: Surface Engineering Strategies for Biological Targeting and Imaging. Adv.Sci. (Weinh) *9*, e2103971.
Manfredonia, I., Nithin, C., Ponce-Salvatierra, A., Ghosh, P., Wirecki, T.K., Marinus, T., Ogando, N.S., Snijder, E.J., van Hemert, M.J., Bujnicki, J.M.*, et al.* (2020). Genome-wide mapping of SARS-CoV-2 RNA structures identifies therapeutically-relevant elements. Nucleic.Acids.Res. *48*, 12436-12452.
Markovic-Plese, S., Cortese, I., Wandinger, K.P., McFarland, H.F., and Martin, R. (2001). CD4+CD28- costimulation-independent T cells in multiple sclerosis. J.Clin.Invest.*108*, 1185-1194.
Mateus, J., Grifoni, A., Tarke, A., Sidney, J., Ramirez, S.I., Dan, J.M., Burger, Z.C., Rawlings, S.A., Smith, D.M., Phillips, E.*, et al.* (2020). Selective and cross-reactive SARS-CoV-2 T cell epitopes in unexposed humans. Science.*370*, 89-94.
Matsuyama, S., Nao, N., Shirato, K., Kawase, M., Saito, S., Takayama, I., Nagata, N., Sekizuka, T., Katoh, H., Kato, F.*, et al.* (2020). Enhanced isolation of SARS-CoV-2 by TMPRSS2-expressing cells. Proc Natl Acad Sci U S A *117*, 7001-7003.
McFarland, H.F., and Martin, R. (2007). Multiple sclerosis: a complicated picture of autoimmunity. Nat Immunol *8*, 913-919.
McGonagle, D., Sharif, K., O'Regan, A., and Bridgewood, C. (2020). The Role of Cytokines including Interleukin-6 in COVID-19 induced Pneumonia and Macrophage Activation Syndrome-Like Disease. Autoimmun. Rev.*19*, 102537.
Mehandru, S., and Merad, M. (2022). Pathological sequelae of long-haul COVID. Nat. Immunol. *23*, 194-202.
Mendel, I., Kerlero de Rosbo, N., and Ben-Nun, A. (1995). A myelin oligodendrocyte glycoprotein peptide induces typical chronic experimental autoimmune encephalomyelitis in H-2b mice: fine specificity and T cell receptor V beta expression of encephalitogenic T cells. Eur.J.Immunol.*25*, 1951-1959.
Meng, J., Jiang, J.J., Atsumi, T., Bando, H., Okuyama, Y., Sabharwal, L., Nakagawa, I., Higuchi, H., Ota, M., Okawara, M.*, et al.* (2016). Breakpoint Cluster Region-Mediated Inflammation Is Dependent on Casein Kinase II. J.Immunol. *197*, 3111-3119.
Murakami, M., Harada, M., Kamimura, D., Ogura, H., Okuyama, Y., Kumai, N., Okuyama, A., Singh, R., Jiang, J.J., Atsumi, T.*, et al.* (2013). Disease-association analysis of an inflammation-related feedback loop. Cell.Rep.*3*, 946-959.
Murakami, M., and Hirano, T. (2011). A four-step model for the IL-6 amplifier, a regulator of chronic inflammations in tissue-specific MHC class II-associated autoimmune diseases. Front.Immunol. *2*, 22.
Murakami, M., Kamimura, D., and Hirano, T. (2019). Pleiotropy and Specificity: Insights from the Interleukin 6 Family of Cytokines. Immunity.*50*, 812-831.
Murakami, M., Okuyama, Y., Ogura, H., Asano, S., Arima, Y., Tsuruoka, M., Harada, M., Kanamoto, M., Sawa, Y., Iwakura, Y.*, et al.* (2011). Local microbleeding facilitates IL-6- and IL-17-dependent arthritis in the absence of tissue antigen recognition by activated T cells. J Exp.Med.*208*, 103-114.
Noseworthy, J.H., Lucchinetti, C., Rodriguez, M., and Weinshenker, B.G. (2000). Multiple sclerosis.N.Engl. J.Med.*343*, 938-952.
Ogura, H., Murakami, M., Okuyama, Y., Tsuruoka, M., Kitabayashi, C., Kanamoto, M., Nishihara, M., Iwakura, Y., and Hirano, T. (2008). Interleukin-17 promotes autoimmunity by triggering a positive-feedback loop via interleukin-6 induction. Immunity *29*, 628-636.
Ohira, Y., Kawano, F., Stevens, J.L., Wang, X.D., and Ishihara, A. (2004). Load-dependent regulation of neuromuscular system. J.Gravit.Physiol.*11*, P127-128.

Oksenberg, J.R., Panzara, M.A., Begovich, A.B., Mitchell, D., Erlich, H.A., Murray, R.S., Shimonkevitz, R., Sherritt, M., Rothbard, J., Bernard, C.C.*, et al.* (1993). Selection for T-cell receptor V beta-D beta-J beta gene rearrangements with specificity for a myelin basic protein peptide in brain lesions of multiple sclerosis. Nature.*362*, 68-70.

Okuyama, Y., Tanaka, Y., Jiang, J.J., Kamimura, D., Nakamura, A., Ota, M., Ohki, T., Higo, D., Ogura, H., Ishii, N.*, et al.* (2018). Bmi1 Regulates IkappaBalpha Degradation via Association with the SCF Complex. J.Immunol.*201*, 2264-2272.

Ota, M., Tanaka, Y., Nakagawa, I., Jiang, J.J., Arima, Y., Kamimura, D., Onodera, T., Iwasaki, N., and Murakami, M. (2020).Role of Chondrocytes in the Development of Rheumatoid Arthritis Via Transmembrane Protein 147-Mediated NF-kappaB Activation. Arthritis. Rheumatol. *72*, 931-942.

Palmal, S., and Jana, N.R. (2014).Gold nanoclusters with enhanced tunable fluorescence as bioimaging probes.Wiley Interdiscip Rev.Nanomed.Nanobiotechnol.*6*,102-110.

Pelfrey, C.M., Trotter, J.L., Tranquill, L.R., and McFarland, H.F. (1994). Identification of a second T cell epitope of human proteolipid protein (residues 89-106) recognized by proliferative and cytolytic CD4+ T cells from multiple sclerosis patients. J Neuroimmunol *53*, 153-161.

Peng, Y., Felce, S.L., Dong, D., Penkava, F., Mentzer, A.J., Yao, X., Liu, G., Yin, Z., Chen, J.L., Lu, Y.*, et al.* (2022). An immunodominant NP105-113-B*07:02 cytotoxic T cell response controls viral replication and is associated with less severe COVID-19 disease. Nat.Immunol. *23*, 50-61.

Phan, L.T., Nguyen, T.V., Luong, Q.C., Nguyen, T.V., Nguyen, H.T., Le, H.Q., Nguyen, T.T., Cao, T.M., and Pham, Q.D. (2020). Importation and Human-to-Human Transmission of a Novel Coronavirus in Vietnam. N.Engl.J. Med. *382*, 872-874.

Pollinger, B., Krishnamoorthy, G., Berer, K., Lassmann, H., Bosl, M.R., Dunn, R., Domingues, H.S., Holz, A., Kurschus, F.C., and Wekerle, H. (2009). Spontaneous relapsing-remitting EAE in the SJL/J mouse: MOG-reactive transgenic T cells recruit endogenous MOG-specific B cells. J.Exp.Med.*206*, 1303-1316.

Prineas, J.W., and Wright, R.G. (1978). Macrophages, lymphocytes, and plasma cells in the perivascular compartment in chronic multiple sclerosis. Lab Invest *38*, 409-421.

Quan, W., Chen, J., Liu, Z., Tian, J., Chen, X., Wu, T., Ji, Z., Tang, J., Chu, H., Xu, H. and Zhao, Y. (2020). No SARS-CoV-2 in expressed prostatic secretion of patients with coronavirus disease 2019.a descriptive multicentre study in China. *MedRxiv*.

Raimondo, M.G., Biggioggero, M., Crotti, C., Becciolini, A., and Favalli, E.G. (2017). Profile of sarilumab and its potential in the treatment of rheumatoid arthritis. Drug.Des.Devel.Ther *11*, 1593-1603.

Raine, C.S. (1994). The Dale E. McFarlin Memorial Lecture: the immunology of the multiple sclerosis lesion. Ann.Neurol*36. Suppl*, S61-72.

Rydyznski Moderbacher, C., Ramirez, S.I., Dan, J.M., Grifoni, A., Hastie, K.M., Weiskopf, D., Belanger, S., Abbott, R.K., Kim, C., Choi, J.*, et al.* (2020). Antigen-Specific Adaptive Immunity to SARS-CoV-2 in Acute COVID-19 and Associations with Age and Disease Severity. Cell.*183*, 996-1012 e1019.

Scheller, J., Chalaris, A., Garbers, C., and Rose-John, S. (2011). ADAM17: a molecular switch to control inflammation and tissue regeneration. Trends Immunol *32*, 380-387.

Shen, J., Wang, H.Y., Chen, J.Y., and Liang, B.L. (2006). Morphologic analysis of normal human lumbar dorsal root ganglion by 3D MR imaging. AJNR. Am. J.Neuroradiol *27*, 2098-2103.

Shichibu, Y., and Konishi, K. (2010). HCl-induced nuclearity convergence in diphosphine-protected ultrasmall gold clusters: a novel synthetic route to "magic-number" Au13 clusters. Small *6*, 1216-1220.

Solanki, V., Tiwari, M., and Tiwari, V. (2021). Immunoinformatic approach to design a multiepitope vaccine targeting non-mutational hotspot regions of structural and non-structural proteins of the SARS CoV2. Peer.J. *9*, e11126.
Sospedra, M., and Martin, R. (2005). Immunology of multiple sclerosis. Annu.Rev.Immunol. *23*, 683-747.
Stefferl, A., Schubart, A., Storch, M., Amini, A., Mather, I., Lassmann, H., and Linington, C. (2000). Butyrophilin, a milk protein, modulates the encephalitogenic T cell response to myelin oligodendrocyte glycoprotein in experimental autoimmune encephalomyelitis. J Immunol *165*, 2859-2865.
Steinman, L. (2009). A molecular trio in relapse and remission in multiple sclerosis. Nat. Rev.Immunol. *9*, 440-447.
Stofkova, A., Kamimura, D., Ohki, T., Ota, M., Arima, Y., and Murakami, M. (2019). Photopic light-mediated down-regulation of local alpha1A-adrenergic signaling protects blood-retina barrier in experimental autoimmune uveoretinitis. Sci. Rep. *9*, 2353.
Stofkova, A., and Murakami, M. (2019). Neural activity regulates autoimmune diseases through the gateway reflex. Bioelectron. Med. *5*, 14.
Sugiuchi, M., Maeba, J., Okubo, N., Iwamura, M., Nozaki, K., and Konishi, K. (2017). Aggregation-Induced Fluorescence-to-Phosphorescence Switching of Molecular Gold Clusters. J.Am.Chem.Soc.*139*, 17731-17734.
Sugiuchi, M., Shichibu, Y., Nakanishi, T., Hasegawa, Y., and Konishi, K. (2015). Cluster-pi electronic interaction in a superatomic Au13 cluster bearing sigma-bonded acetylide ligands. Chem.Commun. (Camb).*51*, 13519-13522.
Susaki, E.A., Tainaka, K., Perrin, D., Kishino, F., Tawara, T., Watanabe, T.M., Yokoyama, C., Onoe, H., Eguchi, M., Yamaguchi, S.*, et al.* (2014). Whole-brain imaging with single-cell resolution using chemical cocktails and computational analysis. Cell.*157*, 726-739.
Tainaka, K., Kubota, S.I., Suyama, T.Q., Susaki, E.A., Perrin, D., Ukai-Tadenuma, M., Ukai, H., and Ueda, H.R. (2014). Whole-body imaging with single-cell resolution by tissue decolorization. Cell.*159*, 911-924.
Takada, Y., Kamimura, D., Jiang, J.J., Higuchi, H., Iwami, D., Hotta, K., Tanaka, Y., Ota, M., Higuchi, M., Nishio, S.*, et al.* (2020). Increased urinary exosomal SYT17 levels in chronic active antibody-mediated rejection after kidney transplantation via the IL-6 amplifier. Int. Immunol *32*, 653-662.
Tanaka, Y., Sabharwal, L., Ota, M., Nakagawa, I., Jiang, J.J., Arima, Y., Ogura, H., Okochi, M., Ishii, M., Kamimura, D.*, et al.* (2018). Presenilin 1 Regulates NF-kappaB Activation via Association with Breakpoint Cluster Region and Casein Kinase II.J.Immunol.*201*, 2256-2263.
Traugott, U., Reinherz, E.L., and Raine, C.S. (1983). Multiple sclerosis. Distribution of T cells, T cell subsets and Ia-positive macrophages in lesions of different ages. J.Neuroimmunol.*4*, 201-221.
Tuohy, V.K., Sobel, R.A., Lu, Z., Laursen, R.A., and Lees, M.B. (1992). Myelin proteolipid protein: minimum sequence requirements for active induction of autoimmune encephalomyelitis in SWR/J and SJL/J mice. J.Neuroimmunol.*39*, 67-74.
Uchida, M., Yamamoto, R., Matsuyama, S., Murakami, K., Hasebe, R., Hojyo, S., Tanaka, Y., and Murakami, M. (2022). Gateway reflexes, neuronal circuits that regulate the autoreactive T cells in organs having blood barriers. Int.Immunol.*34*, 59-65.
Ueda, H.R., Erturk, A., Chung, K., Gradinaru, V., Chedotal, A., Tomancak, P., and Keller, P.J. (2020). Tissue clearing and its applications in neuroscience. Nat.Rev.Neurosci.*21*, 61-79.

Van der Aa, A., Hellings, N., Bernard, C.C., Raus, J., and Stinissen, P. (2003).Functional properties of myelin oligodendrocyte glycoprotein-reactive T cells in multiple sclerosis patients and controls. J.Neuroimmunol.*137*, 164-176.
Verdecchia, P., Cavallini, C., Spanevello, A., and Angeli, F. (2020). The pivotal link between ACE2 deficiency and SARS-CoV-2 infection. Eur.J.Intern.Med.*76*, 14-20.
Weiskopf, D., Schmitz, K.S., Raadsen, M.P., Grifoni, A., Okba, N.M.A., Endeman, H., van den Akker, J.P.C., Molenkamp, R., Koopmans, M.P.G., van Gorp, E.C.M.*, et al.* (2020). Phenotype and kinetics of SARS-CoV-2-specific T cells in COVID-19 patients with acute respiratory distress syndrome. Sci.Immunol.*5*.
Wekerle, H., Kojima, K., Lannes-Vieira, J., Lassmann, H., and Linington, C. (1994). Animal models. Ann.Neurol*36. Suppl*, S47-53.
Wu, F., Zhao, S., Yu, B., Chen, Y.M., Wang, W., Song, Z.G., Hu, Y., Tao, Z.W., Tian, J.H., Pei, Y.Y.*, et al.* (2020). A new coronavirus associated with human respiratory disease in China. Nature. *579*, 265-269.
Wucherpfennig, K.W., Catz, I., Hausmann, S., Strominger, J.L., Steinman, L., and Warren, K.G. (1997). Recognition of the immunodominant myelin basic protein peptide by autoantibodies and HLA-DR2-restricted T cell clones from multiple sclerosis patients. Identity of key contact residues in the B-cell and T-cell epitopes. J.Clin.Invest.*100*, 1114-1122.
Wucherpfennig, K.W., Hafler, D.A., and Strominger, J.L. (1995). Structure of human T-cell receptors specific for an immunodominant myelin basic protein peptide: positioning of T-cell receptors on HLA-DR2/peptide complexes. Proc.Natl.Acad.Sci.U.S.A.*92*, 8896-8900.
Yednock, T.A., Cannon, C., Fritz, L.C., Sanchez-Madrid, F., Steinman, L., and Karin, N. (1992). Prevention of experimental autoimmune encephalomyelitis by antibodies against alpha 4 beta 1 integrin.Nature.*356*, 63-66.
Yoshizaki, K., Matsuda, T., Nishimoto, N., Kuritani, T., Taeho, L., Aozasa, K., Nakahata, T., Kawai, H., Tagoh, H., Komori, T.*, et al.* (1989). Pathogenic significance of interleukin-6 (IL-6/BSF-2) in Castleman's disease. Blood.*74*, 1360-1367.
Young, B.E., Fong, S.W., Chan, Y.H., Mak, T.M., Ang, L.W., Anderson, D.E., Lee, C.Y., Amrun, S.N., Lee, B., Goh, Y.S.*, et al.* (2020).Effects of a major deletion in the SARS-CoV-2 genome on the severity of infection and the inflammatory response: an observational cohort study.Lancet.*396*,603-611.
Zamvil, S.S., Mitchell, D.J., Moore, A.C., Kitamura, K., Steinman, L., and Rothbard, J.B. (1986). T-cell epitope of the autoantigen myelin basic protein that induces encephalomyelitis.Nature. *324*, 258-260.
Zhang, C., Gao, X., Chen, W., He, M., Yu, Y., Gao, G., and Sun, T. (2022). Advances of gold nanoclusters for bioimaging. i.Science.*25*, 105022.
Zhang, G.X., Gran, B., Yu, S., Li, J., Siglienti, I., Chen, X., Kamoun, M., and Rostami, A. (2003). Induction of experimental autoimmune encephalomyelitis in IL-12 receptor-beta 2-deficient mice: IL-12 responsiveness is not required in the pathogenesis of inflammatory demyelination in the central nervous system. J.Immunol.*170*, 2153-2160.
Zhang, J., Markovic-Plese, S., Lacet, B., Raus, J., Weiner, H.L., and Hafler, D.A. (1994). Increased frequency of interleukin 2-responsive T cells specific for myelin basic protein and proteolipid protein in peripheral blood and cerebrospinal fluid of patients with multiple sclerosis. J.Exp.Med.*179*, 973-984.
Zhou, F., Yu, T., Du, R., Fan, G., Liu, Y., Liu, Z., Xiang, J., Wang, Y., Song, B., Gu, X.*, et al.* (2020a). Clinical course and risk factors for mortality of adult inpatients with COVID-19 in Wuhan, China: a retrospective cohort study. Lancet.*395*, 1054-1062.

Zhou, P., Yang, X.L., Wang, X.G., Hu, B., Zhang, L., Zhang, W., Si, H.R., Zhu, Y., Li, B., Huang, C.L., *et al.* (2020b). A pneumonia outbreak associated with a new coronavirus of probable bat origin. Nature. *579*, 270-273.
Ziebuhr, J. (2004). Molecular biology of severe acute respiratory syndrome coronavirus. Curr.Opin.Microbiol *7*, 412-419.